Spectroscopy of size dependent many-particle effects in single self-assembled semiconductor quantum dots

Von der Fakultät für Physik und Geowissenschaften
der Technischen Universität Carolo-Wilhelmina
zu Braunschweig
zur Erlangung des Grades eines
Doktors der Naturwissenschaften
(Dr. rer. nat.)
genehmigte
D i s s e r t a t i o n

von Claudio Dal Savio

aus Bolzano (Italien)

1. Referent: Prof. Dr. Andreas Hangleiter
2. Referent: Prof. Dr. Ernst Otto Göbel

Eingereicht am: 06.12.2005
Mündliche Prüfung am: 20.02.2006
2006

Vorveröffentlichungen der Dissertation

Teilergebnisse aus dieser Arbeit wurden mit Genehmigung der Fakultät für Physik und Geowissenschaften, vertreten durch den Mentor, in folgenden Beiträgen vorab veröffentlicht:

Publikationen

Dal Savio C., Kazantsev D.V., Güttler B. & Danzebrink H.-U. Micro-photoluminescence set-up for low-temperature single quantum dot spectroscopy in the near infrared. Submitted to J. Appl. Phys.

Alla mia famiglia

Acknowledgements

I would like to thank my supervisor Prof. Dr. A. Hangleiter for the stimulating discussions and always fruitful help during this work and Prof. Dr. E. O. Göbel for his important advices after reading the manuscript.

I'm grateful to Dr. H.-U. Danzebrink for the possibility to carry out this work in the Physikalisch-Technische Bundesanstalt (PTB) and for all the things I have learned working in his group.

I would like to thank Dr. B. Güttler for the valuable discussions and his support in this long time and H. Niemann for the help with the low temperature equipment.

I'm thankful to Dr. K. Pierz, for preparing the quantum dot samples, for being always willing to answer my questions and for all the discussions together with Dr. F. Ahlers. Furthermore I would like to thank Dr. U. Siegner for carefully reading parts of this manuscript and Dr. G. Ade for the TEM images of the quantum dot sample.

I would like to thank all the current and former members of the PTB Divisions „Quantitative Scanning Probe Microscopy" and „Layer Thickness and Nanostructures" that I have interacted with and in particular Dr. D. Kasantzev for his work in setting up the low temperature system. I would like to single out D. Schulz, M. Kempe and H. Wolff for their help and friendship.

This work is dedicated to my family.

Abstract

Single InAs quantum dots (QDs) grown with the Stranski-Krastanov method in a $In_{0,12}Ga_{0,88}As$ quantum well embedded in GaAs and emitting in the near infrared have been optically investigated. To perform QD spectroscopy at low temperatures a very stable micro-photoluminescence (μ-PL) microscope set-up fully integrated in a liquid helium (LHe) cryostate has been successfully developed. The system is based on the cold finger technique and a Fourier Transform (FT) spectrometer combined with a nitrogen cooled Ge detector.
Photoluminescence of the QDs was excited non resonantly with a He-Ne laser and single dot spectroscopy was carried out at temperatures below 60 K. The experimental set-up allows mapping of the optical emission by recording spectra for every point of a scan grid. This mapping mode is used to acquire optical images and to locate a particular dot for investigation. Series of measurement on a single QD were normally performed over a long time (from a few days to a week), with the need of daily adjustment in the sub-micrometer range.
At low excitation power a single sharp line (E_x) arising from recombination of a single exciton in the dot is observed. Varying the excitation density the spectra become more complex, with appearance of the biexciton emission line (E_{xx}) on the lower energies side of the E_x line, followed by emission from excitons occupying higher shells in the dot. Measured biexciton binding energies and power dependence are in good agreement with values reported in the literature. The temperature dependence of the optical emission was investigated. The energy shows the characteristic decrease related to the shrinking of the semiconductor band gap, while the linewidth evolution is compatible with broadening due to coupling with acoustic and optical phonons.
A statistics of biexciton binding energies over a dozen of dots was acquired and the results compared with single QD spectroscopy data available in the literature, for III-V material systems. Despite the impossibility to obtain precise information about the dimensions of the particular QD under investigation, from the analysis of these data a general trend can be found in the dependency of the biexciton binding energy on the size of InAs QDs, parameterised with their emission energy.

Contents

1. Introduction

1.1 Semiconductor technology and quantum dots

The development of semiconductor technology towards high performance devices based on smaller components is driven by the need of transport, processing and storage of the continuously growing volume of information that characterises our age. Key components of this technology are microelectronic and optical devices, which make this information transfer and processing possible. The continuous miniaturising process has led to the typical structures size in the present microprocessors of about 90 nm and to integrated circuits containing tens of millions of transistors. But, as the size of the transistor decreases, quantum effects become significant, so that the physical limit for classical electronic structures will be reached soon.

New concepts and device architectures will be therefore needed to improve the speed and the efficiency of transmission systems and to overcome the limit of conventional electronic components and microprocessors. A possible solution is the use of nanostructures like semiconductor QDs [1], nanometer sized objects which provide a full three-dimensional confinement for conduction band electrons and valence band holes. A QD can be realized by embedding a semiconductor crystal of small energy gap and with a size comparable with the de Broglie wavelength of the carriers, in a semiconductor material with larger energy gap. Because of the complete confinement only specific energy levels are allowed, thus, in analogy with atoms, the density of states becomes discrete.

Quantum dots may play an important role in the development of novel opto-electronic devices. QD lasers and semiconductor optical amplifier [2], efficient light-emitting-diodes (LEDs) [3] and high performance mid-infrared photodetectors [4] based on QDs have been already demonstrated. These applications take advantage of the cumulative effect of a large number of QDs, but of great interest is the development of devices based on the properties of a single QD or of only a few interacting dots. QD based single photon emitters [5][6] and entangled photons source [7] have been already demonstrated and may play an important

technological role in the development of quantum cryptography systems [8]. An advantage of the QD system in comparison to other types of single photon sources like atomic cascades is the quantum efficiency for photon pair production. In atomic cascades the excitation process has a very low efficiency because it is proportional to the absorption cross section of the atom itself, while QDs allow for non resonant laser excitation. Photons are absorbed in the surrounding material and the so created electron-hole pairs are efficiently captured into the dot. Furthermore, compared to atoms, QDs have the advantage of mechanical stability and long lifetime.
Another very promising concept is the use of QDs to implement computing logic. Quantum computing [8] uses quantum mechanics phenomena such as superposition and entanglement to perform operation on data represented by the units of quantum information, the qubits. A pure qubit state is a linear superposition of the two states in a two level system. In principle, any two level quantum system can be used as a qubit. But for quantum computation, only systems are interesting which show long decoherence times. Therefore, one important demand on such a system is a weak coupling to their environment. At present there are various proposals for the realization of quantum logic architectures, implemented using semiconductor nanostructures. Many of these require the use of excitons, biexcitons and spin excitations within individual QDs [9][10][11]. Semiconductors QDs are of special interest, since in contrast to other possible candidate systems (trapped ions, nuclear magnetic resonance superconducting systems), they potentially provide an interface between existing digital electronic and quantum based computing elements, so that they could be implemented with currently well developed technologies.
A complete understanding of the mechanisms governing the physical properties of an ensemble and a single QD is of great importance from the point of view of basic research and it is required for the development and the design of more efficient devices. The long time goal is the development and realization of quantum computing and quantum information processing devices operating on the basis of single electrons, excitons, or photons.

1.2 Quantum dots research

Semiconductor quantum dots can be fabricated or grown using different techniques, such lateral patterning of a QW structure performed with e-beam lithography and reactive ion or wet etching [12], intermixing by focused laser beams [13] or focused ion beams [14], chemical synthesis (nanocrystals) [15], natural formation at the interfaces of a QW [16] and Stranski-Krastanov self-assembled epitaxial growth [17]. Among all the different fabrication techniques, self-assembly leads to the formation of QDs of very high optical quality and it has become a standard fabrication method. Since the begin of the 80's QDs have been subject of a great research effort, started with the characterisation of the electrical and optical properties of dots ensembles. Emission techniques [18] such as photoluminescence (PL), electroluminescence (EL), cathodoluminescence (CL) and absorption

techniques [18] such as PL-excitation spectroscopy (PLE) have been used to perform a wide range of experiments in the spectral and time domain under different conditions (temperature, excitation energy and intensity, in electric and magnetic fields, different charging states).
Inhomogeneous broadening is dominant if the spectra are averaged over an ensemble of dots with fluctuation in size, shape and composition, so that it is impossible to observe in the spectra signatures of the individual QDs, like Coulomb many-particle effects involving energy shifts at the meV level [19], lifetime limited linewidths [20], quantum interference effects [21][22].
Around 1994 the first optical spectroscopy studies on single QDs have been reported in the literature [23] (and references therein). Spectroscopy on a single quantum dot is a challenging task, which requires cryogenic temperature and high signal collection efficiency. The spatial resolution has to be comparable with the relevant length scale of the system, i.e. the interdot separation. Technical considerations have to include, therefore, the optical system as well as the structure of the QD sample under investigation.
Single isolated QDs can be fabricated with lithography techniques and, in the case of self-assembled QDs, samples with very low dot's density can be obtained under particular growth conditions, for example by asymmetrical deposition of the dot layer. In this way interdot distances in the range of a few microns can be achieved. Covering the sample with aperture patterned metal layers or etching small mesas are techniques used to isolate a few or only one dot in a small area which can be easily investigated even with low resolution systems. Furthermore a patterned surface allows to easily localize the investigated QD again for further investigations. The drawback of these methods are the modifications of the sample, which can spoil the quality of the QDs or influence their emission [20].
Far-field methods like confocal microscopy provide, by use of conventional microscope objectives with high numerical aperture, an efficient excitation and collection of the dot's photoluminescence with a spatial resolution in the 1 μm range. Special techniques like solid immersion lens (SIL) [24] can extend this range to 0,25 μm [25]. A higher optical resolution can be reached with a scanning near field optical microscope (SNOM) [26], which allows lateral resolutions down to ~30 nm [27] (i.e. in the dots size range), however at the cost of optical throughput.
With the help of these techniques, spectroscopy on single QDs has become a powerful research tool for the investigation of quantum phenomena in zero dimensional systems [28]. The typical fingerprint of the emission from a single QD is the presence in the spectrum of an isolated narrow line and the appearance of groups of lines with increasing excitation power, due to the filling of the discrete energy levels in the dot. The ground state emission is due to recombination of a single exciton (a bound electron-hole pair), which is followed, increasing the number of excitons in the dot, by the biexciton decay and the emission from the excited states. Pauli blocking allows for only two excitons in the lower energy state, forming the biexciton complex. Additional excitons have to occupy higher energetic levels. Beside power dependence studies [19][29][30], the time evolution [21], the effect of the temperature [20][31], the influence of magnetic [32][33] and

electric fields [34] and charged exciton complexes [35] have been widely investigated.
An open problem in single QD spectroscopy studies is the direct comparison between experimental results and theoretical description. The energetic levels in a QD depend on its geometrical and chemical properties, which, in general, are parameters known only with great uncertainty. A systematic study of the quantum confinement effects as a function of the QD size is possible only in the case of lithographically defined structures [36][37][38][39]. On the other hand the disadvantage of this fabrication technique is the incorporation of impurities and structural imperfections during the process of lateral patterning, leading to a low crystal quality at the sidewalls and to an enhancement of non-radiative recombination processes. Furthermore the lateral size is limited to about 20 nm.
In the high quality *self-assembled* QD's samples the dots are embedded in a matrix with a larger band gap material in comparison to the dot one. The dots geometry can be well characterised before the capping process using scanning force (SFM) and scanning tunnelling microscopy (STM) [40], but it will be strongly influenced by the deposition of the cap layer. Partial knowledge about the dot's geometry can be obtained with STM and transmission electron microscopy (TEM) studies on thin sections of the capped samples. With these techniques it is possible to determine the height of the QDs with very high precision, but lateral sizes and shape can only be deduced in an approximate way [41]. These studies can even provide information about the composition and strain distribution in a QD [42].
It has to be noticed that this partial knowledge does not refer to a particular optically investigated QD, thus a straightforward comparison of the spectroscopical data with theoretical calculations is not yet possible for epitaxially grown *self-assembled* QDs. A way to gain some insights into the interplay of geometry and material composition on one side and the optical properties on the other side, is to perform statistical studies of single QDs on the same sample: dependence on size of the emission of excited states [43], biexciton [44] and charged exciton complexes binding energies [45] and linewidths [46] have been already subject of investigations. In these studies the size of the dots is parameterised by their ground state emission energy, because, reducing the size of the QDs, the ground state emission energy shifts to higher energies. The dependence between size and emission energy has been proved with studies on dots ensembles. The observation of a multimodal distribution of the exciton ground state emission energy in an ensemble of InAs/GaAs QDs has been explained by shell-like monolayer (ML) variation of the QDs size [47] from one subensemble to the next. Comparison of the optical data to theoretical calculations yields excellent agreement, assuming a shell-like evolution of the dot volume, characterised by a 2 ML growth of the base length for each 1 ML variation of the QD height [48].

Of special interest is the occupation of the QD with two electron-holes pairs, which form the biexciton complex. The exciton-biexciton system plays an important role in QD based single photon emitters [5][6][49] and as source of entangled photons [50], with possible applications in quantum cryptography and quantum computing systems [51]. The existence of biexcitons in a semiconductor has been predicted by

Lampert [52] and, in a two dimensional system, they first have been observed in 1982 by Miller *et al.* [53]. In a structure of higher dimensionality the biexciton complex is the bound state of two excitons and the binding energy is defined as the energy gain with respect of two spatially separated excitons. In a QD this definition is no more appropriate, because the confinement potential does not allow the unbound state, but it is still useful to retain it. The biexciton binding energy is the result of different aspects of the Coulomb interaction, namely direct attraction or repulsion between carriers, correlation and exchange. The strength of the various contributions depends on the structural and chemical properties of the QD and of the surrounding matrix. The dependence of the biexciton binding energy on the size of *self-assembled* QDs is a debated argument, which has been subject of both theoretical [54][55][56][57] and experimental investigation [44][45][58].
This thesis presents an optical spectroscopy study of self-assembled InAs QDs embedded in a InGaAs quantum well (QW). With experiments on single QDs a statistics of their optical emission characteristics and in particular of their biexciton binding energies over a dozen of dots has been obtained. These data have been compared with published experimental results about single dot experiments on different QD's systems, to provide some insights into the dependence of the biexciton binding energy on the dot size.

1.3 Present work

This work is organised as follows. In the second chapter theoretical foundations will be presented, with an introduction to the factors which determine the single particle energy levels in the dot and to the complicated picture arising from many-particle occupation. The concept of a biexciton binding energy in the QDs and its physical meaning are discussed. This theoretical part is concluded with a discussion of the dependence of the optical linewidth and the emission energy on the temperature.
In the third chapter the Stranski-Krastanov growth process of the investigated QDs is described. The sample presents a gradient in the dot density, which allows for single dot spectroscopy in the region where the mean inter-dot distance lies in the range of a few micrometers. Transmission electron microscope (TEM) images and a first optical characterisation performed at 7 K with a macro-photoluminescence set-up are presented. The QDs emit in the near infrared (NIR) region of the spectrum.
To perform measurements on a single dot a very stable low temperature scanning optical microscope has been developed. Chapter four is devoted to the description of the experimental set-up. Cooling of the sample down to 5 K is achieved with the cold finger technique. Normal optical objectives have been used for the micro-photoluminescence (μ-PL) experiments and the spectra have been acquired with a Fourier Transform spectrometer, in combination with a high sensitivity nitrogen cooled germanium detector.

The different experiments performed to characterise the InAs quantum dots sample will be discussed in the fifth chapter, starting with μ-PL measurement on an ensemble of dots on the high dot density part of the sample, showing inhomogeneous broadened emission and a complicate structure. Moving towards the low dot density part of the sample allows to perform measurements on single QDs. The mapping option of the system is described, which allows for the acquisition of one spectrum for each point of a scanning grid. From the resulting 3D set of data (x, y, I(E)) optical images of the dot emission at a given energy or in an energy interval can be extracted.
A single resolution-limited sharp line due to recombination of a single exciton characterises, as expected, the emission of a single dot at very low excitation power. The evolution of the spectra at different excitation powers has been observed, with the appearance of the biexciton line followed by lines arising from recombination of excited states in higher energetic shells. The multi-excitonic emission is accompanied at the same time by the saturation of the exciton and biexciton emissions. Furthermore the temperature dependence of the single dot emission has been measured.
In chapter six the biexciton binding energy data acquired in this work have been compared with the experimental results available in the literature for III-V QD systems. The analysis of these data leads to a characteristic trend for the biexciton binding energy dependence on the size for InAs QDs. The dot size is parameterised with the emission energy and the correlation between real size and emission energy is demonstrated in the case of InAs on GaAs QDs, for which dimensions extracted from TEM measurements are presented in several works. Furthermore the dependence of the biexciton binding energy on the section area and on the aspect ratio is plotted.

2. Quantum dots

2.1 What is a quantum dot?

If the size of a semiconductor crystal is reduced to the nanometer scale in one direction and the crystal is surrounded by other crystals acting as potential barriers, the freedom of carrier movement is lost in that direction. Carriers in a bulk semiconductor are free to move in every direction, thus, with respect to their movement degrees of freedom, the bulk is a three dimensional (3D) structure; in a quantum well (QW) they can only move in a plane (2D), while shrinking another dimension leads to a quantum wire (QWR) structure, where only translation in one direction is allowed (1D); carriers in a quantum dot are completely localized (0D). Depending on the dimensionality of the structure the density of states (DOS) for the carriers changes from a continue distribution to a discrete one in a QD (fig. 2.1). An ideal QD is an object where the full three dimensional confinement of elementary charges or excitations (excitons) is achieved. Its size has to be of the order of the carrier's de Broglie wavelength.

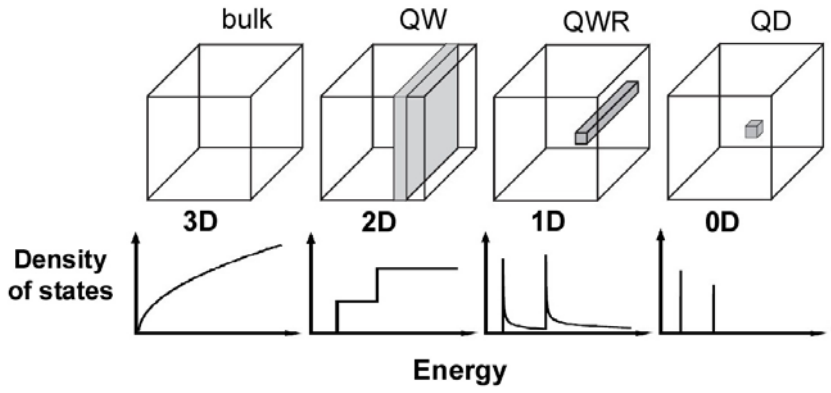

Figure 2.1 Electron density of states (DOS) in semiconductor structures of decreasing dimensionality: bulk (3D), quantum well (2D), quantum wire (1D), quantum dot (0D).

Typical QDs lateral dimensions are in the 2 – 100 nm range, corresponding to about 10^3 to 10^6 lattice atoms. While it is possible to make QDs with different types of materials, using semiconductor crystals has the important obvious advantage of a possible easier integration in existing semiconductor electronic components, taking advantage of sophisticated technology that has already been developed. Full 3D confinement can be obtained in a variety of semiconductor quantum dots structures grown or fabricated using different techniques, but self-assembly leads to the formation of QDs of very high optical quality. The formation of QDs using epitaxy is called the Stranski-Krastanov [17] growth method and is based on the thermodynamic instability during the deposition of an epitaxial film on a lattice mismatched substrate (fig. 2.2). In the very first stage of the growth, below a critical thickness, a pseudomorphic layer with the lateral lattice constant of the substrate is formed. During growth the elastic energy stored in this layer increases. With increasing thickness the accumulated compressive strain can no longer be accommodated in a two-dimensional arrangement and the total film energy relaxes through the formation of coherently strained islands on top of the remaining part of the two-dimensional layer, the wetting layer. The islands are finally embedded into a larger band gap material. Self-assembled QDs (SAQDs) can be realized by molecular beam epitaxy (MBE) or metal organic chemical vapour deposition (MOCVD) on a variety of different semiconductor material systems, comprising III-V compounds systems and also II-VI and IV-VI materials.

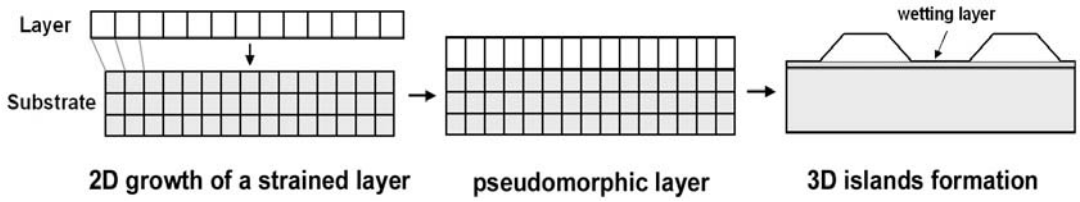

Figure 2.2 The Stranski-Krastanov growth method: the deposition of a lattice mismatched layer on a substrate leads to the formation of a pseudomorfic layer followed by the islands growth.

Self-assembled QDs are coherently strained and their growth is essentially defect and impurity free. They can be easily embedded during growth into more complex structures, like electrodes or optical cavities, making them attractive for different kinds of electronic and photonic devices. Depending on their size and composition the emission wavelengths span in a wide range between 0,3 μm and 1,5 μm. The exact shape, dimension and composition of the self-assembled QDs are generally not known accurately. Surface exchange reactions and diffusion processes play an important rule in the growth process and depending on the materials and the growth conditions, the shape can be pyramidal, multifaceted, or nearly lens-shaped with lateral (vertical) dimensions ranging from ~10 (~2) nm to about ~50 (~15) nm, adjustable within certain limits by choosing appropriate growth conditions. The quantum dot size distribution is poorly controlled, their size dispersion is in general about 10% and is a function of the substrate deposition temperature and the surface

growth kinetics. Although the island geometry can be well characterised using AFM and STM, it will dramatically change during the capping process by the larger band gap film.

2.2 Artificial atoms and the quantum dot problem

Semiconductor QDs are often described as "artificial atoms" [59] due to their delta-like density of states (DOS) (fig. 2.1), which, in analogy with atoms, should result in discrete and very narrow lines in the optical emission spectra. However there are great differences between the two systems, first of all linewidths of atomic emission lines are orders-of-magnitudes smaller compared to those of QDs [60]. Furthermore semiconductor QDs typically consist of thousands of atoms arranged in a finite size lattice, which again is contained in a host crystal with different composition. In contrast to free atoms, QDs are therefore subjected to the interactions with the lattice vibrations (phonons), which leave directly fingerprints in the emission and absorption spectra and, being responsible of the temperature dependence of the band gaps of the respective semiconductors, cause the thermal drift of the transition energies. The analogy with atoms should also be taken carefully, nevertheless it is still useful to adopt the shell notation (n = 1, 2, 3 = s, p, d) used in atomic spectroscopy for the structure of the energetic levels in the QDs (fig. 2.3).
The theoretical description of the optical properties requires the calculation of the single particle energy levels in the dot. The simplest model of a QD is the problem of a particle in a infinite barrier box. First steps towards a more realistic approach are performed taking in consideration the finite height of the confinement potential and the morphological characteristics of the dot, like shape and composition. Furthermore the influence of strain, strain induced effects like piezoelectricity and many-particle interactions (direct Coulomb, exchange and correlation) between carriers need to be considered.

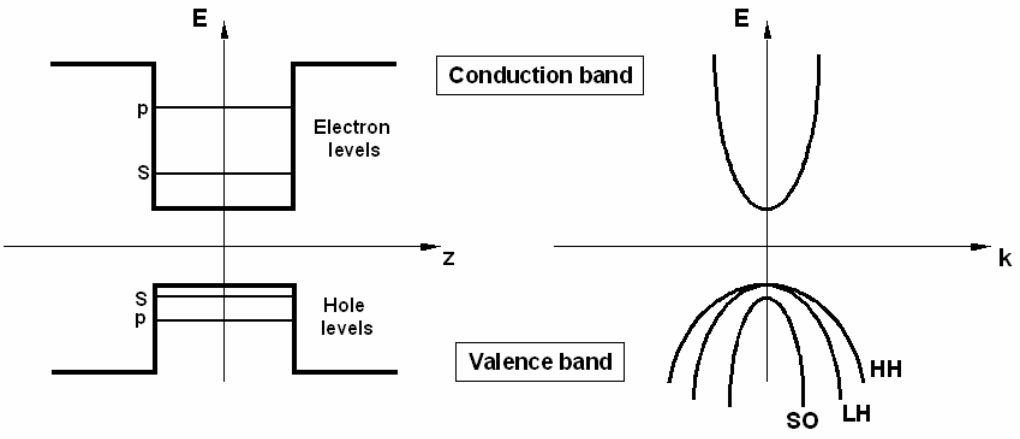

Figure 2.3 Schematic energy diagram for the quantum dot and barrier, and band structure showing the conduction band, heavy hole (HH), light hole (LH) and split-off (SO) bands.

Different methods have been applied to obtain an approximate solution of this problem. Single particle states can be obtained from numerical **k·p** calculations, performed typically in an 8-band version, with the inclusion of two conduction bands (spin up and down), two heavy hole (HH), two light hole (LH) and two spin-split off bands (SO) [61] (fig. 2.3). Beside the shape and composition of the QD, the parameters which enter the model are the band structure and the bulk elastic properties. Starting point of this method is the determination of the QD confining potential details, performed using elastic continuum models or atomistic models and taking into account piezoelectric effects. The single particle eigenstates in the conduction- and valence-band are subsequently obtained with numerical **k·p** calculations in the effective mass approximation. Starting from the analysis of the atomistic structure of the dot other solution methods have been developed, like the tight-binding approach [62] and the empirical pseudo-potential method (EPM) [63]. The single particle wave functions obtained with one of these methods are used to form a system of antisymmetric few-particle wave functions to express the solution of the respective few-particle Hamiltonian (configuration-interaction method). On the basis of the calculated eigenstates the optical properties of the QD (interband and intraband transition energies, oscillator strengths as well as polarizations for the various transitions), and also exciton ground state binding energies can be obtained.
A very important point has to be addressed. The direct comparison of theoretical calculations with the results of experiments on a single self-assembled QD is yet impossible, because the exact geometrical and chemical structure of the investigated dot is unknown. Insights into the interplay of geometry and material composition on one side and the optical properties on the other side can only be obtained comparing experimental data for different QDs.

2.3 Single particle states

The confinement of elementary charges or excitations (excitons) in a QD leads to discrete density of states and energy levels. In the bulk the exciton is a two particle complex formed by one hole and one electron, bound together by their mutual Coulomb interaction. The total Hamiltonian for an electron-hole pair in a quantum structure in absence of external electric or magnetic fields can be written as:

$$\mathcal{H} = \mathcal{H}_e + \mathcal{H}_h + \mathcal{H}_{Coulomb} + \mathcal{H}_{exchange} \tag{2.1}$$

with the first two terms representing the energies of electron and holes, the third their mutual Coulomb interaction and the last one the contribution of exchange and correlation effects.
The effective-mass approximation is used to describe the electronic states of bulk semiconductors and it is applicable to quantum dot systems which are macroscopic in comparison to the unit cell of the material. In the framework of this approximation and neglecting the *Coulomb* and *exchange* terms in the Hamiltonian

(2.1), both of the carrier's wave functions have to be solution of the Schrödinger equation with respect to the confinement potential

$$\mathcal{H}_\nu \varphi(\mathbf{r}_\nu) = \left\{ -\frac{\hbar^2}{2m_\nu^*}\nabla^2 + V_\nu(\mathbf{r}) \right\} \varphi(\mathbf{r}_\nu) = E_\nu \varphi(\mathbf{r}_\nu) \tag{2.2}$$

where $\nu = e,h$ distinguish between electron and hole, m_ν^* is the effective mass for the respective carrier and $V_\nu(\mathbf{r})$ is the confinement potential. With this raw simplification the problem reduces to the well known single particle problem. Carriers confined in the QD can take only discrete energies $E_{\nu,n} < V_{\max}$, whose values and numbers are strongly dependent on the details of the confinement potential. For a parallelepipedic QD with infinite barrier the energy eigenvalues are:

$$E_{n_x,n_y,n_z} = \frac{\hbar^2\pi^2}{2}\left(\frac{n_x^2}{m_x^* L_x^2} + \frac{n_y^2}{m_y^* L_y^2} + \frac{n_z^2}{m_z^* L_z^2} \right) \tag{2.3}$$

where (n_x, n_y, n_z) are the quantum numbers. They are integers but not all of them are allowed to be 0. $L_{x,y,z}$ are the dimensions of the QD and $m_{x,y,z}^*$ the effective masses in the respective directions. This simple model shows the characteristic quantisation of the energy levels due to the confinement and the dependency of the energy levels on the effective masses of the carriers and on the QD size.

2.3.1 Strong and weak confinement approximations

The direct Coulomb interaction between electron and hole is described by the term

$$\mathcal{H}_{Coulomb} = -\frac{e^2}{\varepsilon |\mathbf{r}_e - \mathbf{r}_h|} \tag{2.4}$$

In bulk materials the influence of the Coulomb potential is the reason for the existence of the excitons. An exact solution of the Hamiltonian (2.1) including the first three terms is not possible. However two regimes can be found in the confinement, which lead to a simplification, namely the QD of dimension smaller or bigger in comparison to the exciton Bohr radius a_B^{exc}.

In the first case, for $r << a_B^{exc}$ the eigenenergies of the confinement Hamiltonians for electron and holes are larger than the exciton binding energy given by the Coulomb interaction, situation called "strong confinement" approximation. In this regime the main contribution of $\mathcal{H}$ arises from the confinement contributions $\mathcal{H}_e$ and $\mathcal{H}_h$ for electrons and holes and it is possible to neglect the Coulomb interaction

between the carriers. The problem simplifies to the above discussed single particle one, and the other terms in the Hamiltonian (2.1) can be treated as perturbations. Dimensions of self-assembled QDs lie in the range 2-10 nm in the growth (z) direction and 10-50 nm in the x–y plane. For III-V materials these dimensions have to be compared with the typical bulk exciton Bohr radius of about 10 nm, thus the strong confinement approximation is at least valid for the z direction.

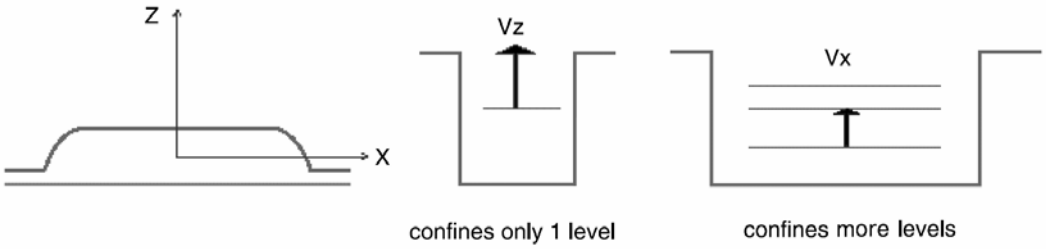

Figure 2.4 Stranski-Kastranov QDs are characterised by a strong confinement in the growth direction (z axis), because the extension of the dot in this direction is smaller than in the x-y plane.

Because of the smaller height in comparison to the extension in the x–y plane, the z axis is the main quantization axis. This situation and the corresponding box like potential barriers are presented in fig. 2.4. For small dots only one (electron) energy level is possible in the dots [64], while the shell structure is determined by the dot extension in the x–y plane.
In the "weak confinement" approximation regime $r >> a_B^{exc}$ it is possible to neglect the potential terms in the expression of $\mathcal{H}_e$ and $\mathcal{H}_h$ and the Hamiltonian without the exchange term is separable into the relative and center of mass motion of the electron-hole pair, with the confining potential acting only on the center of mass motion.

2.3.2 Towards a more realistic treatment

A further improvement of the theory is accomplished considering different effective masses and dielectric constants inside and outside the dots, non parabolicity of the semiconductor band structure, complexity of the valence band, strain induced effects and piezoelectricity. A change in the radial distribution of the electron and hole wave functions is obtained from calculations including Coulomb interaction and the finite barrier height. The Coulomb interaction perturbs the carrier's wave functions and the heavier particle is pushed towards the center of the dot. This effect combined with the fact that electrons and holes can penetrate in the barrier, leads to a mismatch of the corresponding wave functions and consequently to an enhancement of exchange and correlation effects.
The lattice constant mismatch causes the presence of strain at the interface of the two materials. As the unit cell of the crystal is deformed by strain, the bond lengths and angles change. This in turn influences the band structure. At the gamma point of the Brillouin zone, the conduction band is not coupled to the valence band and

the strain induced modification of the conduction band edge consists only of a shift proportional to the hydrostatic strain. The valence band on the other hand is much more complicated. All heavy and light hole band edges are shifted by a factor proportional to the hydrostatic strain. Further, the strain introduces a splitting between the heavy and light hole band edges proportional to the biaxial strain. The sign of the biaxial strain can change on the dot-barrier interface, which causes the light-hole and heavy-hole band edges to cross. The presence of strain does not only modify the energy of the bandgap, but also the effective masses of the carriers, which become (strongly) anisotropic. A second strain induced correction to the potential profile of the quantum dot is the piezoelectric potential, consequence of the piezoelectric charge density which is induced by the shear strains. The importance of the piezoelectric field lies in the fact that it lowers the symmetry of the system, for example for pyramidal dots from C_4 to C_2 [65] and spatially separates electrons and holes.
In conclusion a full numerical treatment of the single particle energy levels in a QD has to consider a realistic geometry, the material composition of both dot and barrier, the strain induced effects like band mixing and piezoelectricity and the complex Coulomb interactions between carriers.

2.4 Excitons, charged excitons and multi-exciton complexes

An electron-hole pair in a QD is commonly called exciton like in the bulk, but there are some important differences that have to be kept in mind. First of all in a QD, because of the confinement potential, there is no exciton unbound state, that means the exciton cannot dissociate, unless one of the carriers leaves the dot. Nevertheless the Coulomb interaction between electron and hole in the dot lowers the sum of the single particle energies thus, in analogy to the bulk situation, the resulting energy difference can be considered as a binding energy. This discussion is valid for every "bound" state in the dot, like the one formed by two interacting electron-holes pairs, the biexciton (see next section). Binding energy of an exciton is always positive, because of the direct attraction of electron and hole and the positive contributions of exchange and correlation.
Another difference is that in a QD there are no exciton excited states like in the bulk. In a QD an excited state is formed by a carrier occupying a higher energetic level in the dot potential and not within the carrier mutual Coulomb interaction.

Filling the QDs with more than one electron-hole pair leads to the formation of charged excitons or multi-exciton complexes. Biexcitons and charged excitons energies lie a few meV apart from the exciton energy and the difference is a measure of the binding energy of these complexes. The exciton is a neutral complex and it interacts weakly with other excitons or charges. This implies that shifts in energy levels of these complexes are a result of both, deviations from charge neutrality, i.e., how different are holes from electrons, and of mixing of configurations. The latter is in turn a sensitive function of parameters such as the

ratio of electron to valence hole mass, the confining potential for either carrier, and the number of confined shells. The biexciton binding energy is the subject of the next section. The binding energy of a charged exciton is the difference between the total energy of the interacting particles (electron-hole + carrier) and that of an exciton plus the carrier. This quantity can be positive or negative. A "negative binding energy" means that the state is not a Coulomb bound one, but the confinement prevents it from dissociation. For QD's systems based on III-V elements charged excitons binding energies in the range of a few meV are predicted theoretically and observed experimentally [35][66][67].
Pauli blocking allows no more than two carriers of the same type to occupy the lowest lying two-fold spin degenerate states of electrons and holes in a QD, thus, after filling the ground state, additional carriers have to occupy higher lying states (fig. 2.5). The number of possible excitons in the dot depends on the density of states available for population, which in turn is determined by the size and the confinement range. In QDs with high number of energy states many pairs can occupy the dot, leading to a complex many body problem. In fact, the transition energy of one exciton depends on the number of additional carriers present in the dot, because of the Coulomb interactions between them [68].

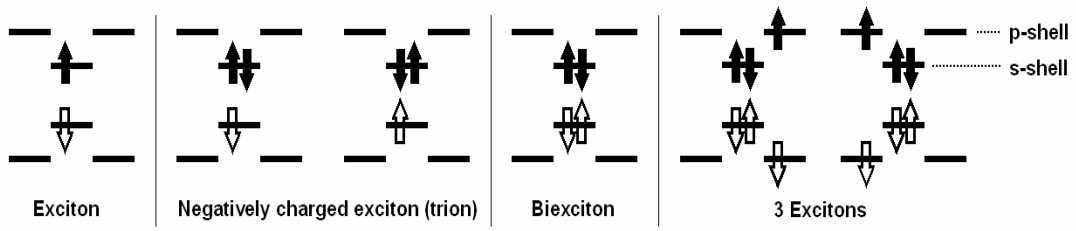

Figure 2.5 Lowest kinetic energy configuration for zero to three excitons and for the negatively charged exciton (trion) in the lowest singlet state. The direction of the arrows indicates the sign of the spin.

2.5 Biexcitons and biexciton binding energy

In semiconductor structures of higher dimensionality (QWRs, QWs, bulk) the biexciton is the bound state of two excitons and the binding energy is defined as the energy gain with respect to two spatially separated excitons:

$$\Delta E_{xx} = 2E_x - E(biexc) \tag{2.5}$$

with E_x and E(biexc) the energies of the exciton and biexciton ground states. Because of the confinement, in QDs there is no unbound state, thus the definition of ΔE_{xx} is no longer appropriate. Nevertheless, like in the case of the exciton binding energy, it is normally used in the literature and it is still useful to describe the experiments.

The binding energy is the result of different aspects of the Coulomb interaction, namely direct attraction or repulsion between carriers, correlation, which is a many-particle effect, and exchange, which regards the particular characteristics of the interacting fermions. The strength of correlation and exchange depends on the spatial overlap between the electron and holes wave functions. In the bulk the biexciton binding energy is much smaller than the exciton binding energy and can in first order be described by correlation and exchange of the two neutral excitons. In general localization of excitons in one ore more directions reduces the exciton Bohr radius, leading to an enhancement of the biexciton binding energy. This effect is attributed [69] to the quenching of the exciton-exciton motion in the biexciton. In the bulk values of less than 1 meV are reported (0,13 meV for GaAs), while an enhancement up to 3,5 meV in GaAs/$Al_xGa_{1-x}As$ QWs [70] and up to about 3 meV in $In_xGa_{1-x}As$/GaAs QWRs [71] has been experimentally observed. It is interesting to study the dependence of the biexciton binding energy on the depth and on the width of a QW. Keeping the width constant and increasing the confinement varying the composition of the well, leads to an enhancement of the biexciton binding energy [72]. On the other side, decreasing the well width, first an increase of the confinement is expected, followed by a decrease for very thin QWs, due to the enhanced penetration of the carrier wave functions into the barriers. Consequently the same behaviour is expected for the dependence of the biexciton binding energy. Indeed theoretical calculations [73] and experimental work shows that, decreasing the well width, first the binding energy increases [69][70], then decreases for very thin wells [74].
The biexciton binding energy in a QD arises from the interplay of the various aspects of the Coulomb interactions between the four spatially confined fermions, under the effect of the confinement potential. The binding contributions come from the direct attraction between carriers of opposite sign and from correlation-exchange effects. In contrast to the case of the single electron-hole pair bound state (the exciton), whose binding energy is always positive, in the biexciton complex a "negative contribution" to the binding energy is present, i.e. the direct repulsion between carriers of the same sign. If this term overcomes the strength of the attractive interaction, the biexciton binding energy takes a negative value (the "anti-bonding" state). In this case the two excitons in the QD do not form a bound state anymore, but the configuration is still stable because of the dot's confinement potential. The relative strength of positive and negative terms depends on the carriers wave functions and their overlap, thus on the structural and chemical properties of the QD and of the surrounding matrix, i.e. size, shape, composition, dielectric properties, strain distribution and strain induced pizeoelectric fields.

Considering as starting point a large dot, the biexciton binding energy is expected to approximate the value in a QW of thickness comparable to the QD height. In dots much larger in size than the exciton Bohr radius (weak confinement regime) an enhancement of ΔE_{xx} is predicted [54] and experimentally observed [75] in CuCl QDs, while reducing the dots size. The same behaviour has been observed in dots with sizes comparable to a_B^{exc}, in the study of etched QDs [36][37][39], where a systematic increase of ΔE_{xx} with decreasing dots size has been found.

Investigations of lithographically defined QDs is possible only down to lateral sizes in the order of 20 nm, because of the intrinsic limitation of this fabrication process.
A further reduction of the QD size leads to an enhancement of the confinement quantization effects, but not to a straightforward increase of the biexciton binding energy. Calculations [55][56] predict for very small InAs/GaAs QDs even a negative value for the binding energy (the "anti-bonding" biexciton state). This effect indicates the overcome of the repulsive Coulomb interaction on the positive terms between the two localized excitons. Many factors contribute to this effect and the balance between them depends on the particular system under study.
The positive contribution to the binding energy due to exchange and correlation is enhanced by the contribution of excited states [76], because of the mixing of excited-states configurations with the biexciton ground-state [44]. Decreasing the size of the dot leads to an increase of the energy separation between ground and excited states and to a depletion of their number. Thus a reduction of the QD's size weakens the positive contribution due to excited states. In particular in ref. [45] is predicted that in truncated pyramidal and pyramidal shaped InAs/GaAs QDs the biexciton can never be a bound state if only direct Coulomb and exchange interactions are considered. Including correlation, a positive biexciton binding energy is found for large dots, which, in the investigated energy region, becomes negative when reducing the size, because of the reduction of the number of bound holes states.
The composition of the dot and of the surrounding matrix plays an important role and influences in many ways the confinement of the carriers and their wave functions. The crystal lattice mismatch between dot and matrix materials is the reason for the strain distribution and the related strain induced piezoelectric quadrupole potential [61]. The piezoelectric field spatially separates electrons and holes, thus reducing the overlap of the respective wave functions and consequently the exchange-correlation interaction. In a large pyramidal-shaped QD the hole wave function is elongated due to the large piezoelectric field, with a density minimum in the center of the dot [61], while the electron (less sensitive to the piezoelectric potential due to its smaller mass) is confined in the center of the dot. This effect leads to a poor electron-hole overlap, resulting in a smaller binding energy. The strength of the piezoelectric effect depends on the piezoelectric modulus of the QD material and on the size of the QD. The piezoelectric quadrupole amplitude scales approximately linearly with the dot's size, thus a weaker charge separation is expected in smaller dots. In this case a reduction of the dot size leads to a larger electron-hole overlap and consequently to an enhancement of the binding energy.
The binding energy increases with the decreasing electron to hole mass ratio, i.e. the heavy hole gives rise to larger binding energies than the light hole [77]. Composition and strain distribution of the dot determine the effective masses of the carriers [65] and consequently the influence of the confinement potential on the wave functions and their overlap. Furthermore, due to its smaller effective mass, the electron is not as strongly confined as the hole. Reducing the size of the dot the electron wave function extends further into the barrier than the hole one, decreasing the overlap between them and the positive contribution to the binding energy due to exchange and correlation.

Another material related effect is the dielectric confinement, due to the difference on the dielectric constants of the QD and the matrix material [78]. A smaller value outside the dot weakens the screening of the Coulomb interaction between electrons and holes and thus enhances the binding energy. The strength of this effect depends on the difference between dielectric constants (small for the InGa/GaAs system[1]) and on the size of the QD, for which the critical value is on the order of the electron-hole separation, namely the exciton Bohr radius. In a QD of size larger than the exciton Bohr radius the dielectric confinement is not effective, while reducing the size of the dot an enhancement of the Coulomb interaction is expected. The discussed factors which contribute to the biexciton binding energy and their dependence on the QD's size are reassumed in table 2.1.

	Effect on ΔE_{xx} due to decreasing dot's size
Excited states	Decrease
Piezoelectric effect	Increase
Effective mass effect	Decrease
Dielectric confinement	Increase

Table 2.1 Factors which influence the dependence of the biexciton binding energy ΔE_{xx} on the QD's size.

Furthermore the QD's shape is predicted to have a great impact on the carriers wave functions and their overlap, thus on the biexciton binding energy. In small pyramidal InAs/GaAs QDs an anti-bonding biexciton state is predicted, while, keeping the dot's volume constant and reducing the aspect ratio, thus changing the shape from pyramid to truncated pyramid, the state becomes a bound one [57]. This effect is due to the decrease of the spatial separation between carriers in flat QDs, with a consequent increase of the wave function overlap and of the positive contributes to the binding energy. Indeed in a small flat QD the electron and holes wave functions present an optimal overlap, with the hole more strongly localized than the electron, because of the larger effective mass. On the other hand, like already explained, in a large pyramidal-shaped QD the piezoelectric field leads to a poor electron-hole overlap, resulting in a smaller binding energy.

This discussion shows that the wave functions of the confined carriers, and consequently the biexciton binding energy, are determined in a very complex way by the geometrical and chemical characteristics of the dots. Because of the impossibility of a direct comparison of theoretical predictions and experiments, an important role is played by statistical studies of many dots, which may lead to a better understanding about the interplay of all these factors. To be mentioned is that the different shapes of the QD's localization potentials should, in turn, give rise to an inhomogeneous broadening of the biexciton binding energy, even for a fixed energy of the localized excitons.

[1] $\Delta\varepsilon_r = 1{,}97$

2.6 Exciton and biexciton fine structure

The last term in the Hamiltonian (2.1) describes the electron – hole exchange interaction, which couples the spins of the electron and hole. This interaction depends on the symmetry of the confinement potential. The break of this symmetry leads to a fine structure splitting of the originally degenerated exciton energy levels given by the confinement and Coulomb part of $\mathcal{H}$. The general form of the spin Hamiltonian $\mathcal{H}_{exchange}$ of an exciton formed by a hole with spin J_h and by an electron with spin S_e is given [79] by

$$\mathcal{H}_{exchange} = -\sum_{i=x,y,z} \left(a_i J_{h,i} S_{e,i} + b_i J_{h,i}^3 S_{e,i} \right) \tag{2.6}$$

with the *z* direction chosen to point along the QDs growth direction, a_i and b_i the spin-spin coupling constants along the three axis.
Due to the complex valence band structure it is necessary to distinguish between light (LH) and heavy (HH) holes. The confinement leads to an energy separation between the heavy and light hole state, where the lowest energy state is given by the heavy hole state. Due to strain in self assembled QDs, the heavy- and light-hole states are split in energy by at least several tens of meV. This splitting is considerably larger than the fine-structure interaction energies, and the light-hole states can safely be neglected. Therefore the single particle from which the exciton is constructed consists of a heavy hole with $J_h = 3/2,\ J_{h,z} = \pm 3/2$ and an electron $S_e = 1/2,\ S_{e,z} = \pm 1/2$. From these states four heavy hole excitons configurations are possible, which are degenerate if $\mathcal{H}_{exchange}$ is neglected, characterized by their angular momentum projections $M = S_{e,z} + J_{h,z}$. States with $|M| = 2$ cannot couple to the light field and are optically inactive (dark excitons), while states with $|M| = 1$ are optically active (bright excitons). Using the $|\pm 1\rangle$ and $|\pm 2\rangle$ exciton states as base, the following matrix representation is obtained for the Hamiltonian [79]:

$$\mathcal{H}_{exchange} = \frac{1}{2} \begin{pmatrix} \Delta_0 & \Delta_1 & 0 & 0 \\ \Delta_1 & \Delta_0 & 0 & 0 \\ 0 & 0 & -\Delta_0 & \Delta_2 \\ 0 & 0 & \Delta_2 & -\Delta_0 \end{pmatrix} \tag{2.7}$$

The matrix has a block diagonal form, thus bright and dark states do not mix with each other, and their energies differ by the electron-hole exchange energy Δ_0. For symmetric QDs $\Delta_1 = 0$ and $|\pm 1\rangle$ are eigenstates of $\mathcal{H}_{exchange}$, thus the ground state is double degenerate, and the emission is circularly polarized. Dark excitons always hybridize, and the energy splitting is equal to Δ_2.

If however the rotational symmetry is broken, the degeneracy of the bright states is split by the exchange interaction into two closely spaced levels splitted by Δ_1. In QDs with $L_z << L_x, L_y$ the splitting between bright and dark excitons is expected to be much larger than the energy splitting of the bright exciton doublet ($\Delta_0 >> \Delta_1$). Therefore the mixing of $|\pm 1\rangle$ and $|\pm 2\rangle$ states is small, and the radiative states are symmetric and antisymmetric linear combinations $\left(|+1\rangle \pm |-1\rangle\right)/\sqrt{2}$ with energies $\left(\Delta_0 \pm \Delta_1\right)/2$. Thus the optical transitions are expected to be linearly polarized along the principal QD axis. In general, both splittings should be small compared to Δ_0, because they are given by the coupling matrix elements that are proportional to J_h^3. The energy levels and the allowed optical transitions of the exciton and biexciton states for an isotropic ($D_{2d} - C_{4v}$ point group symmetry) and anisotropic ($< D_{2d} \rightarrow C_{2v}, C_2$) QD are presented in fig. 2.6. The fine structure of the biexciton emission is identical to that of the exciton because the biexciton is a spin-singlet state and does not exhibit exchange splitting. Therefore, in the optical spectra any fine structure of the E_{xx} emission and its polarization are fully determined by the final state of the electron-hole recombination, i.e. the eigenstates of the single exciton.

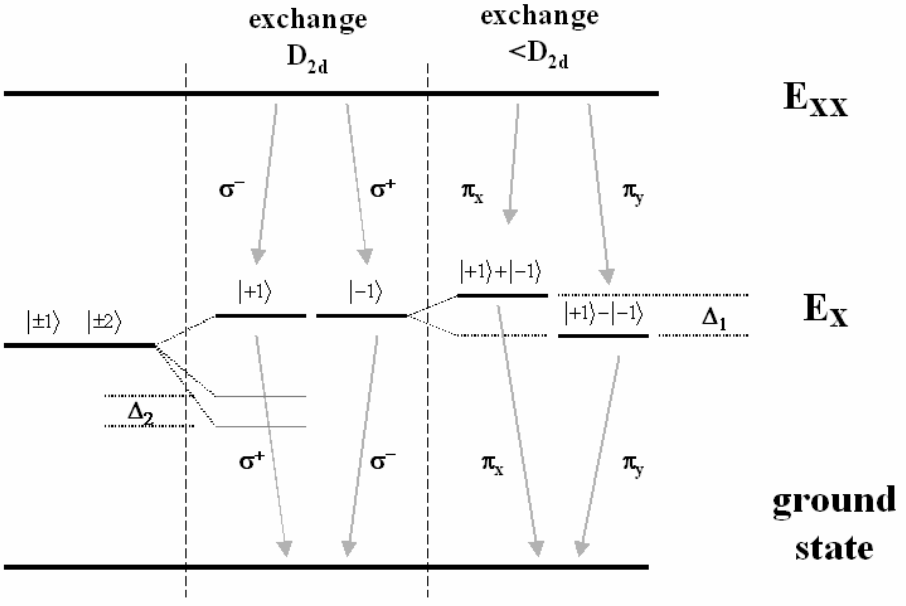

Figure 2.6 Exciton (E_x) and biexciton (E_{xx}) emission structure without exchange, with exchange in a symmetrical confinement and the fine structure in dots of lower symmetry. Polarization of the transitions is indicated.

The energy sequence of the polarized components is different for the E_x and E_{xx} doublets: for the exciton the π_x polarized component is the higher energetic one, while for the biexciton this is true for the π_y polarized component. In most cases the polarization is oriented along the [110] and [1$\bar{1}$0] crystal orientation axis.

To be mentioned is the work of Bester *et al.* [80] where pseudopotential calculations have been performed to model lens shaped symmetric InGaAs/GaAs QDs. The symmetry is broken at atomistic level, leading even for shape symmetric dots to a splitting of bright states and to strong polarization anisotropy. Asymmetry in the dot shape tends to increase this splitting.

2.7 Linewidth

Considering a two level system, the excited state undergoes a spontaneous emission resulting in a finite radiative lifetime. Additionally interactions with the environment such as lattice vibrations and Coulomb interactions with other carriers may influence the lifetime. It is in general complicated to account for these effects since the dynamics of a large number of other particles have to be considered. In a simple approach the time evolution of the system is described by an exponential decay to the equilibrium value, with the introduction of a phenomenological damping constants, related to the two types of relaxation that can be distinguished. One is phase relaxation, where the phase of the state is changed but the occupation can remain and the other is energy relaxation, where both phase and occupation are changed. The homogeneous linewidth of a transition is related to the total dephasing rate T_2, given in general by the excited state lifetime term T_1 plus a pure dephasing term $T_2^{'}$ describing the pure (elastic) phase relaxation which does not change the occupation of the state:

$$\frac{1}{T_2} = \frac{1}{2T_1} + \frac{1}{T_2^{'}} \tag{2.8}$$

Energy relaxation is described by the first term T_1, which is the lifetime of the specific state, e.g. the decay time of the exciton (population) in the QD, such that the system returns to its ground state due to the spontaneous emission. The second term comprises all random phase changes caused by elastic scattering processes, resulting in a decay of the macroscopic polarization additional to the one given by the population damping. T_1 and T_2 are also know as the longitudinal and transverse relaxation time, respectively, in analogy with the theory of magnetic resonance. The factor of two between the elastic dephasing rate $T_2^{'}$ and the radiative one T_1 originates from the direct proportionality of the polarization to the amplitude of the occupation probability of the excited state, while the population inversion is proportional to the square of this amplitude. The incoherent part of the intensity decays exponentially

$$I_{incoh} \propto \exp\left(-t/T_1\right) \tag{2.9}$$

while the coherent part of the intensity has a quadratic dependence on the polarization

$$I_{coh} \propto \left|P(t)\right|^2 \propto \left|\exp\left(-t/T_2\right)\right|^2 = \exp\left(-2t/T_2\right) \tag{2.10}$$

This yields in case of purely radiative damping ($I_{incoh} = I_{coh}$): $2T_1 = T_2$. While the occupation of a state remains unchanged during the pure phase relaxation, for energy relaxation this is not the case. Two groups of processes can be distinguished, both fulfilling energy conservation. The radiative recombination is always connected with the emission of an electromagnetic wave. In contrast, the non-radiative recombination is connected with the transfer of energy to the lattice by the emission of phonons, population of other states lower in energy, or other non-radiative processes. The total life time T_1 can be split in two terms in accordance to the two processes in the form:

$$\frac{1}{T_1} = \frac{1}{T_{rad}} + \frac{1}{T_{non-rad}} \tag{2.11}$$

The dephasing time T_2 describes the damping constant of the macroscopic polarization and it is connected with the homogeneous broadening of the transition emission line by

$$\Gamma = \frac{2\hbar}{T_2} \tag{2.12}$$

The introduction of the damping constants T_1 and T_2 is the simplest approximation to describe the relaxation of the system to its equilibrium, which is also called the relaxation-time approximation. In the absence of interactions with phonons and other carriers and of non-radiative recombination channels, the dephasing time in QDs is limited by the radiative decay. Theoretical studies of the radiative lifetime of ground state excitons in structures going from QDs in the strong confinement regime to QWs are presented in ref. [81]. For QDs in the strong confinement regime a radiative lifetime of about 1-2 ns is predicted, which is independent of the dot size. The corresponding full width at half maximum (FWHM) homogeneous broadening is less than 1 μeV. In the case of an intermediate size range and of weak confinement T_{rad} decreases with increasing dots size [82]. This is the regime of QW thickness fluctuation dots for which a value of ~100 ps have been observed.

2.7.1 Homogeneous and inhomogeneous broadening

Broadening mechanisms are of homogeneous type (coupling to different types of phonons, scattering at defects or interfaces, scattering within a many-particle system of interacting electrons and holes) and of inhomogeneous type as dot size fluctuations (in the case of ensembles of dots) or spectral jitter of the single dot luminescence emission energy.

If there is a set of states, which undergo a radiative recombination to lower lying states, all with the same transition energy $\hbar\omega$, the total emitted electric field can be described by a decaying wave with a central frequency corresponding to the transition energy. The electric field reads:

$$E(t) = E_0 \exp\left(-\frac{\Gamma}{2}t\right)\exp(i\omega t) + c.c. \tag{2.13}$$

In the spectral domain this damping yields a spectral broadening. $E(\omega)$ can be calculated taking the Fourier transformation of (2.13). Since the measured spectrum corresponds to the intensity $I(\omega) = E(\omega)E^*(\omega)$, this yields with the assumption $\omega - \omega_0 << \omega_0^2$

$$I_{\omega_0}(\omega) \propto \frac{\Gamma}{(\omega-\omega_0)^2 + (\Gamma/2)^2} \tag{2.14}$$

which is a Lorentzian line profile. Its full width at half maximum $\Delta\omega_{FWHM} = \Gamma$ is called natural linewidth and its given only by the finite lifetime of the upper state and the loss of phase memory by elastic scattering processes.

Inhomogeneous broadening is given if the transition energy $\hbar\omega$ is not well defined. During the formation of QDs, fluctuations of the morphological characteristics in the ensemble will occur, leading to differences in the ground state emission energy between dots, thus to inhomogeneous broadening effects in the optical spectra of ensembles. Or if the ground state energy of an exciton in a single QD is jittering in time, the time integrated PL will be also inhomogeneously broadened. The line profile in this case will be strongly dependent on the distribution function $g(\omega, \omega_0, \gamma)$ for ω centred at ω_0 with the characteristic width γ. The resulting spectral line profile is defined by the convolution between the Lorentzian profile from the homogeneous broadening and $g(\omega, \omega_0, \gamma)$ and can be written as:

$$I_{inhom} = \int_{-\infty}^{\infty} \frac{\Gamma(\omega')}{(\omega' - \omega_0)^2 + \Gamma(\omega')^2} g(\omega', \omega_0, \gamma) d\omega' \tag{2.15}$$

Often $g(\omega, \omega_0, \gamma)$ is a Gaussian distribution, but it can be non-Gaussian. Which of both distributions dominates the final line profile depends on the relation between γ and Γ and can be Lorentzian ($\Gamma > \gamma$), Gaussian ($\gamma > \Gamma$) or the Voigt profile ($\Gamma \approx \gamma$).

2.7.2 Linewidth temperature dependence

The temperature dependence of the homogeneous linewidth $\Gamma(T)$ of the exciton emission line is determined by its interaction with phonons, an argument which has

been subject of a lot of theoretical and experimental investigations and is not fully understood yet. In a solid crystal, with increasing temperature, the inelastic scattering of the exciton by acoustic or optical phonons reduces the exciton lifetime and broadens the exciton line. In such a mechanism the loss of population of the radiative state induces a loss of phase coherence (dephasing). Energy relaxation processes in QDs have been believed to be slowed down as compared to systems of higher dimensionality.

The relaxation in QD structures assisted by low energy acoustic phonon was predicted theoretically to be inefficient because of the absence of suited states between the QD discrete energy levels, the so-called phonon bottleneck effect [83]. Moreover a strongly reduced exciton relaxation via emission of longitudinal optical (LO) phonons is predicted, unless the energy spacing equals the LO-phonon energy [84]. The results of the experiments do not clearly show the predicted bottleneck effect and their interpretation is still controversial. Depending on the particular system under investigation, different reasons have been proposed for the observed efficient relaxation (fig. 2.7): in the case of high excitation power Auger scattering processes [85] may play an important role, while at low carrier densities possible relaxation channels comprise multi-phonon processes [86], acoustic phonons scattering of holes with closer energetic levels than electrons [87], presence of a continuum of states to the QD emission from the wetting layer [88], enhanced LO coupling because of the presence of a dipole moment in the dot [89].

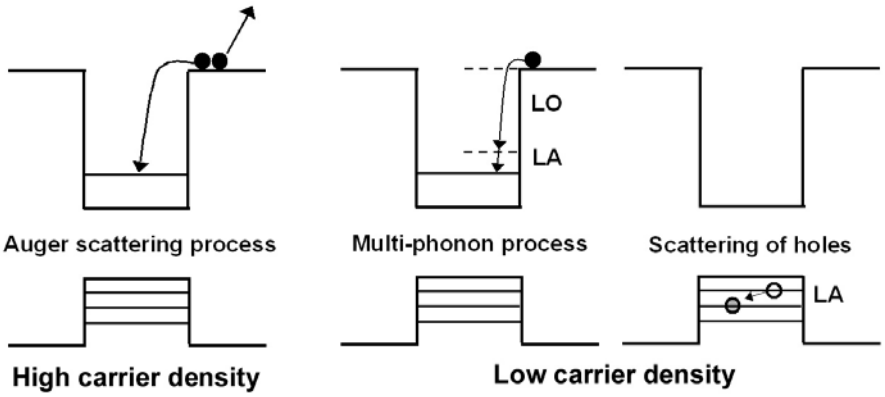

Figure 2.7 Carrier relaxation processes: Auger scattering under high excitation density, multi-phonon processes and LA-phonon scattering of holes under low excitation density.

With increasing temperature the linewidth of the PL emission lines increases, because of the interactions between excitons and thermally created phonons. The experimental temperature dependence of the linewidth $\Gamma(T)$ of the zero phonon line (ZPL) shows a linear and an activated behaviour [20][28][130], i.e. can be expressed as

$$\Gamma(T) = \Gamma_0 + AT + \frac{B}{\exp(E_A / k_B T) - 1} \tag{2.16}$$

Γ_0 is the homogeneous linewidth, which is nearly constant with the temperature. The linear term gives the acoustic phonon scattering, while the activated one gives the scattering with optical phonons. At low temperatures ($k_BT << \hbar\omega_{LO}$) the third term does not play a role because of the negligible LO phonon population, while the acoustic phonon assisted transitions to higher energy exciton states contribute to population decay, leading to a linear dependence on the temperature [90]. This inelastic acoustic phonon scattering increases with the temperature, broadening the transition. In QDs, due to an absence of final states with suitable energy, the phonon induced population decay is reduced and a low thermal broadening is expected. At higher temperatures the activated temperature dependence is due to optical phonon assisted transitions to excited exciton states. The resulting strong increase of the linewidth depends on the electronic shell structure, thus on the geometry of the QDs.
The described temperature dependence involves inelastic scattering of excitons and phonons. With increasing temperature, elastic interactions with acoustic phonons also contribute to dephasing [91]. This pure dephasing effect has been demonstrated for the CdTe/ZnTe QD system by Besombers [92] and Favero [93] for InAs/GaAs QDs: in both works the QD exciton emission linewidth develops a non Lorentzian shape with the appearance by increasing temperature of side bands on both sides of the zero phonon line (ZPL). The broad background originates from exciton-phonon interactions. Theoretical calculations agree with the experimental results and show that for large QDs the exciton-phonon band narrows and is masked by the width of the ZPL.

The strength of the coupling with acoustic and optical phonons is determined by the geometry and composition of the dot. For large QDs with small interlevel spacing the longitudinal acoustic (LA) phonon scattering rate is dominant and leads to a lifetime limited linewidth which is proportional to temperature [94]. For small QDs and large interlevel spacing phonon scattering is predicted to be less effective. Furthermore since the coupling strength of excitons with LO phonons depends on the local charge density and thus on the difference between the electron and hole wave functions, geometrical and material characteristics of the dots have a great influence. Pyramidal dots with high aspect ratio present a high dipole moment and thus can be strongly coupled to LO phonons, leading to the formation of excitonic polarons. On the other side in flat truncated pyramidal QDs a more similar shape of electron and hole wave functions is predicted and exciton relaxation is suppressed [95]. In conclusion, both phonon types influence the broadening of the linewidth of the excitonic emission with the temperature, in a rather complicated way, which strongly depends on the dots characteristics.

2.7.3 Carrier-carrier scattering and spectral diffusion

Other effects that cause the broadening of the QD emission linewidth are the interaction between carriers and the effect of local electric fields. It is generally found that with increasing number of carriers, both inside the dots and in the

wetting layer and surrounding barrier, the homogeneous broadening of the transitions increases. Two mechanisms of homogeneous broadening due to Coulomb interactions were found to be important, pure dephasing due the influence of carriers outside the dot and multi-excitonic effects between levels in the dot [96][97].
Not only the direct carrier-carrier interactions affect the emission linewidth: local electric fields like those of defects, impurities, or localized charges in the vicinity of a QD will strongly influence its electronic structure and thus the emission characteristics. Spectral diffusion is caused by the quantum-confined Stark effect (QCSE) [98] due to statistical variations of these local electric fields acting on the dots. The electric field separates the electron and hole wave functions, resulting in an overall net reduction in energy of the electron-hole pair and a corresponding Stark shift. This effect have been observed in nanocrystalline QDs [99], in self-assembled CdSe/ZnSSe [100] and CdSe/ZnSe [101] QDs, where shifts up to 1 meV and time constants in the range of seconds to tens of seconds have been measured. II-VI structures with high background doping are characterised by a density of charged defects an order of magnitude larger than in comparable III-V structures. For this reason this effect is expected to be small in QDs structures based on III-V materials. Ref. [45] reports about the observation of the jitter in the InAs/GaAs system: this effect has been used to identify the emission lines arising from recombination in the same QD. Due to the random distribution and population of defects each QD is exposed to a different electric field and, furthermore, the strength of the effect depends strongly on the geometrical extent of the QD. Thus each QD exhibits its own characteristic jitter.
Other effects related to the influence of local electric fields are the on/off switching called random telegraph noise [102] and the two-color blinking of the excitonic emission in a single QD [103]. An interesting effect is presented in ref. [104] where it is shown, that for CdTe QDs the QCSE induced energy shifts for exciton, biexciton and charged excitons are not identical. This effect would lead to different linewidths in time integrated measurements.

2.8 Temperature dependence of the semiconductor energy gap

The dependence on the temperature of the optical spectra of crystals results from the interaction of the electronic states with the vibrations of the lattice (electron-phonon interactions). Transition energies of QDs are thus subject to thermal drift, which is caused in first order by the temperature dependence of the band gaps of the respective semiconductors. The gap shrinkage effect in semiconductors represent a cumulative effect produced partly by electron-phonon interactions and partly by thermal lattice expansion, whereby the first mechanism is usually the dominating one at low temperatures [105][106]. At high temperatures, both contributions lead to a linear change of the band-gap energy and, depending on the material, can have similar magnitude.

The lattice phonons influence the bonding energy and consequently the band gap through various orders of the electron-phonon interaction. Since this effect depends on phonon numbers, the dependence on the temperature should take a form proportional to the Bose-Einstein occupation factor $\overline{n}\left(\varepsilon_{\mathbf{q}j},T\right)$, where $\varepsilon_{\mathbf{q}j}$ indicates the energies of the individual phonon modes **q**j. Thus the contribution to the energy shift can be represented in the form of an integral $\int f_{e-ph}(\varepsilon)\overline{n}(\varepsilon,T)d\varepsilon$ [107], where $f_{e\text{-}ph}$ is a spectral function related to the electron-phonon interaction $f_{e-ph}(\varepsilon)\propto C(\varepsilon)D(\varepsilon)$. In this relation $D(\varepsilon)$ is the density of phonon states and $C(\varepsilon)$ accounts for the energy dependence of the coupling strength in the corresponding spectral region.

The thermal expansion of the lattice results from anharmonic terms in the expression of the crystal energy vs. atomic displacement and causes a change in the atomic wave-function overlap. Typically, a decrease of the lattice constant causes an increase of the band gap and vice versa. The contribution to $E_g(T)$ is generally proportional to the thermal induced change of the volume, which can be represented again in the form of an integral along the ε axis proportional to the phonon occupation factor $\overline{n}\left(\varepsilon_{\mathbf{q}j},T\right)$ and with a mechanism specific spectral function $f_{thermal}(\varepsilon)\propto\gamma(\varepsilon)\varepsilon D(\varepsilon)$ (where $\gamma(\varepsilon)$ are the Grüneissen parameters [107]). The thermal expansion effect is in general smaller than the contribution from the electron-phonon interaction and presents a very flat behaviour at low temperatures. This effect can be evaluated with a formula proposed by Biernacki [106], which gives for GaAs a very small contribution of less than 100 μeV for T < 60 K.

Since phonon and lattice contributions to the band gap shift have a similar averaged temperature dependence, it is possible to include both in an unique integral equation of the form

$$E_g(T)=E_g(0)-\int f(\varepsilon)\overline{n}(\varepsilon,T)d\varepsilon \tag{2.17}$$

with $E_g(0)$ the bandgap at zero temperature and $\overline{n}(\varepsilon,T)$ the thermally averaged phonon occupation number in the corresponding spectral region

$$\overline{n}(\varepsilon,T)=\frac{1}{\exp(\varepsilon/k_BT)-1}=\coth\left(\frac{\varepsilon}{2k_BT}\right)-1 \tag{2.18}$$

The relevant total spectral function $f(\varepsilon)$ is given by the sum of contributions due to both mechanism. For $z\equiv\hbar\omega/2k_BT<\pi$ (region of intermediate to high temperatures) its possible to expand the $\coth(z)$ function into a corresponding Taylor series

$$E_g(T) \to E_g(0) - \alpha\left(T - \frac{\Theta}{2}\right) - \frac{1}{2}\left(\frac{M^{(1)}}{6k_B T}\right) - \ldots \tag{2.19}$$

where $M^{(m)}$ denotes the moments of the spectral function

$$M^{(m)} \equiv \int \varepsilon^m f(\varepsilon)\, d\varepsilon \ , \quad m = -1, 0, +1, +3 \ldots \tag{2.20}$$

The empirical standard parameters α and Θ are generally defined in terms of the two lowest-order moments as

$$\alpha \equiv k_B M^{(-1)} \equiv k_B \int \frac{f(\varepsilon)}{\varepsilon} d\varepsilon \tag{2.21}$$

and

$$\Theta \equiv \frac{M^{(0)}}{k_B M^{(-1)}} \equiv \frac{1}{\alpha} \int f(\varepsilon)\, d\varepsilon \tag{2.22}$$

The series expansion ceases to converge at temperatures lower than about Θ/π, thus its inapplicable to the cryogenic region. On the other hand fitting of experimental data requires an analytical expression applicable to arbitrary temperatures, from below liquid helium to above room T for a whole class of semiconductors. This is obtained with the choice of a physically reasonable model for the spectral function $f(\varepsilon)$. A spectral function of a power-law type $f(\varepsilon) = C\varepsilon^{\nu}$ up to a certain cut-off energy ε_0 and $f(\varepsilon) = 0$ elsewhere, with ν empirical exponent, have been proposed by Pässler [108] and leads to an approximate expression for $E_g(T)$, which gives very good fits to the experimental data. With the use of relations (2.21) and (2.22) the spectral function can be represented in terms of the basic empirical parameters

$$f(\varepsilon) = \nu \frac{\alpha}{k_B}\left(\frac{\varepsilon}{\varepsilon_0}\right)^{\nu} \quad \text{and} \quad \varepsilon_0 = \frac{\nu + 1}{\nu} k_B \Theta \tag{2.23}$$

Inserting (2.23) into (2.17) it is possible to use the obtained integral formula to fit the data, or to derive a simpler analytical representation from it, of the form

$$E_g(T) = E_g(0) - \frac{\alpha \Theta_p}{2}\left[\sqrt[p]{1 + \left(\frac{2T}{\Theta_p}\right)^p} - 1\right] \tag{2.24}$$

which approximates very well the integral equation in particular for exponents $p = \nu + 1$ within a range of about $2{,}2 < p < 2{,}5$. More realistic and complicated spectral functions [109] lead to better approximations, but eq. (2.24) have been proved to fit very well to the experimental data for a wide range of semiconductor materials [110].

The parameters which enter this fitting formula are related to specific material characteristics. It is important to remember that because of the dependence of the gap shrinkage on both phonon mediated mechanisms, the moments $M^{(m)}$ are different from those associated with the mere phonon density of states $D(\varepsilon)$ in a given material. The low temperature asymptote is given by a power law $E_g(0) - E_g(T) \propto T^p$. The curvature of the non linear part of $E_g(T)$ is related to the position of the center of gravity $\langle \varepsilon \rangle$ and to the effective width[2] $\Delta\varepsilon = \sqrt{\langle \varepsilon^2 \rangle - \langle \varepsilon \rangle^2}$ of the relevant spectrum of phonon modes that makes a substantial contribution to the observable $E_g(T)$ dependence. From eq. (2.23) and the identity $p = \nu + 1$ it follows that the fractional exponent p is connected to the degree of phonon dispersion $\Delta\varepsilon / \langle \varepsilon \rangle$ by the approximated relation

$$\frac{\Delta\varepsilon}{\langle \varepsilon \rangle} \approx \frac{1}{\sqrt{p^2 - 1}} \tag{2.25}$$

At high temperatures $E_g(T)$ tends towards a linear asymptote of the form

$$E_g(T) \to E_g(0) - \alpha\left(T - \frac{\Theta_p}{2}\right) \tag{2.26}$$

Here the parameter α represents the $T \to \infty$ limiting magnitude of the slope, which is the entropy

$$\alpha = \lim_{T\to\infty} \frac{dE(T)}{dT} = S(\infty) \tag{2.27}$$

The center of gravity $\langle \varepsilon \rangle$ is represented in a temperature scale by a corresponding average phonon temperature

$$\Theta_p \approx \Theta \equiv \frac{\langle \varepsilon \rangle}{k_B} \tag{2.28}$$

The approximated relationship between the average phonon temperature Θ and the empirical value Θ_p is a consequence of the already explained approximated nature of the used fitting formula. For a given material Θ amounts to about 2/3 of the associated Debye temperature (Θ_D) [111]. The effective phonon temperature Θ allows an estimation of the relative weights of the contributions of various sections of the phonon energy spectrum to the measured $E_g(T)$ dependence [111].

[2] Defined as the root mean square (RMS) distance from the center of gravity of the phonon spectrum

3. The InAs / InGaAs quantum dots sample

3.1 Sample growth

The quantum dot samples investigated in this work consist of self-assembled InAs QDs embedded in an InGaAs QW surrounded by a GaAs matrix. The QDs are of type I for which electrons and holes are both confined in the dot (for type II dots one type of carrier is confined while the other remains in the barrier). The InGaAs QW red shifts the emission of the InAs QDs in comparison to the InAs/GaAs ones. This effect is due to several reasons. The energy levels of the dot are sensitive to the bandgap of the surrounding material, thus embedding the dots in an InGaAs structure causes a decrease in energy and a red shift of the emission energy. The Stranski-Krastanov growth of InAs on InGaAs should lead to larger QDs due to the smaller lattice misfit. Furthermore, strain driven surface kinetics leads to a partial decomposition of the InGaAs capping layer during growth [112] and to preferential incorporation of indium at already existing InAs islands which also counteracts the effect of In-Ga intermixing in the dots. Finally, the In concentration in the dots is enhanced and the size is increased which leads to lower energy levels and redshift of the emission energy.
The QDs sample were grown by molecular beam epitaxy (MBE) on a semi-insulating GaAs (100) substrate. The growth sequence started with a 500 nm GaAs buffer layer followed by the growth of the lower cladding layer which consists of a 10 period AlAs/GaAs (2,5 nm / 2,5 nm) superlattice structure. Also the subsequent 30 nm GaAs layer and the 5 nm $In_xGa_{1-x}As$ ($x \sim 0{,}12$) layer were grown at a substrate temperature of $T_S = 600°C$ before T_S was reduced to 520°C for InAs deposition during a growth interruption of 10 minutes. Wafer rotation was stopped in order to monitor the self-assembled QD formation by RHEED and to achieve a gradient of InAs coverage across the diameter of the wafer (about ±15% with respect to the centre of a 2" wafer due to the MBE geometry). InAs was grown with a slow growth rate of about 0,01 monolayers/s (calibrated to the centre of the wafer) and after deposition of nominally 1,2 monolayers of InAs the streaky RHEED pattern becomes spotty which indicates the start of 3-dimensional island

growth. Immediately, InAs growth was stopped to ensure that the early stage of QD formation was conserved to obtain areas on the wafer with very low QD density between the areas without QDs on the InAs wetting layer and areas with a high QD density. After a growth interruption of 10 minutes the QDs were covered symmetrically with a 5 nm $In_xGa_{1-x}As$ (x ~ 0,12), a 30 nm GaAs layer, the upper cladding layer (10 periods AlAs/GaAs (2,5 nm / 2,5 nm) superlattice) and a 7,5 nm GaAs cap layer. The superlattice barriers were grown to avoid diffusion of photo-excited carriers to the GaAs bulk and to the sample surface which results in a stronger photoluminescence intensity. The structure of the sample is presented in the cross section TEM image of fig. 3.1.

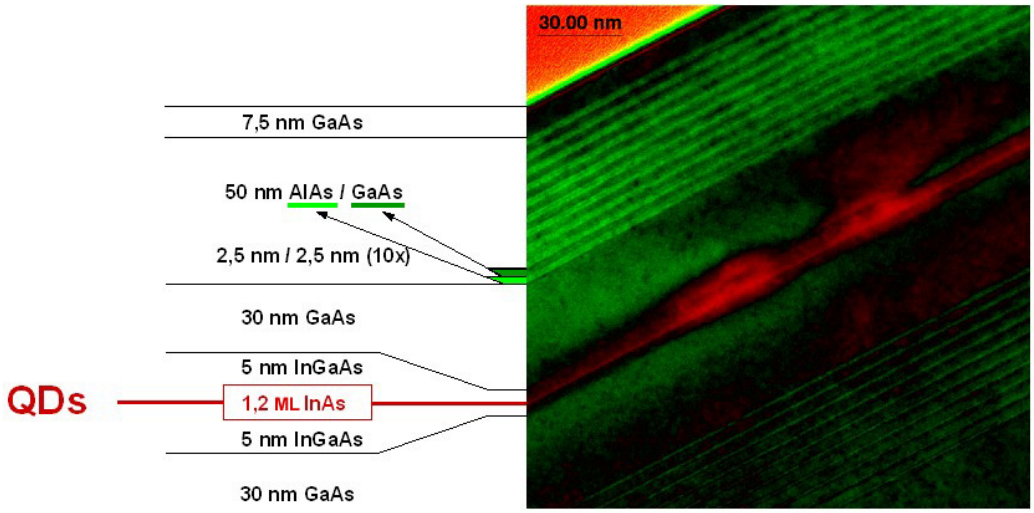

Figure 3.1 TEM image and schematic structure of the investigated InAs on $In_{0,12}Ga_{0,88}As$ sample (ML = monolayer).

A ~5 mm large slice was cut from the 2'' wafer parallel to the direction of the dots density gradient. This slice was divided into three samples 611-x (x = 1, 2, 3), the order indicating increasing dot densities.

3.2 QDs shape and dimensions

Uncapped samples for SFM characterisation were not prepared, but SFM measurements on similar InAs QDs grown on a InGaAs buffer reported in ref. [113] show QDs with an asymmetric truncated pyramid shape and a *length : width : height* ratio of about *2 : 1 : 0,235*.
With cross sectional TEM (transmission electron microscopy) imaging it is possible to investigate the buried islands. Measurements are performed on a very thin specimen of wedge form. Thus it is important to remember, that the observed properties, which are an average over the slice thickness, depend on the location of the structure within the slice. This technique can give precise information about the

height and composition of the dots [41] and even about the strain distribution [42], but only a rough estimation of the lateral dimension is possible, which depends on the position where the cleavage plane cuts the dot.
TEM pictures acquired from our sample in the middle of the wafer (sample 611-2) are of difficult interpretation, because the contrast is due to both material contrast and strain. The dots show a truncated pyramidal form, with a base length in the range of 30 to 40 nm and a height of about 9 nm, thus a *length : height* ratio of about *0,25*. The recorded images show 5 QDs of about the same dimensions. An example of two QDs is given in fig. 3.2.

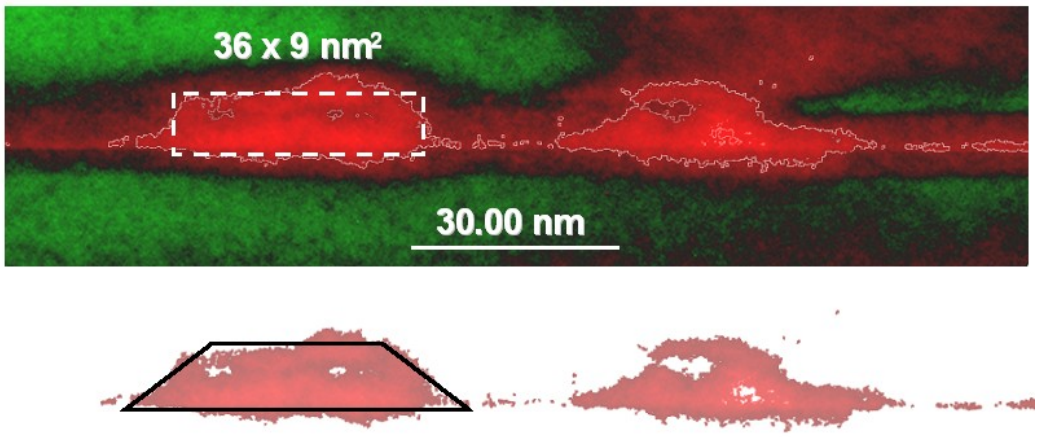

Figure 3.2 TEM image of two QDs of sample 611-2 (in the middle of the 2'' wafer).

Measurements on single QDs have been performed on the 611-1 sample, where the dot density is lower than in the region, where TEM images were taken. Probably the optically investigated dots are slightly smaller. Nevertheless, the main goal of these measurements is to obtain a rough estimation of the dot's dimensions. A comparison with dimensions of QDs studied in published papers is reported in table 6.1.

3.3 Macro-photoluminescence optical characterisation

The first optical characterisation of the sample was carried out at 7 K with a macro-photoluminescence set-up, to check the emission energies of the QDs and the other structure of the sample. The photoluminescence was excited with a He-Ne laser focussed by a f = 400 mm lens to an elliptic spot (60 μm large and 100 μm long). Signal was collected with a f = 300 mm lens and focussed on the entrance slit of a grating spectrometer, with the possibility to switch between a liquid nitrogen cooled germanium detector and a photo-multiplier, to cover the energy range of the sample emission, which spans from about 1 eV to 1,8 eV.

Measurements were performed on the 611-1 and 611-2 samples, with low and intermediate dot densities respectively. Characteristic emission lines can be seen in fig. 3.3a. In order of increasing energies the emission of the QDs (1,05 – 1,25 eV), the InGaAs QW (~1,25 eV), the GaAs matrix (~1,51 eV) and the AlAs/GaAs QWs superlattice structure (~1,8 eV) can be seen. The peak at 1,25 eV has been attributed to the InGaAs QW, because of the constant emission energy on different positions of the sample. No luminescence related to the wetting layer was observed in the PL, most likely because of an efficient transfer of the photoexcited carrier to the QDs.

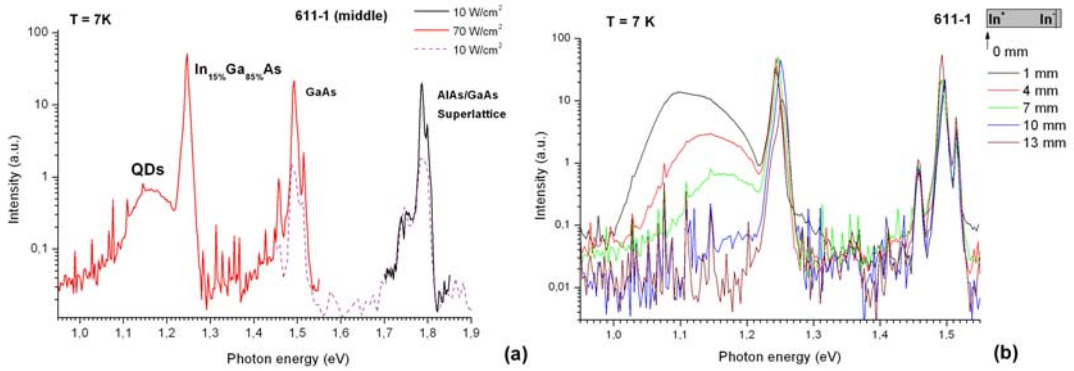

Figure 3.3 Macro photoluminescence measurements on the low dots density sample 611-1: emissions from the different structures of the sample (a) and blue shift of the dot's PL signal with decreasing In concentration (b).

A blue shift of the QD's PL emission peak was found when moving towards the low density region of the sample (fig. 3.3b), due to a decrease of the QD's dimensions. Single QDs spectroscopy experiments were performed at a distance of about 6 mm from the high density edge of the 611-1 sample, corresponding roughly to the green spectra in fig. 3.3b. The QD emission band shows a FWHM of about 100 meV centred at about 1,16 eV.

4. Experimental methods

4.1 The low temperature micro-photoluminescence set-up

To perform micro-photoluminescence experiments at cryogenic temperatures a measurement system has been developed, on the basis of a cold finger cryostat and a Fourier Transform (FT) spectrometer [114][115].
In this work spectroscopy on a single QD is accomplished without modifications of the sample (etching, masking), but performing measurements on a region where the interdot distance is larger than the optical resolution. The very low dots density on sample 611-1, expected after comparison with SFM measurements performed on similar InAs/GaAs QDs samples [114, less than 1 QD pro square μm], does not require a very high optical resolution. On the other hand a long integration time is expected for the acquisition of a single spectra with the FT spectrometer, thus it is of central importance, to have an efficient long term spatial stability of the microscope system and to collect a maximum of the emission from the QDs. Furthermore, the experimental set-up has been designed to work as a combined low temperature SFM and SNOM system, by replacing the conventional microscope objective with one of the special sensor heads developed in our group [116]. The combination with a high resolution SFM positioning system has lead to a straightforward implementation of a scanning mode for the spectra acquisition, thanks to the synchronisation of the spectrometer and the SFM software. This operation mode allows the precise scanning of the sample and the acquisition of a spectrum for each point of a grid in the scanning area. Three dimensional sets of data can be acquired, whose sections at a given energy represent optical images of the sample at that particular emission energy. A schematic view of the whole experimental set-up and its main components is presented in fig. 4.1. The heart of the system is the optical scanning microscope mounted inside the vacuum chamber of the cryostat, which is connected with the laser source and the spectrometer via optical fibers.

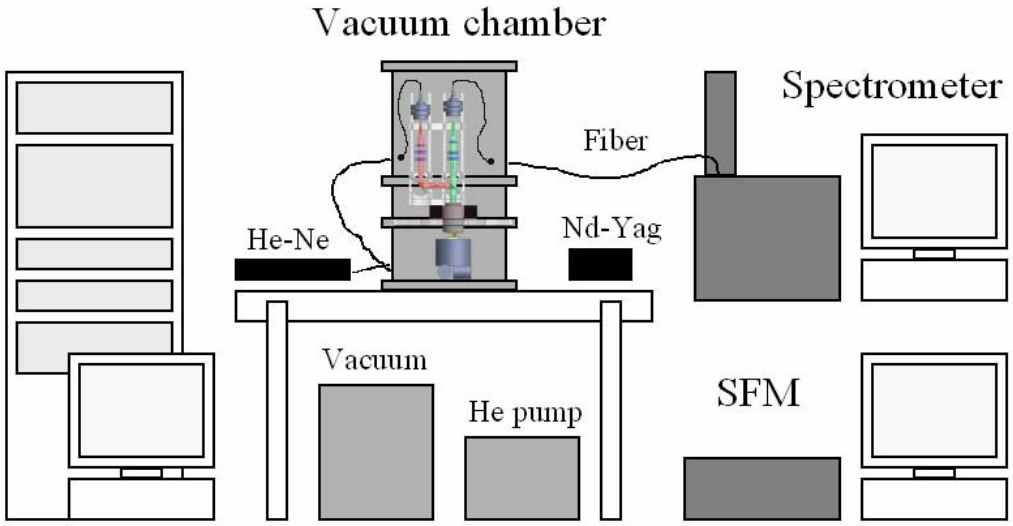

Figure 4.1 Schematic view of the experimental set-up: the scanning optical microscope is mounted inside the vacuum chamber, which is fixed on the top of a pneumatic active controlled table. Laser sources, vacuum pump, liquid He pump, Fourier Transform spectrometer and the control electronics (spectra acquisition, temperature control, scanning and SFM unit) complete the measurement system.

Cooling of the sample is performed with a specially designed cryostat using a liquid helium-cooled cold finger. The homemade microscope and the cold finger are mounted on two independent positioning systems, in particular, the microscope is fixed on top of a piezoscanning stage and the cold finger to a three axis step motor positioning system. This configuration requires a cryostat divided in three sections, to allow an independent access to the optical microscope and to the cold finger where the sample is fixed. The vacuum chamber and the laser sources are fixed on the top of an actively controlled pneumatic optical table (Newport Inc.). The whole system is controlled by three computers (spectrometer, SFM and scanning control, temperature). In the following sections a detailed description of each constituent part is presented.

4.2 The scanning optical microscope

A schematic view of the optical microscope and its actual realization are presented in fig. 4.2. The optical components are fixed in an optical bench system (Linos GmbH). The light is guided to and from the microscope with optical fibers via vacuum-tight throughputs. A monomode fiber F1 is used in the excitation optical path (green), while, for a better signal collection efficiency, a multimode fiber F2 is used in the collection optical path (red).

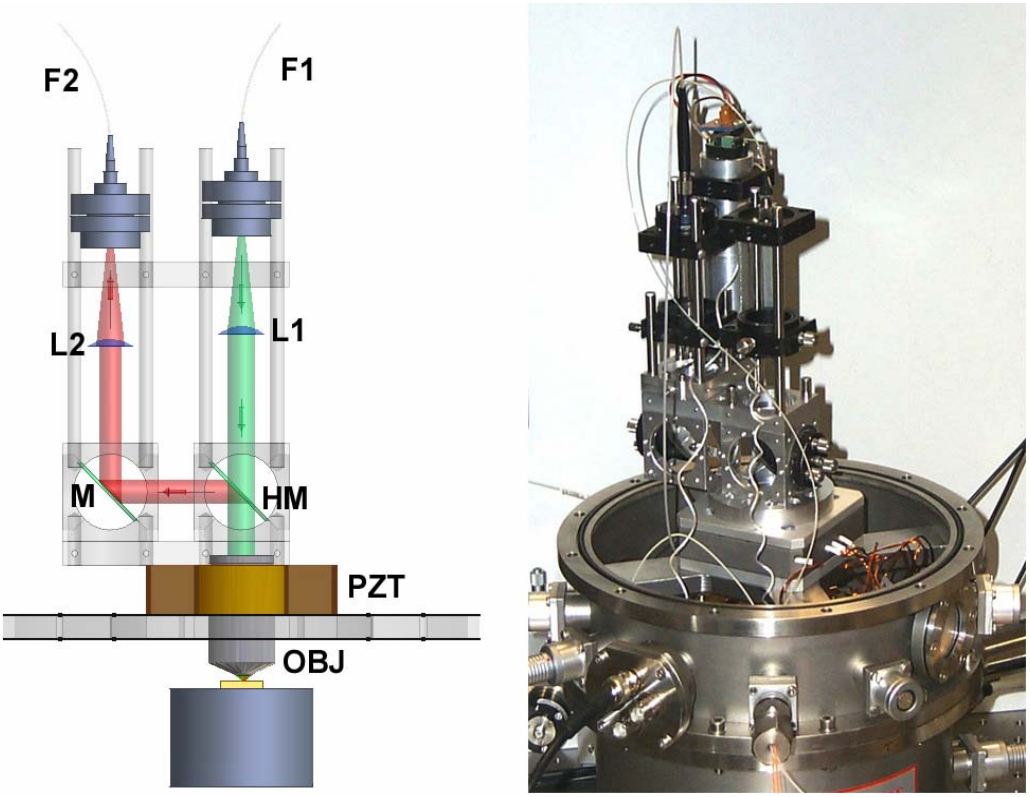

Figure 4.2 Excitation (green) and detection (red) optical paths in the microscope. Image of the realized microscope. The whole microscope unit is fixed on top of a piezo-scan table (PZT).

The light of a He-Ne laser, guided through a monomode fiber, is collimated in the microscope with a f = 60 mm achromatic lens (L1). About 5% of the beam intensity passes trough a 45° tilted "hot mirror" (HM) and is focussed onto the sample. The collected signal is reflected from the hot mirror to the detection optical path (red). The high reflectivity window of the hot mirror is centred at the QD's emission wavelengths (>98% in the wavelength range between 1000 – 1100 nm corresponding to 1,24 – 1,13 eV).
The microscope objective (OBJ) is used to focus the parallel laser beam onto the sample surface and to collect the photoluminescence signal. Apoplan Leica objectives with 50× and 100× magnifications and numerical apertures (NA) of 0,85 and 0,90 have been used for the experiments. The collected μ-PL signal is reflected to the vertical direction by a second 45° tilted mirror (M) and finally focussed with a f = 60 mm lens (L2) to the end of the multimode fiber. Both mirrors are mounted on holders which are adjustable with three micrometric screws, to optimize the coupling to the optical fiber connected with the spectrometer. A thin 45° tilted cover glass is placed behind the second mirror (not shown in the schematic view of fig. 4.2), and reflects a few % of the He-Ne beam, reflected from the sample, to a CCD camera, so that the sample surface as well as the excitation beam focus point are visible on a video monitor.

It is to be noticed that the system is not a true confocal set-up, because of the presence of the multimode fiber in the detection channel, which does not act as a pointlike pinhole like the monomode fiber in the excitation path. This configuration allows a better signal collection yield, but it reduces the optical resolution of the microscope in the experiment on QDs (see next section). The whole microscope unit is mounted on a piezo-scan table (PZT), which is one of the positioning unit in the system (section 4.5).

4.3 Optical characterisation

In the μ-PL experiments discussed in this work, the photoluminescence of the QDs is excited non-resonantly with the light of a He-Ne laser (5 mW output power). As already discussed, the emission occurs in the near infrared region. For this reason a Nd-Yag laser (λ = 1064 nm) has been used for the adjustment of the optical elements in the collection optical path.
The beam of the He-Ne laser is coupled into a monomode fiber with an opto-coupler mounted on three micropositioning stages for fine alignment with respect to the laser beam. A plasma filter is used to remove unwanted laser lines and moveable neutral filters can be placed before the coupling into the fiber to control the laser power. The intensity of the light which reaches the sample has been measured with a power meter placed in front of both objectives used in this work. This calibration is important for the power dependence series of measurements performed on the QDs samples.
An important point has to be addressed: the objective is used both for focussing of the excitation beam (He-Ne, 633 nm) onto the sample and for collecting the PL signal in the near-infrared. Therefore, working with different wavelengths the chromatic aberration has to be considered (fig. 4.3a). To characterise this effect and to estimate the optical resolution of the microscope, measurements were performed with both laser sources and objectives on a test sample for optical microscopy (metal lines of different widths on glass, standard sample GN1).
The resolution (or diameter of the focal spot) has been measured for both objectives with the 10-90% criterion of the intensity jump from the maximum to the minimum of the reflected signal at the edge of a metal line. A photodetector has been used in the visible and an avalanche photodiode in the IR region of the spectrum. Experiments have been performed scanning at a fixed distance a 10×2 μm^2 large area across the metal line. This optical picture has been averaged to obtain an unique profile from which the resolution can be determined. This procedure is then repeated by reducing the distance between sample and objective until the sample reaches the focal plane. Fig. 4.3b shows the result of the experiment performed with the 100× Leica objective.

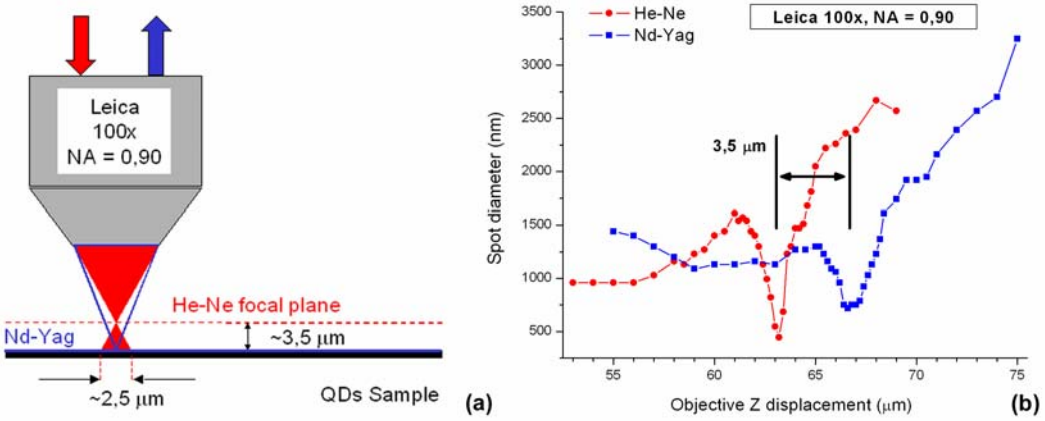

Figure 4.3 (a) Schematic representation of the chromatic aberration effect: the same objective is used for photoluminescence excitation (He-Ne) and signal collection (simulated by the Nd-Yag wavelength). (b) In the case of the 100× Leica objective the focal planes for the two wavelengths lie about 3,5 µm apart from each other.

In the graph the red and blue colours distinguish between He-Ne and Nd-Yag laser sources, both plotted as a function of the objective displacement in z direction. The distance between sample and objective has been changed and measured with the linearized piezo scanner on which the microscope is mounted. The best achieved optical resolution is in the range of the theoretical limit of λ/(2NA), 440 nm (500 nm) for the He-Ne and 720 nm (760 nm) for the Nd-Yag in the case of the 100× (50×) objective. The separation between the two resolution maxima (spot diameter minima) represents the distance between the focal planes due to the chromatic aberration and it is about 5 µm for the 50× and about 3,5 µm for the 100× objective. The results of this set of measurements are reassumed in table 4.1.

	Resolution - spot diameter (nm)		**Distance between He-Ne and Nd-Yag focal planes**
	He-Ne	Nd-Yag	
50×	500	760	~5 µm
100×	440	720	~3,5 µm

Table 4.1 Optical characterisation of the microscope.

In the photoluminescence experiments on QDs the sample is always positioned in the plane, which corresponds to the focal plane for the Nd-Yag wavelength; this is due to optimize the collection of the weak dot emission signal. In this way a large area of approximately 2,5 µm (100×) and 3,5 µm (50×) radius is illuminated by the excitation beam (fig. 4.3a). This area is further increased by diffusion effects arising from carrier diffusion in the GaAs barrier, because of the non-resonant excitation energy used for the experiments performed in this work. Because of this large excitation area and the presence of the multimode fiber in the signal collection path, QD luminescence is collected even if the dot is not in the focal point of the objective (fig. 4.4). Thus the lateral resolution expected in the experiments on QDs is lower than the value measured at the Nd-Yag wavelength. It should be

mentioned, that even placing the sample in the focal point of the excitation laser, thus exciting a very restricted area of the sample, the resolution would be lowered by the diffusion of the carriers.

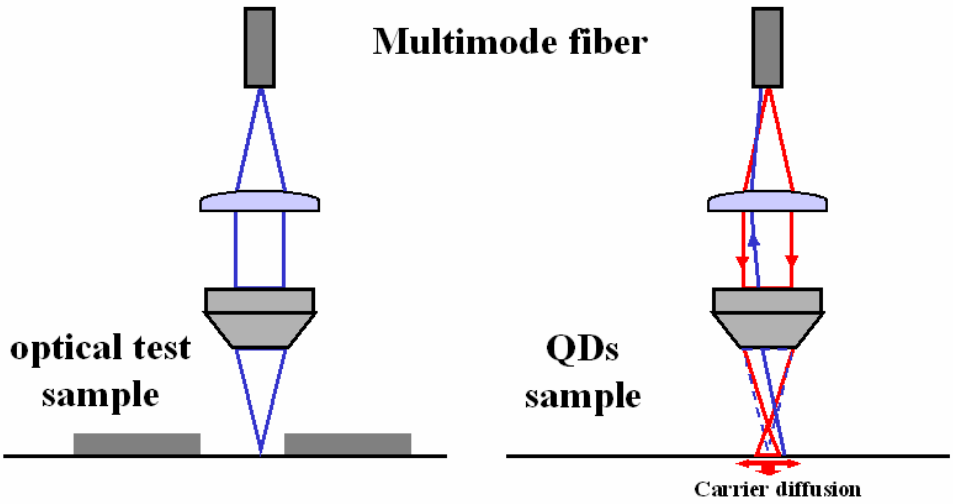

Figure 4.4 Schematic of the collection optical path: the use of a multimode fiber combined with diffusion effects in the semiconductor QDs sample leads to a reduction of the lateral optical resolution.

The use of a monomode fiber instead of the multimode one and resonant excitation conditions would lead to an improvement of the optical resolution in the range of the diffraction limit (and below in combination with the SIL technique). In order to reach a resolution below the diffraction limit, a specially designed sensor head could also be implemented, which was developed in the frame of a high resolution spectroscopy project by the author. This head consists of a combined optical mirror objective with integrated compact SFM and SNOM unit [116].
The efficiency of the collection optical path is about 30% (50×) and 20% (100×) at 1064 nm. These values are the ratios between the output intensity at the end of the multimode fiber and the intensity measured in front of the objective.

4.4 Fourier Transform spectrometer

The collected optical signal is guided to and analysed by a infrared Fourier-Transform spectrometer (FT-IR) of the type Matrix (Bruker Optik GmbH). The instrument sweeps the mirror in one arm of a Michelson interferometer at a constant rate. An interferogram is produced by measuring the intensity at the output of the interferometer as a function of time. For weak signals the interferogram can be built up by repeatedly stepping the mirror and collecting single data points. The frequency spectrum is obtained by calculating the Fourier transform of the recorded interferogram.

The resolution of the spectrometer depends on the maximum mirror displacement and is nominally 1 wave number for the used instrument, which corresponds to about 124 μeV. The signal is detected by a high sensitivity, liquid nitrogen cooled Ge detector (with a hold time of almost 5 days). The spectral range spans from 851 nm (1,4568 eV) to 1695 nm (0,7315 eV), with a NEP < 10^{-15} W/Hz$^{1/2}$ and a maximum frequency of 5 kHz. The spectrometer is connected with the SFM control electronics and a dedicated software allows the synchronisation of the spectra acquisition program with the scanning force microscopy software.

4.5 Positioning systems

Microscope and cold finger (which also acts as sample holder) are mounted on two independent positioning systems, the first one on a closed-loop piezoscanner and the second one on a three axis stepper-motor stage. The 'coarse' positioning of the sample, comprising localization of the area to be investigated and positioning in the focal plane of the objective, is done by the stepper-motor stage (Micos GmbH). The spanned area in the x-y plane is 4,6×4,6 mm^2 and the vertical direction range is 3 mm. The motors can be controlled with a joystick or with the dedicated software, and the coordinates are recorded to a file. The stepper-motor positioning is not reproducible on a submicrometer scale and furthermore it requires the movement of the whole cold finger unit, including the thin pipes for the liquid helium. During cooling of the sample every movement of these pipes causes instabilities of the temperature, and consequently of the sample position. For this reason during the PL measurements the precise focussing, fine positioning and scanning are performed moving the microscope with the piezoscanner (Tritor series, Piezosystems Jena GmbH). The movement range of the scanner is 100×100×100 μm^3, which is reduced to 80×80×80 μm^3 in closed-loop mode. The coordinates can be read on the electronic control unit, with an error of ±100 nm. Scanning of the sample is performed with the help of the SFM software (SIS GmbH), which, in combination with the sensor head [116], allows the use of the system as a low temperature SFM. Despite the weight of the microscope unit, the SFM mode has been proven to work successfully.

4.6 Vacuum and temperature control

The vacuum in the chamber of the cryostat is generated by a turbo pump with a maximal pumping speed of 60 l/min. The pressure reaches 10^{-3} Pa (10^{-5} mbar) after almost one day of pumping without cooling of the sample and falls to 10^{-5} Pa (10^{-7} mbar) during low temperature operation.
The temperature of the sample is defined by the helium-cooled cold finger system Konti-cryostat (Cryovac GmbH). The main advantage of this configuration in comparison to bath cryostats is that only the sample is cooled down, while the rest

of the microscope remains at room temperature [117]. In this way no reduction of the stroke of the piezo scanners occurs and thermal drifts of other components are avoided. The liquid helium flux is controlled by the electronic unit TIC303-MA (Cryovac GmbH) acting on an electro valve. The lowest temperature is 5 K and can be controlled with the precision of better than 5×10^{-2} K. A very high temperature stability can be achieved in this way over long periods of time. The temperature is monitored and recorded to a file every second to control the occurrence of instabilities; an example of the stability during a long system run is given in table 4.2.

Time	Mean (K)	sd (K)	T_{min} (K)	T_{max} (K)	T_{max} - T_{min} (K)
50 min	50,000	0,026	49,96	50,05	0,09
19 h	49,997	0,034	49,96	50,06	0,1
39 h	49,997	0,022	49,94	50,05	0,11

Table 4.2 Temperature stability during long runs of the system at 50K.

Helium is supplied in LHe dewars with a capacity of 100 l, thus the duration of a cooling cycle is limited and depends on the temperature. Experiments at 50 K can be performed for about 6-7 days.

4.7 Mechanical stability

Because of the long integration time expected for the acquisition of a single QD spectrum with the FT spectrometer (1 hour for a single spectrum with the best spectrometer resolution), a very good stability of the whole system is required. The relative position of the objective and of the sample have to remain stable in the micrometer range. This has been achieved by damping or proper fixing of the sources of mechanical noise, like cooling fans and the pipes connected to the vacuum and helium pumps. Furthermore, after cooling and positioning of the sample with the stepper-motors it is necessary to wait until the system thermalises. When the temperature fluctuations stops and the helium flux has been stabilised, the mechanical stability of the sample allows very long μ-PL measurements and it has been proved to be high enough for SFM measurements too.
In fig. 4.5 the position of a single QD during a 6 days long cooling cycle at 50 K is reported (details on the experiments are presented in the next chapter). Measurement where performed on the same dot over this long time, with only small daily adjustments of the objective position. The relative position of sample and objective drifted in the x-y plane over an area of only 1×2 μm^2 during the six days. Correction of the position in the x-y plane requires the acquisition of an optical image of the QD emission, which is a time consuming procedure.

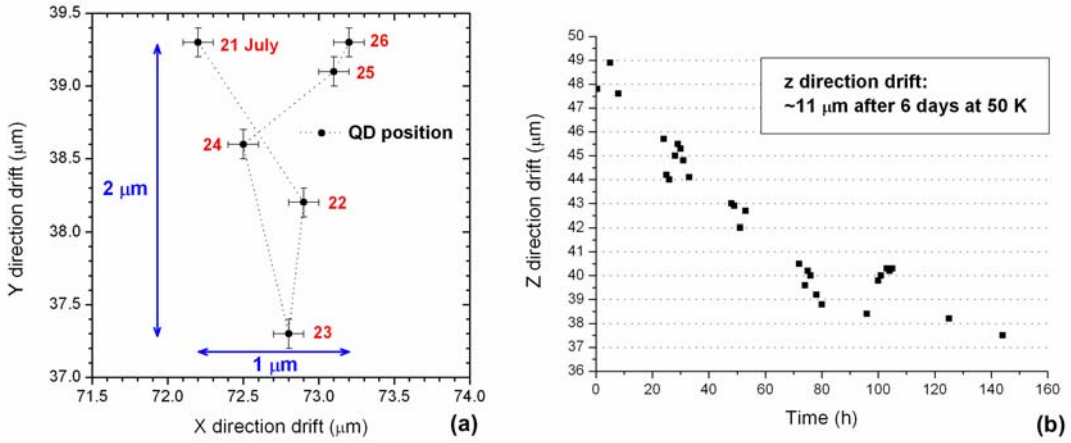

Figure 4.5 Stability of the QD position in the x-y plane (a) and in the z direction (b) over a 6 days long cooling cycle at 50 K.

The drift in the z direction is more pronounced and shows a general downward trend, that means a reduction of the sample-objective distance. Control of the positioning in the z direction is not as critical as for the x-y plane and after each spectrum acquisition the focussing procedure can be repeated. In the case of a very long mapping set of measurements the drift in the z direction causes a decrease of the signal intensity.

5. Micro-photoluminescence experiments

The QDs sample described in chapter 3 has been investigated performing micro-photoluminescence experiments on an ensemble of dots (sample 611-3), while the single QD spectroscopy limit has been reached on sample 611-1. In all experiments described below the QD's photoluminescence is excited non resonantly over the GaAs barrier using a He-Ne laser (E = 1,96 eV) in continuous wave (CW) operation mode.
The sample is fixed in the middle of the cold finger. After cooling the excitation beam is focussed onto the sample and the spot monitored with the CCD camera. Then the objective is moved with the piezo scanner to bring the sample into the focal plane of the Nd-Yag wavelength instead of the He-Ne one. In this way the excitation spot becomes larger but the QD's PL signal in the NIR is collected more efficiently. Like already discussed the chromatic aberration effect depends on the objective used (~3,5 μm for the 100× and ~5 μm for the 50×, table 4.1).

5.1 Micro-photoluminescence measurements on QDs ensembles

Two series of μ-PL spectra have been acquired on a high dot's density region (in the middle of the 611-3 sample) with the 50× objective. The collected signal arises from recombination in an ensemble of QDs, leading to inhomogenous broadening of the PL emission due to the fluctuation in size and composition of the dots.
The first set of measurements was performed at the maximum available excitation power of 105 μW, corresponding to a power density[3] of ~650 W/cm^2, varying the temperature of the sample from 300 K to 10 K. The emission spectra consist of a superposition of broad peaks, which correspond to optically allowed transitions between different shells. Furthermore, at this excitation power the dots are occupied

[3] In the description of the results the incident power is always the value measured in μW in front of the objective.

by multiple excitons, thus carrier-carrier exchange and Coulomb interactions play an important role giving rise to energetically close radiative recombination lines. This effect, combined with the emission of inhomogenously broadened ground and excited levels, leads to the complex spectra structure presented in fig. 5.1. Spectra at this high pump power do not present well separated peaks. The QD's emission lies in the interval between 0,95 eV and 1,25 eV, while the peak at 1,25 eV corresponds to recombination processes in the InGaAs QW (~16 meV FWHM from a Gaussian fit). These measurements show that only a small increase of the PL yield occurs at temperatures below 60 K.

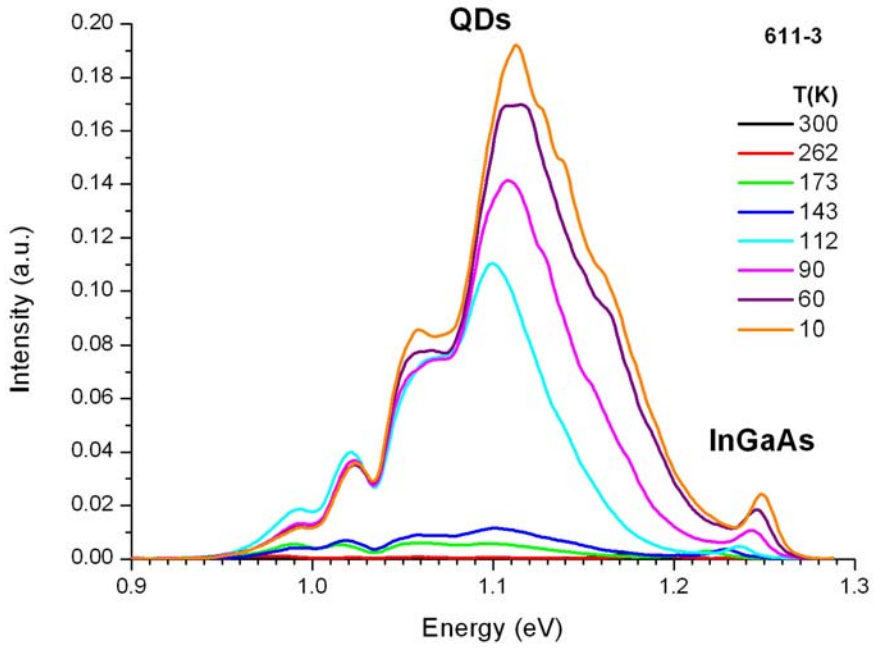

Figure 5.1 Series of spectra acquired at different temperatures (10 K ≤ T ≤ 300 K) at the highest available excitation power of 105 μW (~650 W/cm^2) on a high dot's density region in the middle of sample 611-3.

A second set of measurements was performed varying the temperature from 200 K to 5 K and acquiring at a fixed temperature a series of spectra at different excitation powers. The series of spectra at 20 K is presented in fig. 5.2. At very low excitation power of 0,07 μW (~0,4 W/cm^2) the spectrum shows a single emission peak centred at 1,06 eV and a width of ~50 meV, which arises from ground state recombination processes in the dots. With increasing pump power the spectra are the result of superposition of excited states emissions, leading to a very complex shape and become difficult to interpret. At the two highest pump powers the QD's energy levels are filled and recombination takes place in the InGaAs QW too.

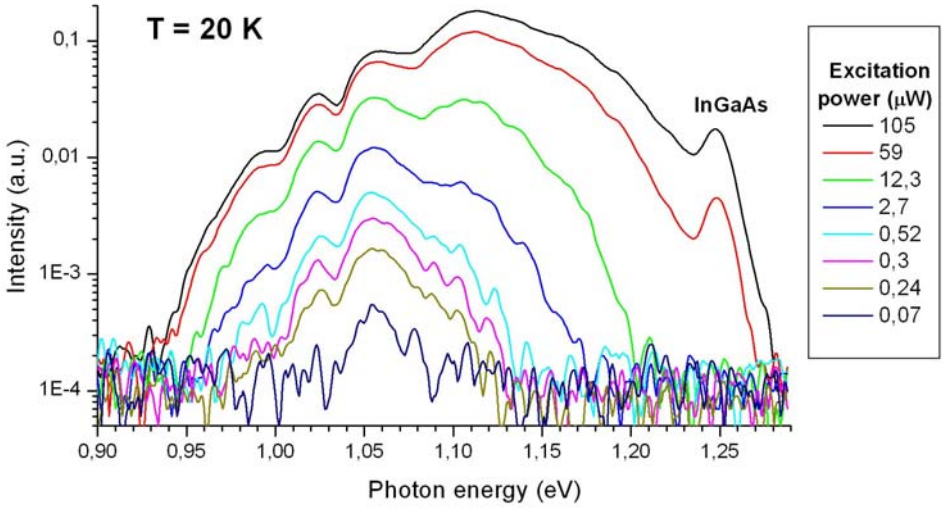

Figure 5.2 Dependence of the QDs photoluminescence with respect to the excitation power (varied over 3 orders of magnitude) at T = 20 K. At the highest pump powers the QD's states are filled and recombination takes place in the InGaAs QW too.

A multipeak fit of these spectra with Gaussian distributions leads to a non univocal result, making it impossible to extract the underlying peak structure. The problem is that the fits are very sensitive to small parameter variations and to the number of peaks chosen.

5.1.1 Temperature dependence

The emission energies of the InGaAs QW peak and of the QD's ground state emission have been plotted as a function of the temperature in fig. 5.3. The peaks, extracted from the two series of measurements described above, have been fitted with a Gaussian function (not presented). Due to the shrinking of the semiconductor bandgap, both emission energies are expected to be redshifted with increasing temperature. In the plot the red lines represent fits to the experimental data performed with eq. (2.24), while the green and blue dashed lines show the temperature dependence of the bulk InAs and GaAs bandgaps. The fitted parameters are listed in table 5.1, together with the values for the bulk InAs and GaAs from ref. [110]. The InGaAs QW emission energy shows an almost flat dependence on the temperature below 70 K and lies between the InAs and GaAs bulk behaviours for T > 200 K. The QD's peak position scatters at low temperatures, while for T > 100 K the two experimental points lie near the GaAs bandgap dependence, which in that temperature range presents a faster redshift than for the bulk InAs. As discussed in section 2.8 the fitting parameters are related to material specific characteristics of the emitting structure.

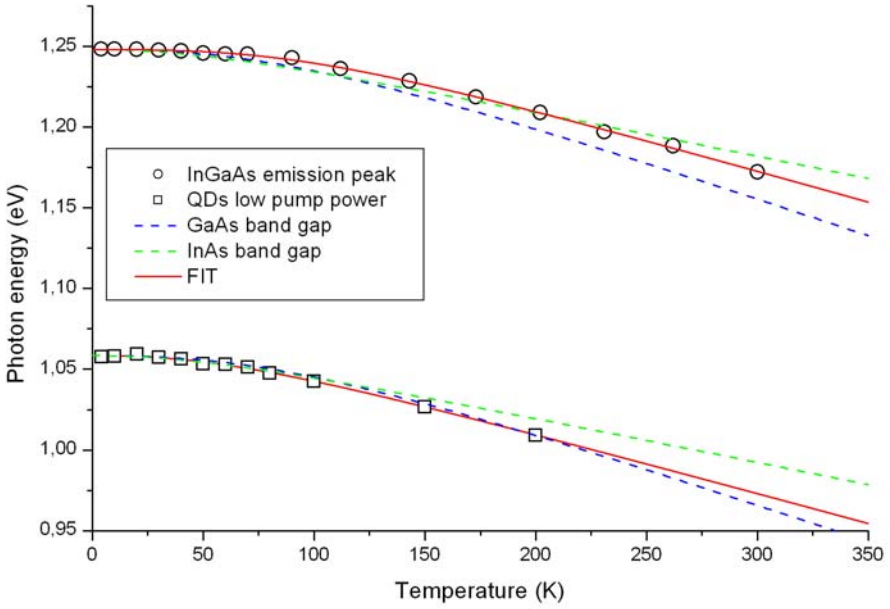

Figure 5.3 Temperature redshift of the ground state QDs emission and of the InGaAs QW peak. The green (blue) dashed lines represent the bulk InAs (GaAs) bandgap temperature dependence. Red lines are fits from the experimental data.

	GaAs	**InAs**	**InAs QDs**	**InGaAs QW**
E_{gap} (eV)	1,519	0,414	1,0584 ± 0,0005	1,2480 ± 0,0004
α (meV)	0,472	0,281	0,38 ± 0,05	0,39 ± 0,02
Θ_p (K)	230	143	157 ± 55	225 ± 24
p	2,44	2,10	2,4 ± 0,5	3,0 ± 0,4

Table 5.1 Fitting parameters for bulk GaAs and InAs [110] and results of the fits for the QD's and QW experimental data.

The parameter α is the slope of the fitting function for $T \to \infty$. As pointed out in [110] only fitting a set of data which covers a temperature range up to $T \geq \Theta_D$ (Debye temperature) leads to a trustworthy value of the limiting slope. The experimental data reach 200 K in the case of the QDs and 300 K for the InGaAs peak, in comparison to Θ_D = 262 K (360 K) for the bulk InAs (GaAs), thus the reported values can not be considered well determined. Nevertheless, the important observation is that the asymptotic behaviour of both curves lies between the bulk GaAs and the InAs ones: because of its composition this effect is expected for the $In_{0,12}Ga_{0,88}As$ QW peak, while it means a faster redshift rate than the InAs bandgap for the QD's emission.

Θ_p is related to the effective phonon temperature, the value 157 K for the QDs ensemble is near to the bulk InAs one, while 225 K for the $In_{0,12}Ga_{0,88}As$ is almost equal to the GaAs bulk value. Thus the relative weights of the contributions of various sections of the phonon energy spectrum to the measured $E(T)$ dependence are similar to that of the respective bulk materials (with the GaAs considered as the

"bulk" for the $In_{0,12}Ga_{0,88}As$ QW). The fourth fitting parameter p gives the curvature of the function at low temperature and with Θ_p enters eq. (2.23), which gives in this model the phonon cut-off energy ε_0. To be noticed is the similar value for p_{GaAs} and p_{QDs}, an effect which is further discussed in section 5.2.4, where the dependence on the temperature of the single QD emission has been investigated.
The listed values present quite large errors, but the aim of this analysis is not the exact determination of the material parameters, but a better understanding of the sample characteristics by comparison with the bulk values. The bandgap temperature dependence is determined by two mechanisms involving phonons, the thermal expansion of the crystal and the electron-phonon interactions. The InAs QDs are embedded between the two 5 nm thick $In_{0,12}Ga_{0,88}As$ layers, surrounded by the GaAs barrier. Both QD and QW structures are strained and the strain field influences the phonon energies and the phonon mediated processes. The dependence on the temperature of the QD ensemble emission is even more complicated, because of the complex carriers dynamic between dots. As already pointed out, the temperature dependence of the QD's ground state emission at high temperatures presents a faster rate of energy shift than the InAs bandgap. Fig. 5.4 shows the difference between the experimental data and the expected change in the InAs bandgap, represented by the dotted horizontal line at 0 eV. At temperatures above 80 K the experimental points lie below the InAs bandgap temperature dependence.

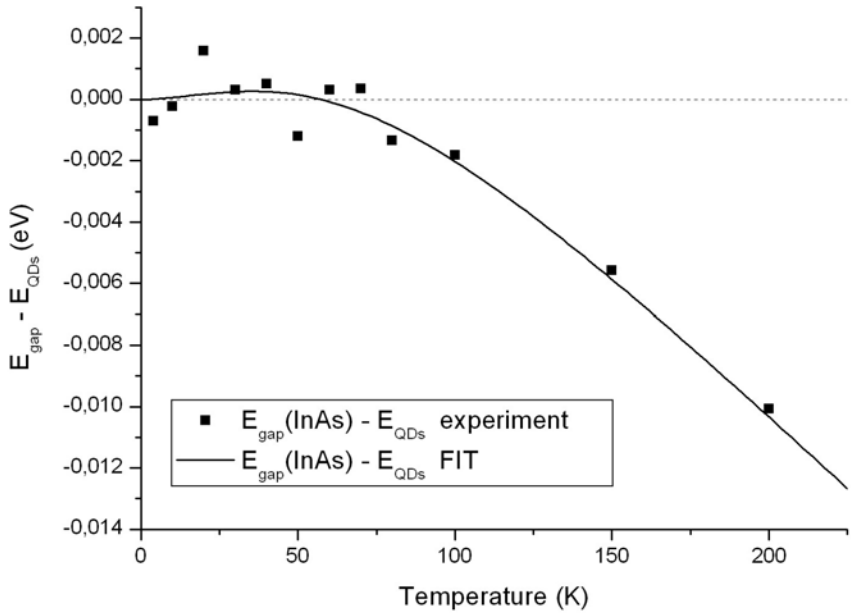

Figure 5.4 Difference between the InAs bandgap dependence on temperature (dotted line) and the experimental data. The full line is the difference between the fit of the data (red line in fig 5.3) and the InAs bangap.

This result is in agreement with experiments on InAs QDs ensembles reported in refs. [118][119][120]. The effect is explained by the enhancement of coupling and relaxation effects between dots, due to the increase of the electron-phonon

interaction with temperature. In this way the carriers can transfer to larger dots and relax into lower energetic states, giving rise to the observed fast redshift of the exciton ground state energy. The magnitude of the observed effect is comparable with that reported in [120] for small InAs/GaAs QDs (r ~ 12 nm) emitting at 1,105 eV.

5.2 Spectroscopy on single QDs

The main topic of this work is the characterisation of the PL emission from single QDs. Low density areas, in which the average distance between neighbour QDs is larger than the spatial resolution of the μ-PL set-up, can be found on the 611-1 sample. The advantage of this approach is that no modification of the sample surface is required, which can influence the dot's emission by strain induced effects in the case of a metal mask or by the influence of trapped charges at the edges of an etched mesa structure [20]. The drawback is that measurements on a particular point are possible only during one cooling cycle (4-6 days depending on the temperature), because thermal drifts, during the warming and the successive cooling processes, cause the lost of the previous measurement point. The mapping option (see next section) allows in principle to obtain an optical picture of the sample within the drift range, but the long integration time needed to scan large areas makes this option not realisable in spectroscopy mode. A different QD for investigation is then chosen at every cooling cycle. μ-PL measurements were performed at temperatures below 60 K in a region ~6 mm away from the high indium concentration edge on the 611-1 sample, where the QDs emission energy lies between 1,1 eV and 1,2 eV.

5.2.1 Mapping

The experimental set-up with the combination of the piezoactuator driven stage and the synchronisation of SFM and spectrometer software allows scans of sample areas and the acquisition of one spectrum for each point of the scan grid. This mapping procedure results in a 3D set of data (x, y, I(E)) containing the coordinates (x, y) and the spectrum I(E). The extraction of the intensity I from each spectrum at a given energy E or the sum of the intensities over an energy range ΔE gives optical images of the sample emission at that energy E or over the interval ΔE (fig. 5.5). Because of the low intensity of the emission from a single QD a long integration time (normally 1 hour) is required for the acquisition of a single spectrum at the highest available resolution (about 124 μeV) and with a good signal to noise ratio.

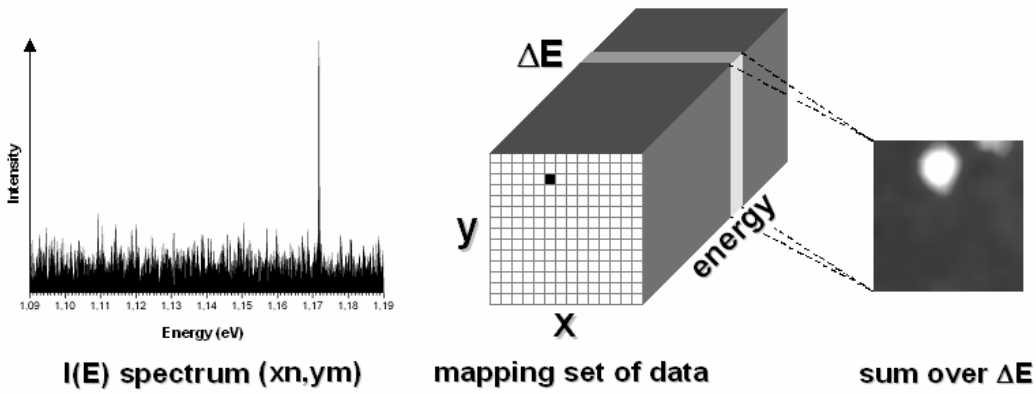

Figure 5.5 The acquisition of one spectrum I(E) for each point (x, y) of a raster (mapping), leads to a 3D set of data (x, y, I(E)). Sections at a given energy E (or sum over an energy range ΔE) give optical images of the emission at that E (ΔE).

For mapping measurements a trade off has to be found between the size of the scan area and both the spatial and the spectral resolution, in order to restrict the acquisition time to a reasonable limit. Because of the low optical resolution expected for experiments on the QDs (see section 4.3), the spectra have been acquired at a distance in the range between 0,5 – 1 μm. Furthermore, the resolution of the spectrometer has been reduced depending on the size of the scan area to limit the acquisition time to a maximum of one day. A typical result of a mapping series performed at 50 K with the 100× objective is presented in fig. 5.6a.

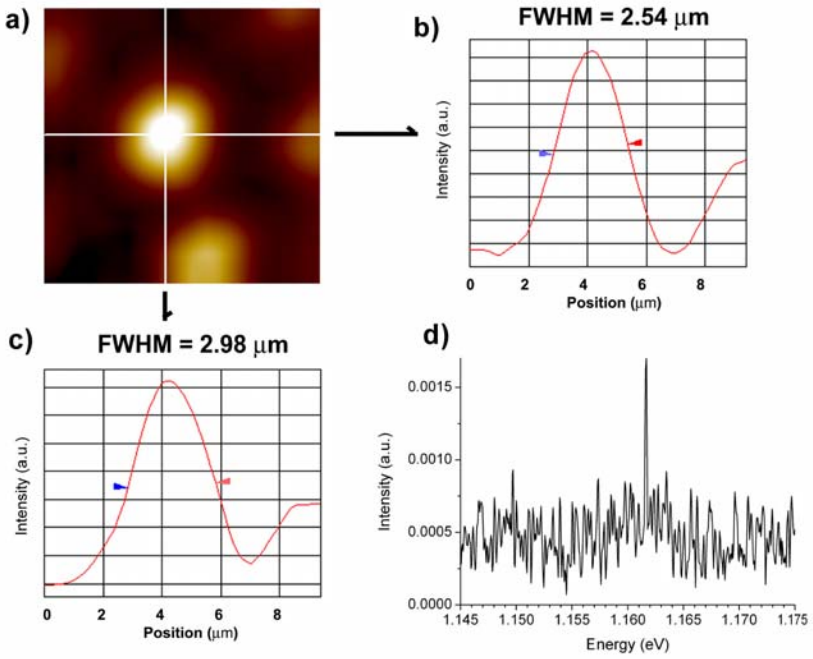

Figure 5.6 Image of the QD emission acquired with the 100× objective. The scan area is 9,4×9,4 μm^2 wide, covered by a grid with 20×20 points and the acquisition time is almost 20 h. The resolution in the slower scan direction (vertical) is influenced by drifts during the long measurement.

The 9,4×9,4 μm^2 scan area was mapped with 400 spectra (20×20 points grid), the spectrometer resolution lowered to 15 wave numbers (~2 meV) and each spectrum integrated for about 3 min, resulting in a total acquisition time of almost 20 h. The image has been obtained using a detection energy centred at 1,161 eV and with a width of ΔE = 2 meV. A high resolution spectrum acquired in the center of the bright spot, at the same excitation power used for the mapping series, is presented in fig 5.6d, showing a very narrow (140 μeV limited by the spectrometer resolution) isolated emission line. From the optical images it is possible to estimate the lateral resolution of the system, for this kind of experiments. The FWHM of the bright spot due to emission of a single QD is 2,5 μm in the horizontal and 3 μm in the vertical direction. The asymmetry is due mechanical drifts of the system, which affect the slower scan direction (vertical) stronger than the faster one (horizontal). The mapping series presented in fig. 5.7 was recorded at a temperature of 50 K. In the 7×7 μm^2 area of the image the emission of 6 different QDs has been clearly identified, with ground state emission energies ranging between 1,14 eV and 1,9 eV.

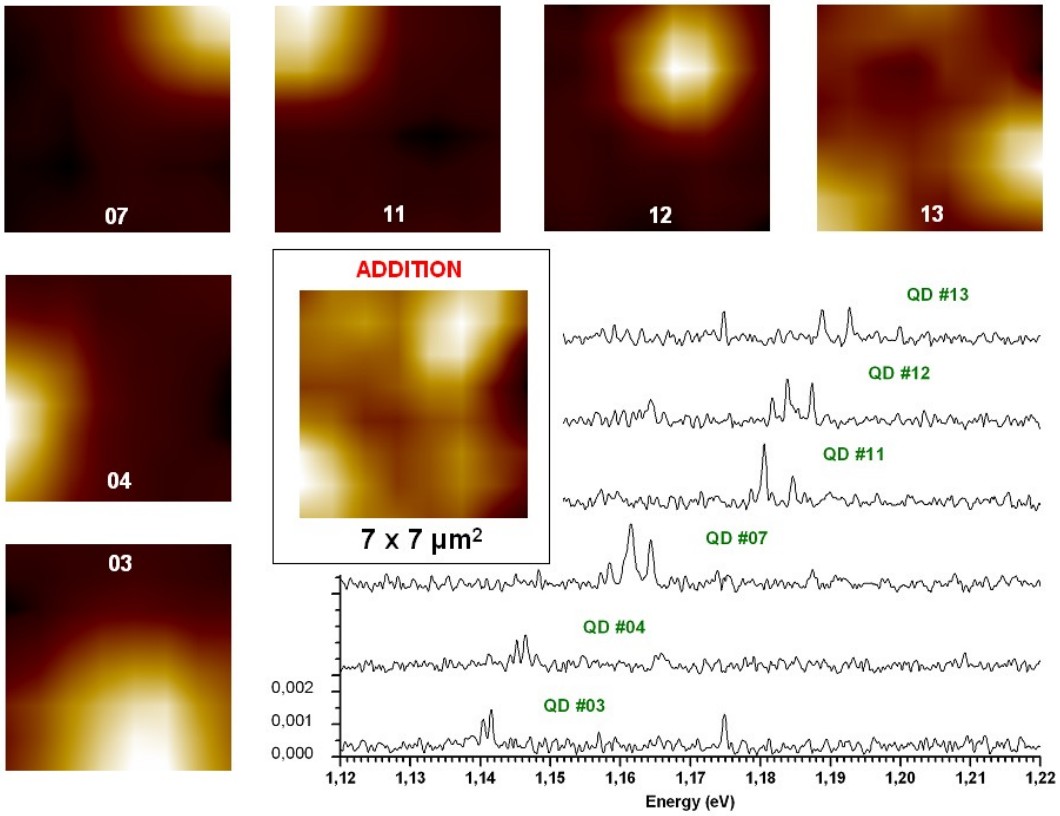

Figure 5.7 Images extracted from a mapping series of spectra showing the emission of six different QDs in a 7×7 μm^2 large area. The image in the middle is the superposition of all images normalized to the maximum emission intensity.

The diameter of the spots is slightly bigger than in the previous image (~3 μm), because in this case the measurement was performed with a 50× Leica objective. Each spectrum contains a doublet of lines corresponding to the exciton and

biexciton emissions, the latter is always at the lower energy side of the E_x line. The additional lines present in some of the spectra near the exciton and biexciton emissions are tentatively attributed to the emission of charged exciton complexes (see sext section). The resolution of the spectrometer was set to 3 wave numbers (~400 μeV) and the integration time to 18 min for each spectrum, leading to a total acquisition time of almost 19 h for the 64 points of the grid. The images from the bottom left to the top right corner corresponds to the spectra from the bottom to the top. Each image is centred at the energy of the exciton emission line and the one in the middle is a superposition of all the images normalized to the maximum emission intensity. The dots density observed in this area of sample 611-1 is about 10^7 cm^{-2}. Emission from different QDs can be spatially or energetically resolved if their separation is bigger than the optical resolution, or, in the limit of low pump power, if their energy separation is larger than the spectral resolution used for the acquisition of the spectra.

5.2.2 Emission from a single QD

The mapping of the sample allows to find an isolated single QD and is used to adjust the objective over the particular dot under investigation (after normally one day of measurements) or in the case of mechanical drifts which cause the loss of alignment. To verify that the luminescence arises from recombination processes in a single QD a series of spectra is acquired at increasing excitation pump power. At very low power only one emission line is expected, arising from the recombination of an electron-hole pair at a time and characterised by a very narrow linewidth, below or in the range of the resolution of the spectrometer.
In the following the shell notation commonly adopted for atomic spectroscopy has been used, thus s-shell indicates the ground state and p-, d-shell the excited levels. Fig. 5.8 shows the emission of a single QD recorded at 30 K and at very low excitation power: the spectrum in the lower part of the picture presents, as expected, just one narrow line arising from the recombination in the QD of only one exciton at a time (E_x line). The increase of the excitation power from 0,3 μW to 0,52 μW causes the appearance of other lines in the lower energy side of the first one: the strongest appearing 4,1 meV below the E_x is attributed with a power dependent study (not presented) to the biexciton decay (E_{xx} line). The attribution of the emission lines in the spectrum is not a simple task: the E_x and E_{xx} emissions show a characteristic behaviour, namely a linear and bilinear dependence at low excitation power and the same is valid for emission from charged exciton and biexciton complexes [49][146]. The dependence on the excitation power has been used in this work to identify the biexciton emission. The distance between the E_x and E_{xx} emission lines is the energy gain between the configuration of two isolated excitons and the biexciton complex, thus the biexciton binding energy (indicated in the rest of this work as ΔE_{xx}).

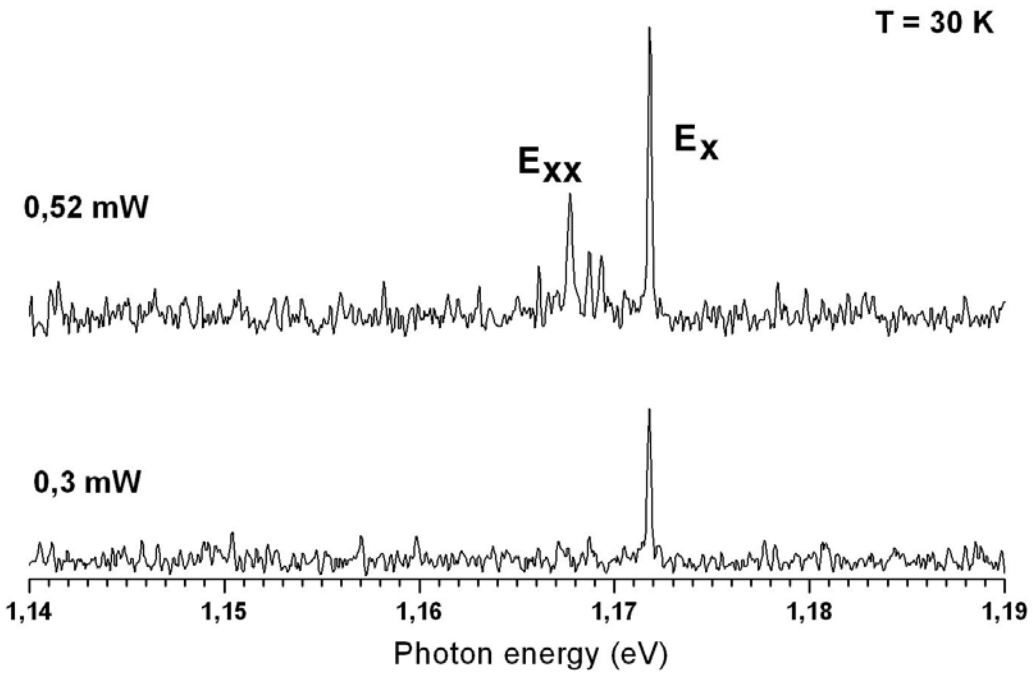

Figure 5.8 Emission from a single isolated QD: recombination of a single exciton E_x (bottom) and of exciton and biexciton E_{xx} (top). The lines between E_x and E_{xx} are attributed to the emission of charged excitons.

Because of their energy (see section 2.4) the weaker lines are tentatively attributed to the recombination of charged excitons, e.g exciton complexes with one (trions) or more excess negative or positive carriers. Charged exciton and biexciton complexes can occur in the case of a resident electron in the dot or in the case of capture of single carriers. The QDs may collect carriers generated in the GaAs barrier from a rather large area in comparison to the dot lateral size (typically a few micrometers [121]). The process of carrier diffusion depends not only on the carrier type (e or h), i.e. on the effective mass of the diffusing particles, but is essentially governed by the excess energy of the created carriers relative to the band gap of the excited material. The significant increase (up to five times) of the effective diffusion constant of photogenerated carriers in GaAs QWs with increasing pump-photon energy was experimentally demonstrated in ref. [121]. Thus it is reasonable to expect that the significantly different diffusivities of electrons and holes will lead to a population of QDs with different numbers of e and h. This effect will be manifested by the appearance of lines due to charged exciton or biexciton complexes in the time-averaged emission spectra of individual QDs.
The position of the charged exciton lines with respect to E_x depends on the localization of the carriers in the QD and on the sign of the excess charge. In the case of stronger confinement for holes in comparison to electrons, negatively charged E_x lines are always red-shifted, while positively charged E_x can be either red- or blue-shifted, depending on the relative strength of the positive Coulomb interaction in comparison to the negative contributions of exchange and correlation [66]. The magnitude of this shift is of the order of a few meV, comparable with the

biexciton binding energy. The presence of additional lines in the s-shell like the ones in fig. 5.8 have been observed for several of the dots studied in the present work. Further investigations are required for a more precise attribution of the observed lines. Power dependence studies and magneto μ-PL experiments allow to distinguish between emissions from charged exciton or biexciton complexes [67][104], while exciting the QDs PL with different wavelengths gives insights into the dependence of the spectra from the carriers excess energy [122].
The emission lines are well fitted by a Lorentzian function (fig. 5.9) and the linewidth of the E_x emission is 190 ± 10 μeV at both excitation powers. In general, if not otherwise specified, all the linewidths given in this work are the result of a Lorentzian fit of the emission lines.

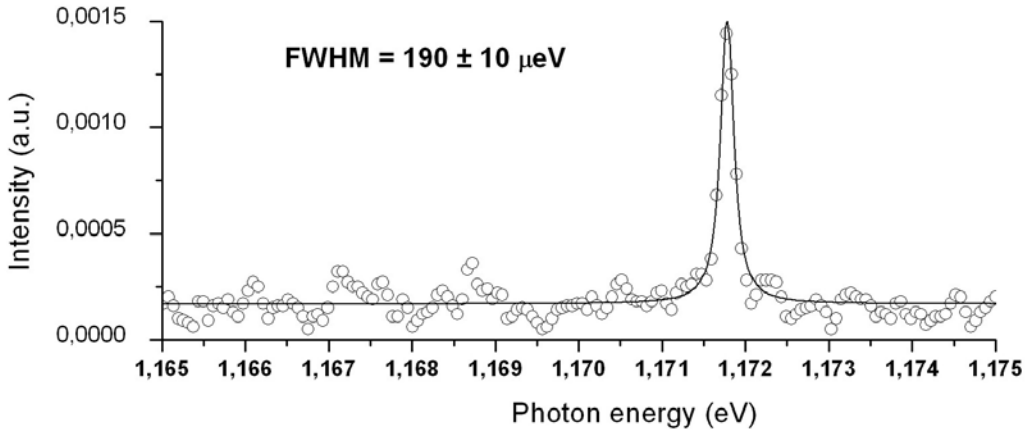

Figure 5.9 Lorentzian shape of the ground state emission E_x from a single QD.

The best spectrometer resolution (~124 μeV) and a very long integration time (5h) were necessary for these measurements. This allows a very good signal to noise ratio and a relatively small error in the determination of the linewidth. Nevertheless, long series were performed with shorter integration times and even reducing the resolution of the spectrometer to further speed up the acquisition, depending on the aim of the measurement. This implies that in some cases not all the lines in the spectra can be properly resolved. With a short integration time the lines between the E_x and E_{xx} lines in the spectrum of fig. 5.8 will have an intensity comparable with the noise peaks.
Dealing here with very long integration times an important property is the spectral stability of the QD emission, which shows often a spectral drift in time (section 2.7.3). The two spectra in fig. 5.8 have been acquired after 1 day time interval and the lorentzian fits for both excitons lines give 1,171780 ± 4 × 10^{-6} eV and 1,171790 ± 3 × 10^{-6}, thus a difference 10 ± 7 μeV which is in the range of the experimental error. Furthermore, long temporal stability of the emission has been proven in the series of measurements presented in the following.

5.2.3 Power dependence of the PL spectrum of a single QD

Fingerprint of the emission from a single QD is the quantization of the energy levels, thus the presence of excited states emission lines in the spectra and their grouping into shells. Increasing the excitation power causes the statistical occupancy with more than one exciton and the subsequent filling of the "atomic like" shell energy structure of the QD. Fig. 5.10 shows a power dependent experiment on a single QD, which is typical for the series of spectra acquired in the present work.
As expected, an isolated single line (labelled E_x in the following) appears at low excitation power due to recombination of a single exciton in the QD. For this experiment the resolution of the spectrometer was set to 2 wave numbers (~250 μeV) to speed up the collection of the spectra. The integration time was set to 50 min and 14 spectra have been acquired at different excitation powers.

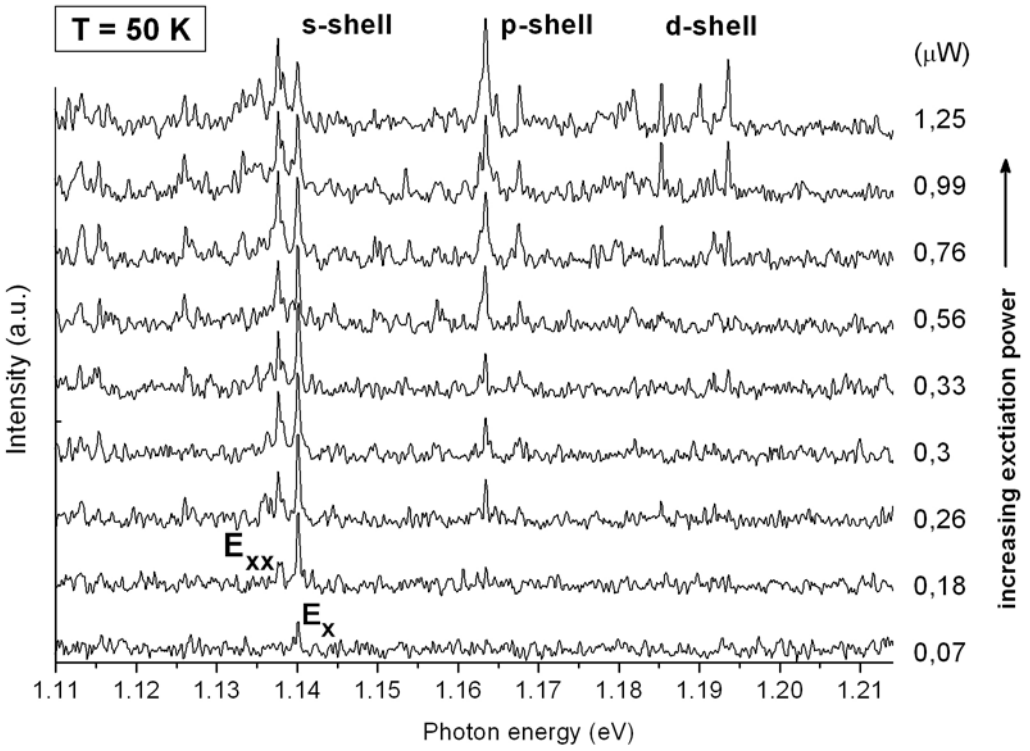

Figure 5.10 Power dependence of the emission from a single QD, with the successive appearance in the spectra of the ground state E_x and the biexciton E_{xx} lines and at higher pump powers the emission from excited states (p- and d-shells).

At the lowest pump power only the ground state emission line (E_x) is present in the spectrum. As excitation power increases a second line (E_{xx}) appears on the low energy side of the E_x line, which originates from recombination of a second exciton in the QD. The two excitons in the dot form a biexciton complex, the E_{xx} line arises from a sequential biexciton decay, i.e. the radiative recombination of a bound biexciton configuration into a single exciton state in the s-shell. The lower emission

energy indicates a positive biexciton binding energy (ΔE_{xx}) whose magnitude is the distance between the E_x and the E_{xx} lines (in this case 2,4 meV).
The power dependence of the intensity of the two lines confirms the interpretation as single exciton and biexciton emissions. In the double-logarithmic plot (fig. 5.11a) the integrated intensity of the E_x line exhibits a linear increase with the excitation intensity, whereas the biexciton line intensity shows a superlinear increase with an exponent of 2,1. In the case of resonant excitation, a quadratic dependence of the integrated intensity of the biexciton line at low excitation powers is the fingerprint of the two photon absorption process needed for the creation of the two excitons. For non-resonant excitation conditions this behaviour has been modelled with a rate equation system based on a four level exciton-biexciton model [30][123][124]. The basic idea is to relate both exciton and biexciton states by steady-state transition rates. The model predicts a linear and bilinear increase of the E_x and E_{xx} integrated intensities at low excitation powers and a saturation with increasing pump power. Another approach consists in the random capture model [25][125], based on the assumption that the generation of biexcitons is a result of random capture of two excitons at the same time by the dot. Both models show an overall good agreement with the experimental data.

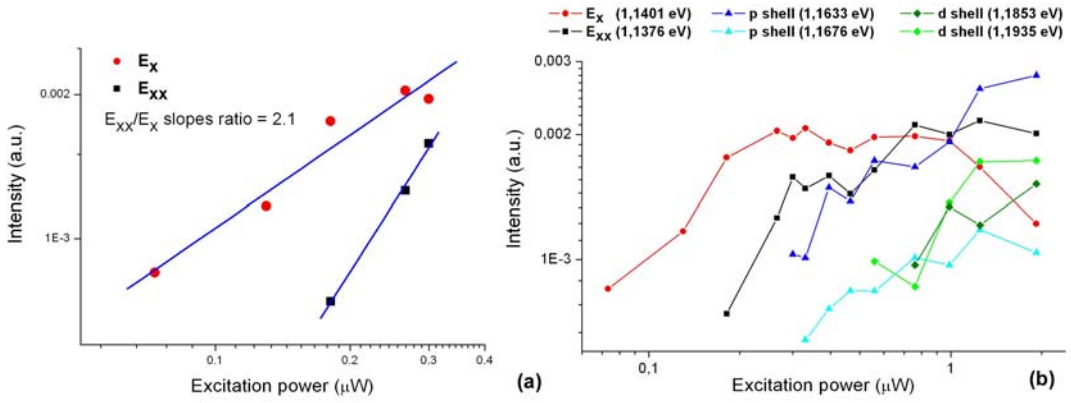

Figure 5.11 (a) Power dependence on a double-logarithmic scale of the intensity of the exciton and biexciton emission lines at low excitation powers and (b) power dependence of E_x, E_{xx} and the two main emission in the p- and d-shells. Note the saturation of the E_x and E_{xx} lines and the linear increase of the excited states emission intensities.

Another tool for the identification of the biexciton emission peak has been recently proposed by means of photon-correlation measurements, by demonstrating its strong correlation with the single exciton emission [126][127]. In ref. [49] both laser power dependent and time resolved PL measurements have been used to identify the exciton, biexciton and their charged complexes emission lines from an individual QD.
The occupancy with two excitons fills the ground state s-shell of the dot, but at higher excitation powers the QD becomes populated with statistically more that two excitons at a time. Because of the Pauli exclusion principle these excitons have to occupy higher energy shells (p, d) and other lines appear on the high energy side of the E_x one. The peaks observed at 1,633 eV and 1,676 eV are associated to

recombination of the three-exciton up to six-exciton complexes, when the first excited energy level (p-shell) becomes saturated. For this QD the centre of the p-shell group lies ~23 meV above the s-shell, while the d-shell emission lines are spread in an interval from about 20 to 30 meV above the p-shell. The integrated intensity of the excited states emission lines shows with good approximation a linear increase, while the E_x and the E_{xx} lines saturate (fig. 5.11b). Additional lines appearing in the s-shell region on the low-energy side of E_x arise from recombination of an s-shell exciton, perturbed by the presence of excitons occupying higher lying shells [68][128]. At the highest pump power a broadening of the s-shell emission is observed which may be caused by Coulomb interaction between carriers in the dot and in the wetting layer [129] and in the surrounding barrier.

5.2.4 Temperature dependence of the single QD emission

As a result of the multiexciton occupancy, the power dependence studies reveal information about the confinement potential and the strength of carrier-carrier interactions in the QDs. They allow the determination of characteristic emission properties like the biexciton binding energy and the distance between the levels in the energetic shell structure of the dots.
On the other side the study of the temperature dependence of the emission reflects the dot crystalline structure and the interactions with the surrounding matrix mediated by phonons. In what follows the emission dependence on the temperature of a single QD has been investigated in the limit of only ground state occupation. The studied QD exhibits exciton (E_x) emission at 1,15679 eV at 5 K (fig. 5.12a).

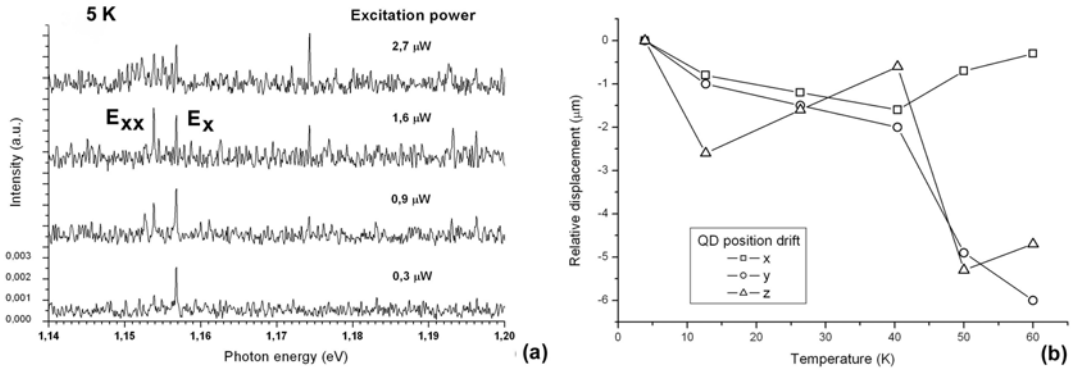

Figure 5.12 (a) Power dependence of the emission. (b) Drift of the dot position during the long measurement run, with respect to the position at the lowest temperature (5 K).

At higher pump power the biexciton (E_{xx}) line appears 2,9 meV below E_x, while the first p-shell emission line lies 17,5 meV above and because of the short integration time of the measurement only weak d-shell emission can be seen at 1,6 μW excitation power ~19 meV above the p-shell. The series of measurements started at 5 K. Since thermal drifts are not avoidable and no marking of the sample is possible

in our set-up (for example with a high intensity laser pulses like in ref. [122]), after every temperature jump it is necessary to find the particular QD under study again. This is normally accomplished by scanning a small 3×3 μm^2 area after the temperature and the cold finger have been stabilised. The displacements of the QD position after every temperature jump are reported in fig. 5.12b, with respect to the position at 5 K. The drift of the system is caused by thermal effects and eventually by mechanical instabilities of the set-up. A jump greater than 3 μm in the y and z directions can be seen between 40 K and 50 K, caused probably by an instability of the helium flux during the temperature change. The series of acquired spectra is presented in fig. 5.13.

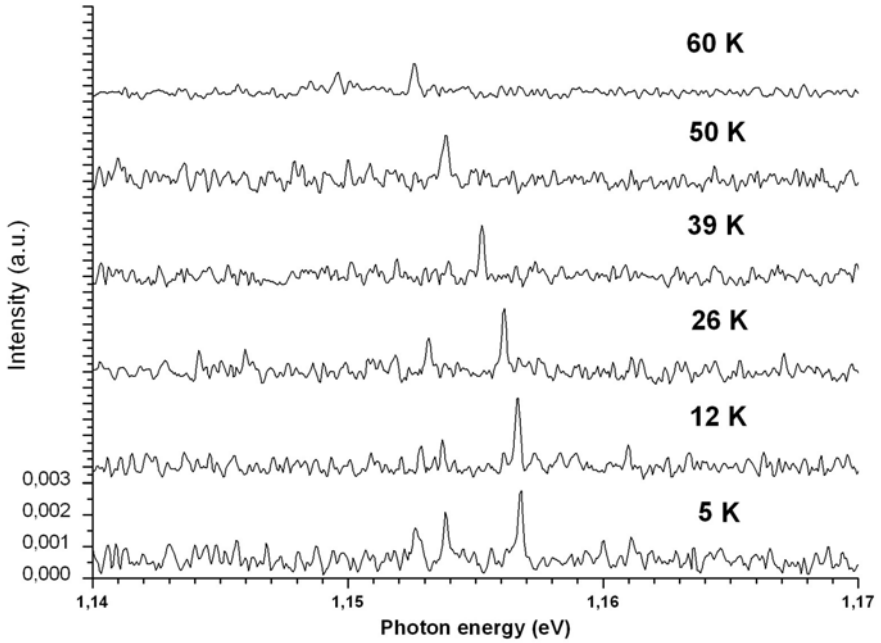

Figure 5.13 Dependence on the temperature of the ground state emission of a single QD. Acquisition time for the spectrum at 60 K is 4 times longer then the others (the noise is reduced by a factor 2).

Each spectrum required 50 min integration time, except the one at 60 K for which a very long time (3h20m) was necessary to obtain a sufficient signal to noise ratio. The noise is reduced by a factor proportional to the square root of the integration time (2 in this case). Unfortunately the QD under investigation has been lost at 70 K, probably because of the very low emission intensity.
The series of spectra clearly shows the drop of the intensity, the energy shift and the broadening of the ground state emission while increasing the temperature. Biexciton emission is present in spectra acquired at the lowest temperatures and at 60 K. Each line has been fitted with a lorentzian function, which gives values for the emission energy and linewidth. The intrinsic crystalline nature of the QD system plays an important role on the optical properties like emission energy and linewidth. The influence of the dot environment is due to lattice vibrations and it is described in terms of coupling with phonons. The effect of the semiconductor bandgap shrinkage with increasing temperature has been already presented in

section 5.1.1, for the QDs ensemble ground state emission and the InGaAs QW peak. The redshift of the exciton emission line from a single dot is shown in fig. 5.14, where the green and blue dashed lines represent the bandgap temperature dependence of the bulk InAs and GaAs materials.

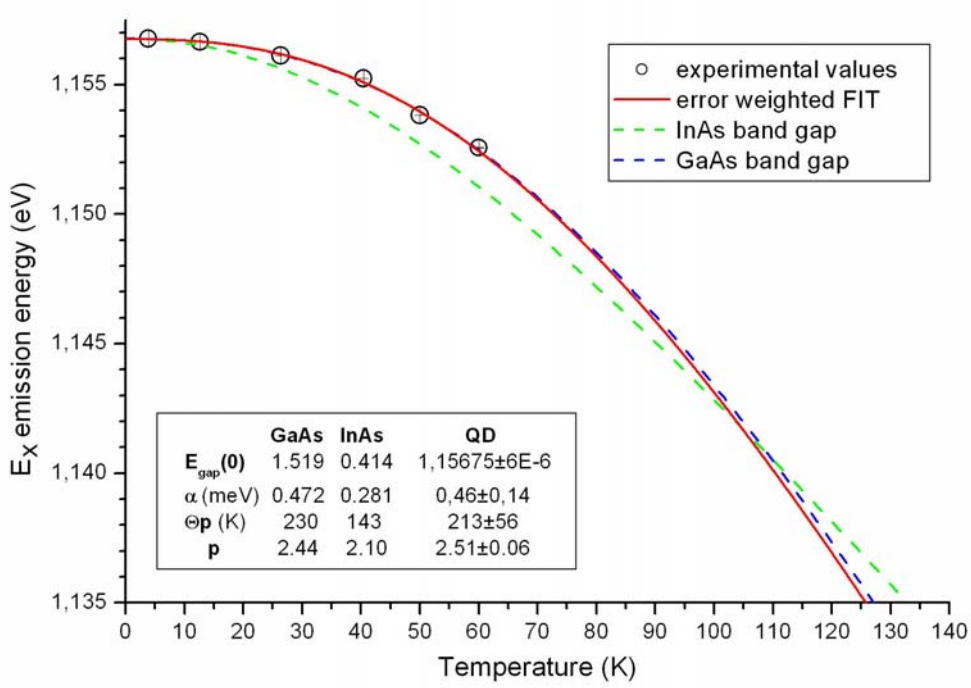

Figure 5.14 Dependence on the temperature of the ground state emission energy E_x of a single QD, with the fit of the experimental data (red) and the bandgap dependence of the bulk InAs (green) and GaAs (blue).

The temperature dependence of the ground state emission for the QDs ensemble has been studied up to a temperature of 200 K (fig. 5.3, section 5.1.1), while data for the single dot emission cover only a range up to 60 K. Nevertheless, at least in this temperature range, the experimental points lie above the InAs bandgap behaviour and follow with very good approximation the GaAs temperature dependence. Since in a single dot experiment interdot relaxation does not play a role, the emission should follow the band gap of either InAs or GaAs. The error weighted fit of the single dot data shows an overall very good agreement with the GaAs bandgap, but the temperature range covered by the experimental points is too limited to draw general conclusions about the temperature dependence. On the other hand, at low temperatures this result agrees with the analysis of the ensemble data. The parameter p, which gives the shape of the fitting function at low temperature, has been found ($p_{QDs} = 2{,}4 \pm 0{,}5$ table 5.1) to be comparable to $p_{GaAs} = 2{,}44$. The large uncertainty determines that even the value of the InAs ($p_{InAs} = 2{,}1$) lies within the error, but the here presented behaviour (confirmed by the emission of a second studied dot) sustains the agreement with the GaAs bandgap dependence.
At low temperatures only low energy longitudinal acoustic (LA) phonons contribute to the temperature dependence. Due to the small QD size these low

energy – long wavelength phonon modes can only propagate in the $In_{0,12}Ga_{0,88}As$ and GaAs barriers surrounding the QD. Their spectrum is the one characteristic of the bulk GaAs and this fact explains the observed agreement of the experimental points for the single QD emission with the GaAs redshift temperature dependence. It would be interesting to follow this behaviour at higher temperatures, because for T > 110 K the GaAs bandgap dependence lies below the InAs one and this effect may contribute to the faster redshift of the QD emission in comparison to the bulk InAs.

5.2.5 Linewidth temperature dependence

Interactions with phonons not only determine the temperature dependence of the bandgap, but also the temperature dependence of the exciton homogeneous linewidth Γ(T), or correspondingly the lifetime of the exciton complexes. The QD emission was thought to be very insensitive to inelastic scattering by low energy acoustic phonons because of the discrete nature of the energy levels. However many experimental results show the persistence of an observable dephasing, characterised by a linear dependence at low temperature due to interaction with low energy acoustic phonons and an abrupt increase at higher temperatures due to scattering by optical phonons. The measured dependence of the E_x (E_{xx}) linewidth on temperature is presented in fig. 5.15a (b). A few preliminary comments are necessary. The series of measurements presented above in fig. 5.13 shows spectra acquired only up to T = 60 K, while in the following analysis a linewidth value at 70 K has been added.

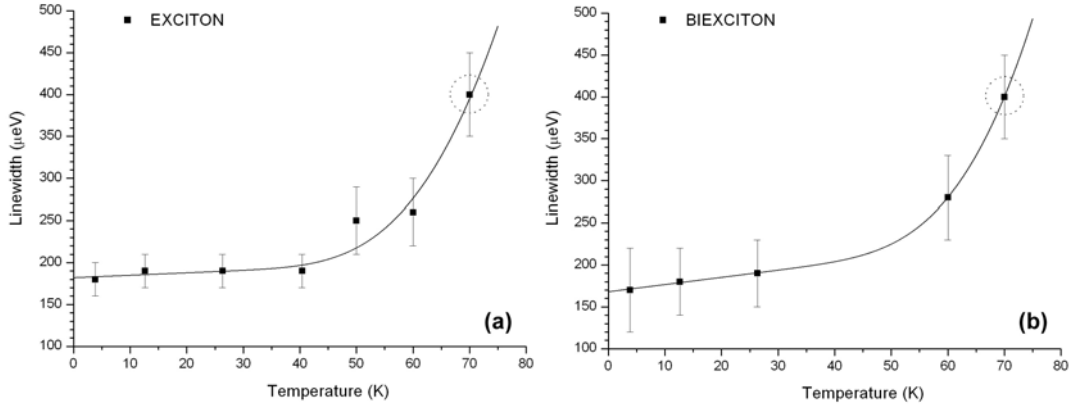

Figure 5.15 Dependence on the temperature of the linewidth of the exciton E_x (a) and biexciton E_{xx} (b) emission lines. The value at 70 K refers to a different QD and it is the lower limit of the linewidths measured at that temperature.

The spectra acquired at this temperature do not show a peak compatible with the studied dot. Most probably in the jump between 60 K and 70 K the positioning was lost and it was not possible to find the studied QD again. The presented linewidth is the lower limit of the linewidths of lines which have been measured at low

excitation power at 70 K, but arising from different QDs. The same value has been taken for both the E_x and E_{xx} linewidths and it is marked with a dotted circle in the graphs. Linewidths with relative errors are the result of Lorentzian fits of the emission lines and have not been corrected considering the limited resolution of the spectrometer.
A weak dependence of the linewidth on the temperature is expected for the emission from a single QD, because of the efficient suppression of the interactions with phonons due to the lack of final states for phonon-exciton scattering processes. Below 40 K the E_x linewidth shows almost no increase, the fit with eq. (2.16) gives a linear coefficient A = 0,29 μeV/K. In the same temperature range the E_{xx} line shows a more pronounced linear increase of the linewidth of about 0,86 μeV/K, almost 3 times the coefficient of the E_x line. The linear increase is weak in comparison to values reported for narrow QWs and comparable with other published results for single QDs (table 5.2). A difference between the linear coefficients for the E_x and E_{xx} broadenings has been reported in the study of InGaAs/GaAs QDs presented in ref. [97] and has no clear explanation. The extrapolated linewidths at 0 K have values of 182 ± 19 μeV (E_x) and 168 ± 49 μeV (E_{xx}).

Material		***A* (μeV/K)**	**T_{range} (K)**	**T_{limit} (K)**	**Linewidth (μeV)**	**REF.**
InAs/GaAs	QD	0,12 – 2,1	5 – 90	40	7,5 @ 5K	[130]
InAs/GaAs	QD	10, 40	10 – 50	40	500 @ 10 K	[131]
InAs/GaAs	QD	0,05 – 0,4	10 – 60	40	10 @ 10 K	[132]
InAs/GaAs	QD	2 – 2,8	4 – 33	33	10 @ 4,2 K	[133]
InAs/GaAs	QD	3,5	5 – 80	50	> 390 @ 5 K	[93]
InAs/$In_{0,12}Ga_{0,88}As$	QD	0,3 – 1,2	4 – 60	40	140 @ 50 K	PW
$In_{0,6}Ga_{0,4}As$ /GaAs	QD	0,05 – 0,1	10 – 90	40	100 @ 5K	[130]
$In_{0,7}Ga_{0,3}As$/GaAs	QD	0,22	7 – 300	30	2 @ 7 K	[134]
$In_{0,50}Ga_{0,50}As$/GaAs	QD	0,4	10 – 95	50	20-200 @ 10K	[46]
InGaAs/GaAs	QD	2,4	10 – 40	40	-	[135]
$In_{0,60}Ga_{0,40}As$/GaAs	QD	0,5	2 – 60	60	1,8 @ 2K	[20]
InGaAs/GaAs	QW	1,5 – 11	-	-	-	[131]

Table 5.2 Reported values for the linear increase coefficient (A) of the linewidth for different QDs and QWs systems. T_{range} indicates the investigated temperature range, while T_{limit} is the upper limit of the linear dependence. The linewidth corresponds to the one of the narrower line and is in many works resolution limited. (PW: present work)

At higher temperatures the thermal excitation of optical phonons and contributions of excited states enhances the exciton scattering considerably, resulting in a strong increase of the linewidth. The presented data, because of the already discussed origin of the linewidth value at 70 K, cannot be conclusive. Nevertheless, the broadening of the lines shows a thermally activated behaviour with an activation energy of about 33 meV (E_x) and 38 meV (E_{xx}), which lie in the InAs and GaAs optical phonons energy range.

5.3 Statistics of measured single QD emission characteristics

Power dependent experiments on single QDs allow to measure the energies of the characteristic emission lines, which comprise the exciton (E_x), biexciton (E_{xx}), first (E_p) and second (E_d) excited levels. In table 5.3 the results of the analysis of spectra from 12 different QDs are presented. The table is completed with the acquisition temperature, the exciton emission (E_x) linewidths, the biexciton binding energy (ΔE_{xx}) and the energy difference between the s- and p- (ΔE_{sp}) and the p- and d-shells (ΔE_{pd}), if these emissions have been clearly identified. The energy of the p- and d- shells refers to the center of the group of lines. Linewidths are reported only if the measurement was performed with the best spectrometer resolution. Biexciton binding energies and energy gap of the first excited level are in agreement with values reported in literature for experiments on single QDs, from which an extensive list is presented in the next chapter in table 6.1. The energy values presented in table 5.3 have been extracted from spectra recorded at a temperature of 50 K (the 2nd column gives the temperature of the measurement), with the exception of the red marked dot #05 (5K) and dot #08 (30K). In this cases the energies have been normalized to 50 K, the correction factors (-0,00298 meV 5→50 K and -0,0021 meV 30→50 K) being extrapolated from the series of measurements presented in fig 5.13 and checked by the acquisition of spectra on dot #11 at 5 K, 30 K and 50 K, which have confirmed the magnitude of the shift.

QD	T (K)	E_x (eV)	E_{xx} (eV)	ΔE_{xx} (meV)	E_p (eV)	ΔE_{sp} (meV)	E_d (eV)	ΔE_{pd} (meV)	Γ_{Ex} (μeV)
01	50	1,1376	1,1338	2,7	1,1512	13,6	1,1873	36,1	240
02	50	1,14	1,1376	2,4	1,1633	23,3	1,1853	22	-
03	50	1,14156	1,13963	1,93	1,1592	17,6	1,1748	15,6	210
04	50	1,1468	1,1448	2,0	1,1657	18,9			-
05	5	1,154	1,1511	2,9	1,1715	17,5	1,1904	18,9	180
06	50	1,1612	1,1567	4,5	1,1962	35	1,2187	22,5	160
07	50	1,1661	1,1632	2,9	1,1911	25			-
08	30	1,1697	1,1656	4,1					190
09	50	1,1806	1,177	3,6					190
10	50	1,18466	1,18055	4,11					190
11	50	1,1873	1,1837	3,6					150
12	50	1,1927	1,1888	3,9					-

Table 5.3 Results of experiments on single InAs/$In_{0,12}Ga_{0,88}As$ quantum dots, with $\Delta E_{sp} \equiv E_p - E_x$ and $\Delta E_{pd} \equiv E_d - E_p$ distances between the first excited (p) to ground (s) and second (d) to first excited (p) levels. Energies values for the red marked dots have been normalized at 50 K.

The single exciton emission of the analysed dots lies between 1,14 eV and 1,2 eV. In fig. 5.7 (section 5.2.1) it is shown that in a relatively small area (7×7 μm^2) it is possible to find dots emitting over this whole energy range, with quite different

biexciton binding energies. The optical properties of QDs can be very inhomogeneous even if the distance between them is very short. The scatter of the E_x, E_{xx}, E_{sp}, E_{pd} values is a consequence of the differences in size, shape, composition and strain induced effects between the dots and of their effect on the optical properties. The interplay of these factors leads to the complicated emission structure, which is an unique characteristic of each dot. In first approximation bigger dots will be characterised by lower ground state emission energy, biexciton binding energy and ground to first excited state energy gap (ΔE_{sp}) than smaller dots. The increase of the ground state emission energy is related to the reduction of the dots dimensions, with the stronger quantization leading to a larger energy difference between ground and first excited energy level, like reported in the literature for etched [36] and self-assembled QDs [43]. This effect is confirmed by the dependence of the measured ΔE_{sp} values on E_x plotted in fig. 5.16.

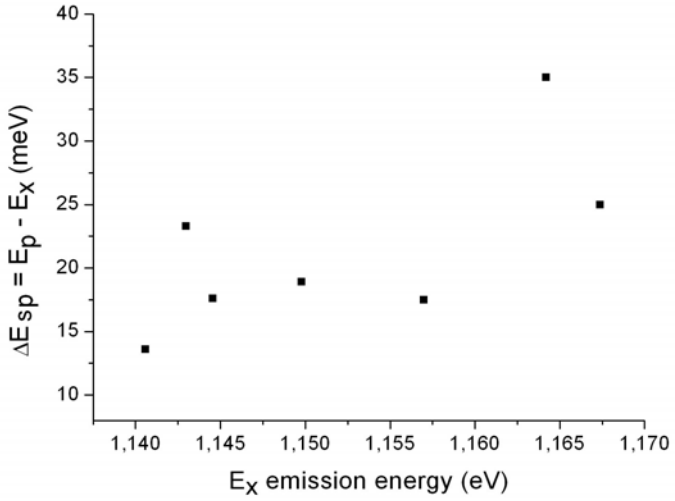

Figure 5.16 Dependence of the energy of the first excited level $\Delta E_{sp} \equiv E_p - E_x$ on the ground state emission energy E_x.

5.3.1 Biexciton binding energies

Measured biexciton binding energies lie in the range of 2 - 4,5 meV, in agreement with values reported in literature and in particular with the work of Kaiser *et al.* [136], where the studied sample consists of InAs QDs on $In_{0,15}Ga_{0,85}As$. In that work the dots are smaller in comparison to the ones investigated here (r ~ 15-20 nm, h ~ 4-7 nm) and characterised by biexciton binding energies ranging between 3,3 meV and 4,8 meV.
In fig. 5.17a the measured ΔE_{xx} are plotted as function of the ground state emission energy E_x and of the distance between the s- and p-shell ΔE_{sp} (5.17b). Both parameters (E_x, ΔE_{sp}) are related to the dimensions of the dots and can be used to parameterise them. The behaviour of ΔE_{xx} shows despite some scatter a trend to

higher values with increasing emission energies, a result well reproduced by the dependence from ΔE_{sp}. The data in this case do not cover all the dots.

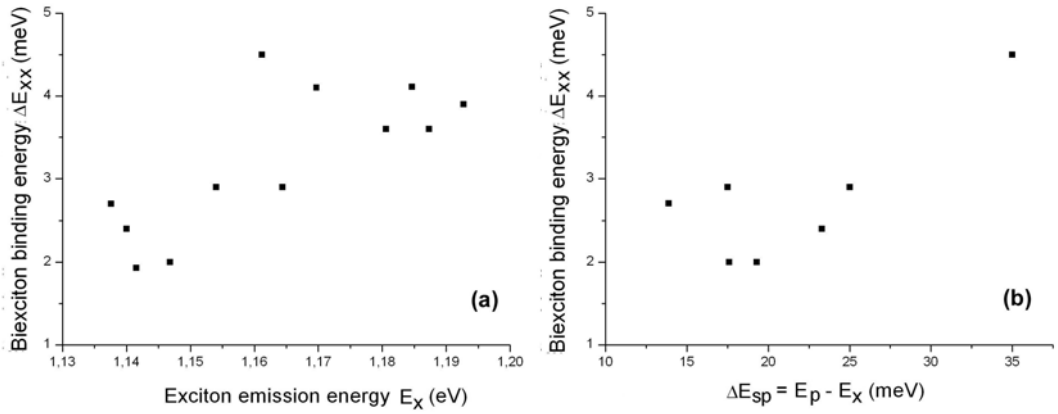

Figure 5.17 (a) Biexciton binding energy (ΔE_{xx}) as function of the ground state emission energy (E_x) and (b) as function of the distance between ground and first excited shell ($\Delta E_{sp} \equiv E_p - E_x$)

The enhancement of the biexciton binding energy with decreasing dot's size is a consequence of the stronger confinement. The dependence of the biexciton binding energy on the dot's dimension for self-assembled QDs is the topic of chapter 6.

5.3.2 Linewidths

In general, the linewidths measured in a non-resonant PL experiment on single QD do not correspond to the homogeneous ones intrinsic of the dot because they might be influenced by fluctuating charge distributions or defects in the dot environment. In this work the resolution of the spectrometer (nominally 124 μeV) does not allow the measurement of the lifetime limited linewidth of the exciton emission (which is believed to be in the order of ~1 μeV to some tens of μeV, section 2.7). The measured linewidth range from 140 μeV[4] at 50 K, which is most probably limited by the resolution of the spectrometer, to 210 μeV (the value of 240 μeV in the table corresponds to a splitted E_x emission) at 50 K. Linewidths of different QDs scatter without regularity and only two of them are resolution limited, while almost half of the values lie in the range 180 – 210 μeV (table 5.3). A rough estimation of the deconvoluted linewidth with

$$\Gamma_{deconv} = \sqrt{\Gamma_{meas}^2 - \Gamma_{res}^2}$$

gives for the lower limit ~60 μeV, which corresponds to a dephasing time of ~20 ps. Values in this range have been reported in various papers [table 5.2 and refs. therein], with the smallest homogenous linewidth of about ~2 μeV [20].

[4] The emission of this dot is not listed in the table, because the biexciton emission has not clearly identified

The accidental overlapping of the emission from different QDs may influence the linewidth, but this is unlikely to happen because of the low dot's density in the investigated region of the sample. The scatter of the linewidths may be caused by different factors, first of all the intrinsic properties which make each QD an unique system, namely his shape, size, composition and strain distribution. A statistics of emission linewidths for $In_{0,5}Ga_{0,5}As$ QDs is presented in the work of Leosson *et al.* [46]. At a given emission energy linewidths values range from ~20 μeV (resolution limit) to about 200 μeV.
Beside the intrinsic fluctuations of the linewidth for each dot and the effect of a unresolved fine structure splitting (argument of the next section), different factors may cause the observed broadening of the exciton emission lines at a fixed temperature, like interactions with phonons, carrier-carrier scattering, spectral diffusion. Almost all the presented linewidth values have been extracted from spectra acquired at a temperatures of 50 K. This temperature lies near the upper limit, where the broadening is dominated by the interaction with acoustic phonons and optical phonons starts to play an important role. No jitter nor blinking have been observed in the present study, probably because the time scale involved in these processes are much shorter than the integration times normally used for a single spectrum acquisition, while shifts due to the quantum confined Stark effect may be a reason for the broadening of the measured linewidths.

5.3.3 Fine structure

Another effect which can influence the measured linewidth is the fine structure splitting of the ground state emission, due to the asymmetry of the dots shape and to the atomistic structure of the dot itself (section 2.6). In ref. [113] dots of similar composition to the here investigated ones (InAs/InGaAs) present a strong asymmetrical shape, which would lead to a splitting of the E_x and E_{xx} lines. If the distance between the doublets is less or in the order of the spectral resolution, the effect of this splitting is the broadening of the line.

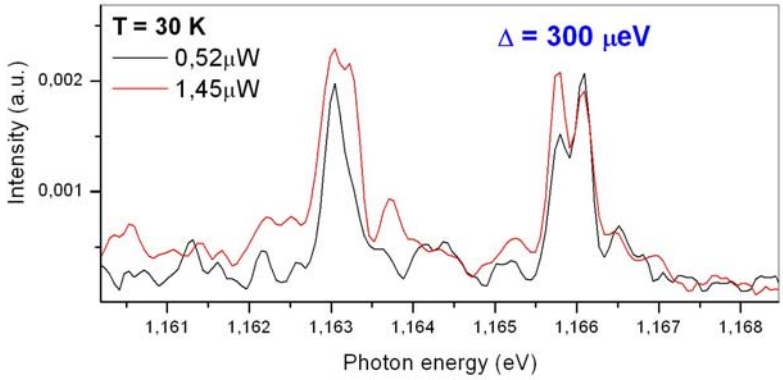

Figure 5.18 Splitting of the ground state E_x and of the biexciton E_{xx} lines observed for dot #07.

The differences in the QDs shapes and their asymmetry, will lead to different splitting magnitudes, which could explain the scatter of the linewidths values. A

fine structure have been observed for two of the studied QDs (#01, #07 in table 5.3), which present a splitting of the ground state emission in two lines. For dot #07 this effect can be recognised in the biexciton line too (fig. 5.18). The fine structure components in the excitonic and biexcitonic emissions are expected to be linearly cross polarised to each other, but the lack of polarisation control on the detected signal in our set-up has not allowed a further investigation of this effect.

System	Lines	Splitting (μeV)	Ref.
InAs/GaAs	E_x / E_{xx}	60 – 134	[44]
In(Ga)As/(Al)GaAs	E_x	< 450	[33]
InAs/$In_{0,12}Ga_{0,88}As$	E_x / E_{xx}	300, 650	present work
$In_{0,6}Ga_{0,4}As$/GaAs	E_x	120 – 150	[137]
$In_{0,6}Ga_{0,4}As$/GaAs	E_x	200	[138]
InAs/$Al_{0,6}Ga_{0,4}As$	E_x	500 – 1000	[139]

Table 5.4 Magnitude of the fine structure splitting in the QDs emission spectra reported for different material systems.

The observed magnitudes of the splitting (300 μeV and 650 μeV) lie in the range of the values reported in the literature, as presented in table 5.4. From the spectrum in fig 5.18 it is clear, that a splitting of less than 300 μeV can not be resolved by the spectrometer and leads to a broadening of the linewidth.

6. Biexciton binding energy in semiconductor QDs

6.1 Single QD experiment statistics

Despite the fact that it is possible to gain some information about the geometry of self-assembled QDs with SFM on uncapped[5] and TEM imaging techniques on capped samples, in single self-assembled QD spectroscopy there is no exact knowledge about the geometry of the particular dot under investigation. The problem is even more complicated, due to the complex influence of composition and strain distribution of the dot and its surrounding matrix on the emission properties. Therefore a straightforward comparison of the experimental data with detailed theoretical calculations is not yet possible.
One way to estimate the dimensions of an investigated single self-assembled QD is to proceed backwards, i.e. to calculate the spectrum and to adapt the model to the observed optical characteristics. In refs. [19][30] the spectrum is obtained solving the problem with the assumption of a simplified confinement potential, dealing with the dimensions of the dots as free parameters, which have to be calculated fitting the observed emission lines, e.g. level separations and inter-shell spacing between lines. A good agreement with the experimental data and with dimensions obtained from cross section TEM images of similar dots has been achieved. Correlation between average optical emission characteristics and size of the dots has been quantitatively demonstrated in ref. [47]. The observed multimodal distribution of the exciton ground state recombination energy in an ensemble of self-organized InAs/GaAs QDs has been explained by a shell-like growth of the dots. The QD's optical properties have been obtained from numerical eight-band **k·p** calculations, including inhomogeneous strain distribution, piezoelectric potential, interband mixing and Coulomb interactions. This model shows an excellent agreement with the experimental data, if the volume of the QD is supposed to follow a shell-like evolution: the QD's base length increases in 2 monolayers steps with increasing height (in monolayer steps) [48]. Therefore the average base length and height of

[5] Keeping in mind that the capping process influences the QD's geometry and composition.

the QDs are correlated and the aspect ratio becomes larger with increasing volume of the dot.
The direct information that can be obtained about the geometry of capped dots is deduced from TEM and STM images of a sample section. The problem of these measurements is that the geometry has to be extrapolated from a cross section of the dot [41]. In this way the height can be measured very precisely, but only a raw estimation of the lateral extension can be obtained. Furthermore, it is practically impossible to get the structural properties of the spectroscopically investigated QD.

In the following table characteristic experimental data (material system under study, masking of the sample, shape and size of the dots, temperature of the measurement) and optical emission characteristics (E_x, ΔE_{xx}, ΔE_{sp}) have been collected from publications about experiments on single QDs. Only systems based on the III-V elements Al, Ga, In and As have been taken into consideration, without of course any sake of completeness. Almost all the samples were fabricated by the Stranski-Krastanov self-assembling growth method with the exception of some lithographically defined QDs and of a few QW thickness fluctuation dots in the systems with Al content. The aim of this research is first of all to compare the results of the present work with similar experiments and furthermore to gain some insights into the dependence of the optical properties from the geometrical characteristics of the dots, keeping in mind the already described partial knowledge about size and shape.

REF.	QDs composition	M	S	Size (nm×nm)	E_x (eV)	ΔE_{xx} (meV)	ΔE_{sp} (meV)	T (K)
InAs/InGaAs								
[136]	InAs/$In_{0,15}Ga_{0,85}As$	×	L	15-20×4-7	1,078-1,093	3,3→ 4,8		
PW	InAs/$In_{0,12}Ga_{0,88}As$		TP	36 × 9	1,14→1,2	2 → 4,5	14-36	4
InAs/GaAs – InGaAs/GaAs - InAs/AlGaAs								
[45]	InAs/GaAs		TP	13 × 2-3	1,2→1,34	1,3→ -6,3		6
[140]	$In_{0,5}Ga_{0,5}As$/GaAs	×	L	23 × 2,5	1,262	~ 2	30	2,3
[128]	$In_{0,6}Ga_{0,4}As$/GaAs	×	D		1,28	~ 3	50	1,2
[29]	$In_{0,4}Ga_{0,6}As$/GaAs	×			1,283	2,7	20	2,3
[43]	InAs/GaAs			45×40×4,5	1,284	3,5	40	
[138]	$In_{0,6}Ga_{0,4}As$/GaAs	×		20	1,29	3	30	1,5
[141]	$In_{0,5}Ga_{0,5}As$/GaAs	×			1,3075	~ 3		2,3
[126]	InAs/GaAs		L	40-50×3	1,3078	3,5		4-7
[30]	InAs/GaAs				1,31		~40	4
[142]	$In_{0,6}Ga_{0,4}As$/GaAs	×	H	10	1,3196	3,1	30	1,5
[143]	$In_{0,4}Ga_{0,6}As$/GaAs				1,32	3	40	
[5]	InAs/GaAs				1,3222	2,6		4
[19]	InAs/AlGaAs			20-40×2-6	1,325		50	10
[122]	InAs/GaAs		L	35 × 4,5	1,3406	~ 3	30	4
[144]	InAs/GaAs			10-12×4	1,342	- 0,8	60	5
[145]	$In_{0,5}Ga_{0,5}As$/GaAs	×			1,3436	2,8	30	2,3

[146]	InAs/GaAs	×		18×18×5	1,3453	2	35-45	10
[147]	$In_{0,5}Ga_{0,5}As$/GaAs			30×15unc	1,361	2,2	30	<10
[148]	InAs/GaAs			10-12 × 4	1,3726	- 1,7		5
[49]	InAs/GaAs				1,3748	- 1,1		5
[127]	InAs/GaAs	×		20 × 2	1,375	- 3		
[6]	InAs/GaAs	×			1,4145	1,7		5
[39]	$In_{0,14}Ga_{0,86}As$/GaAs		Lit	50 → 120	~1,429	1 → 2		1,5
[39]	$In_{0,14}Ga_{0,86}As$/GaAs		Lit	50 × 5		2		1,5
[39]	$In_{0,14}Ga_{0,86}As$/GaAs		Lit	60 × 5		1,6	4	1,5
AlInAs/AlGaAs - GaAs/AlGa - GaAs/AlGaAs - InGaAs/AlGaAs - InAs/AlAs								
[67]	AlInAs/AlGaAs	×	L	20 × 5	1,6008	5	70	1,2
[149]	GaAs/AlGa		Tf		1,6088	3,1		
[150]	GaAs/AlGaAs	×	Tf		1,6212	3,36		
[151]	InAs/AlAs	×		25-30 × 3	1,63	- 0,4		8
[123]	GaAs/AlGaAs		Tf		1,6586	4,2		5
[135]	$In_{0,4}Ga_{0,6}As$/AlGaAs			30 × 3,5	1,6682	2,8		
[152]	$In_{0,4}Ga_{0,6}As$/AlGaAs	×	D	30 - 100	1,67	4,7		3,8
[153]	GaAs/AlGaAs		Tf		1,688	1,3		

Table 6.1 Collection of results from single QDs experiments on III-V systems from literature. Size of the dots is normally length (radius) × height expressed in nm. (M = masking with etched mesa or metal layer mask, S = shape, D = disc, H = hemisphere, L = lens, Tf = thickness fluctuation, TP = truncated pyramid, Unc. = uncapped, Lit = lithographically defined). PW indicates the experimental results of the present work.

Masking (M) means that the sample has been modified to perform experiments on a single QD by etching small mesas or patterning the surface with small apertures in an opaque metal layer. Data about size and shape (S) are the results from SFM and TEM studies of the samples, and in general only base length (or radius) and height (in nm) are reported. For the shape the following abbreviations have been used: D = disc, H = hemisphere, L = lens, Tf = thickness fluctuation, TP = truncated pyramid, Unc. = uncapped, Lit = lithographically defined. Not every paper reports all these parameters. Furthermore because of the different temperatures the emission energy values are not exactly comparable. Nevertheless, all the experiments have been performed at temperatures below 10 K, which implies a very small correction, in the order of a few hundred μeV (data of the present work have been normalized at 5 K).

The data in the table are listed in order of increasing ground state emission energies (E_x), starting from the lowest (1,08 – 1,2 eV) of the two InAs/$In_xGa_{1-x}As$ systems [136, present work]. The most widely studied InAs/GaAs and $In_xGa_{1-x}As$/GaAs QDs systems emit in the range between 1,2 eV and 1,36 eV, while at higher energies (1,6 – 1,7 eV) lies the emission of systems with Al content. Different sample structure (thickness and composition of the layers) and growth conditions (temperature, annealing after growth) lead to the variety of optical characteristics (E_x, ΔE_{xx}, ΔE_{sp}) reported in table 6.1. The following analysis focuses on the size dependence of the biexciton binding energy ΔE_{xx}, plotted in fig. 6.1 as a function of

the ground state emission energy E_x. The green and red areas indicate that the reported experimental results lie approximately in the marked range.

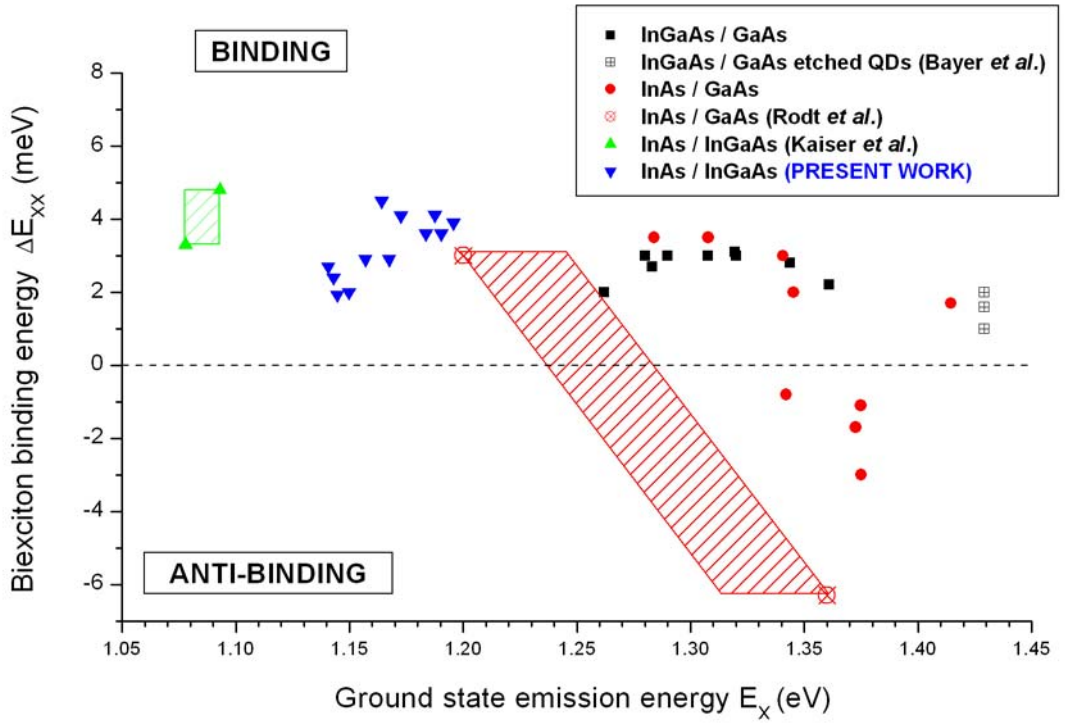

Figure 6.1 The biexciton binding energy ΔE_{xx} dependence on the ground state emission energy E_x of single QDs made from different materials (data of table 6.1).

The data of the biexciton binding energies (ΔE_{xx}) show both, positive (binding) and negative (anti-binding) values. The positive ΔE_{xx} lie in the range between 0 – 5 meV, while negative ΔE_{xx} range from 0 to -6,3 meV. Only InAs/GaAs QDs and the InAs/AlAs system show negative ΔE_{xx}. In particular the work of Rodt *et al.* [45] have to be mentioned, which presents a statistics of E_x and ΔE_{xx} over more than 70 dots of the same InAs/GaAs sample (whose data are represented by the red highlighted area in fig. 6.1). Some comments to the plot:

- growing InAs on $In_xGa_{1-x}As$ shifts the emission to lower energies in comparison to a GaAs substrate

- InAs and $In_xGa_{1-x}As$ dots on GaAs emit almost in the same spectral region. Ga inclusion increases the bandgap energy, thus $In_xGa_{1-x}As$ QDs have to be larger than the pure InAs ones to emit at the same energy. Data of $In_xGa_{1-x}As$ QD's dimensions do not confirm the expected behaviour, i.e. InAs dots emitting at the same energy and with comparable ΔE_{xx} binding energy are larger. Probably this is due to the scarce information about the dimensions of the InGaAs dots available in the considered experiments.

- inclusion of Al in the substrate shifts the emission to higher energies. The scatter in the data about these QDs systems is due to the variety of compositions (AlInAs/AlGaAs - GaAs/AlGa - GaAs/AlGaAs - InGaAs/AlGaAs - InAs/AlAs) and to the different morphological characteristics originating from the used growth techniques (self-assembly and thickness fluctuations).

6.2 Biexciton binding energy dependence on the QD's section area and aspect ratio

Biexciton binding energy is defined as $\Delta E_{xx} = 2E_x - E(biexc)$, the difference between the ground states energy of two independent excitons and the biexciton ground state energy. As noted in par. 2.5 the concept of a binding energy in a QD is not really appropriate, because no unbound state is possible like in the case of a system of higher dimensionality (QWR, QW, bulk). The biexciton binding energy (ΔE_{xx}) results from the Coulomb interaction between the four carriers localized in the confinement potential of the QD. Depending on the geometrical and chemical characteristics of the dot and the surrounding matrix, the change in the total energy of the few-particles system with respect to the sum of energies of the contributing single-particle states can be either positive ($\Delta E_{xx} > 0$, i.e. binding state) or negative ($\Delta E_{xx} < 0$, i.e. anti-binding state).
Within the same material system it is expected in a first approximation that bigger dots present lower emission energies, lower biexciton binding energies and lower ground to first excited level distances in comparison to smaller dots. The enhancement of the biexciton binding energy with decreasing dot's size has been demonstrated in the systematic study of QDs defined by lithography and etching [36][37][39]. In ref. [39] the dots have been fabricated in form of boxes or cylinders from a 5 nm thick $In_{0,14}Ga_{0,86}As$/GaAs QW with lateral sizes or radii ranging from 50 nm to 120 nm. An increase of the biexciton binding energy (~1 meV $\rightarrow$ ~2 meV) has been observed.
In what follows the data presented in table 6.1 are analysed in detail. Fig 6.2a shows the dependence of ΔE_{xx} on the section area of the QDs. Without knowledge about the exact dimensions and shape (disc, lens, hemisphere, truncated pyramid), the QD section has been approximated (in excess) by a box of dimensions equal to the reported length (or radius) and height values. In the plot the size of the box near every experimental point is proportional to the QD's dimensions. In case of the InAs/GaAs system, the transition from positive to negative biexciton binding energies with decreasing dot's section area and consequently dot's size can be observed.

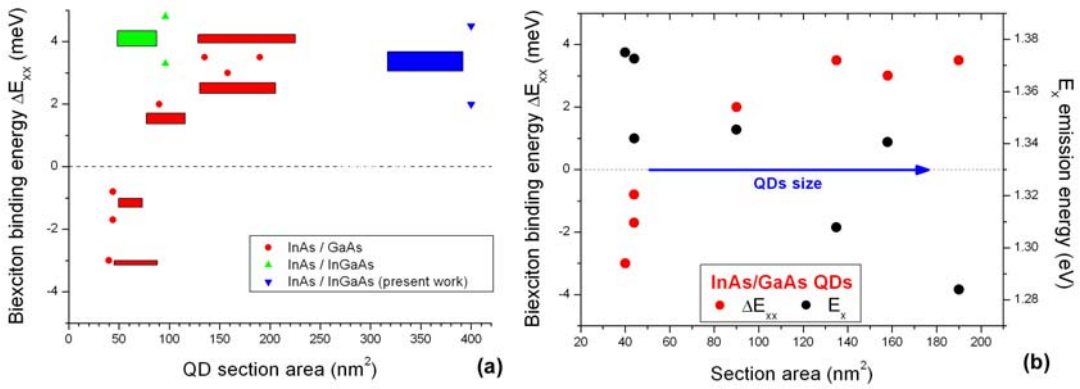

Figure 6.2 (a) Dependence of the biexciton binding energy from the QDs section area, defined as the product of the given length (radius) and height. (b) ΔE_{xx} (red dots) and E_x (black dots) data about InAs/GaAs QDs. The size of the boxes is proportional to the QD's dimensions.

Fig. 6.2b the dependence on the section area of ΔE_{xx} (left axis) and E_x (right axis) for InAs/GaAs QDs are plotted, showing a clear regular trend: increasing the size the ground state emission energy decreases monotonically, while the biexciton binding energy jumps from negative to positive values reaching a plateau at about 3 meV. The smallest QDs (20×2 nm^2 and 11×4 nm^2 in the plot) are thus characterised by a strong repulsive Coulomb interaction between the confined carriers, which overcomes the positive terms leading to the observed negative ΔE_{xx}. Remarkably the data presented in ref. [45] acquired on a single sample show the same ΔE_{xx} sign reversal (from positive to negative) with decreasing dots size.

The shape is another important parameter which influences the optical emission characteristics of the QDs. Fig 6.3 shows the dependence of the biexciton binding energy from the aspect ratio, defined as the ratio between the reported height and base length (or radius) values.

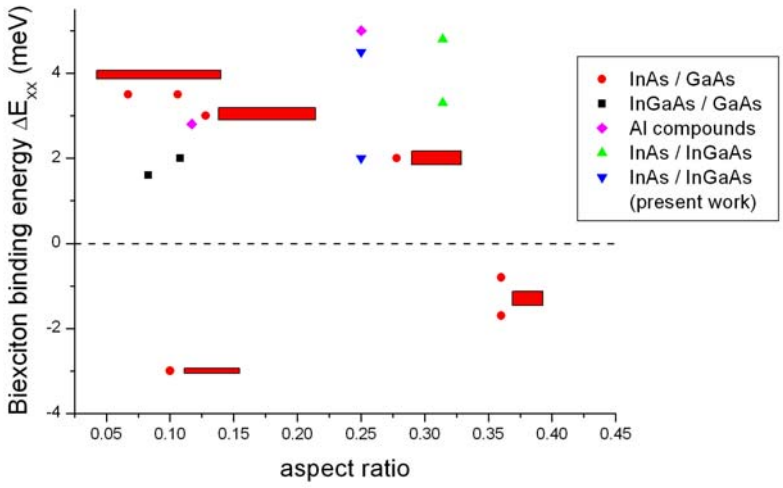

Figure 6.3 Dependence of the biexciton binding energy on the QD's aspect ratio. The size of the boxes is proportional to the QD's dimensions.

The data set regarding InAs/GaAs QDs (red circles) presents a regular trend, namely a decrease of the biexciton binding energy with increasing aspect ratio and the transition from positive to negative ΔE_{xx} values. This behaviour is in agreement with the theoretical calculation reported in ref. [57], which models the transition at constant volume of a InAs/GaAs QD from flat truncated pyramid to pyramid. The transition is due to the strong influence of the QD's shape on the electronic structure: as the pyramidal shape is approached the carriers wave functions become more and more different under the impact of the piezoelectric potential, reducing the positive contributes to the biexciton binding energy. A more detailed knowledge of the QD's shape is necessary to confirm the predicted behaviour.

6.3 Biexciton binding energy dependence on size for InAs QD's

Turning back to the representation of ΔE_{xx} in dependence on E_x, in fig. 6.4 are reported ΔE_{xx} values for the InAs/$In_{0,12}Ga_{0,88}As$ and InAs/GaAs QD systems. As already pointed out the experimental data for the InAs/$In_{0,12}Ga_{0,88}As$ QDs studied in the present work show an increase of the biexciton binding energy with increasing ground state emission (decreasing dots size), from about 2 meV to 4,5 meV, which is compatible with an enhancement of the binding energy due to the stronger confinement in smaller dots. The scatter of the data reflects the great impact of the morphological characteristics of each dot on the optical emission properties. The dots are characterised by a base length in the range between 30 and 40 nm and a height of about 9 nm. The data about InAs/GaAs present the transition from positive to negative biexciton binding energies and dots with cross section areas ranging from about 40×4 nm^2 to 12×2 nm^2.
The proposed trend for the dependence on size of the biexciton binding energy in self-assembled InAs QDs is represented by the black curve. At low emission energies (large dots) it is reasonable to assume that the biexciton binding energy tends to the value in a QW of thickness comparable to the QD height. By decreasing the dot size (increasing E_x) the confinement enhances the binding energy, till ΔE_{xx} reaches a maximum and starts to decrease, in analogy with the described dependence in QW structures (section 2.5). A similar behaviour has been demonstrated for CdSe nanocrystals [154]. The experimental data for InAs on GaAs QDs indicate that a further decrease of the dot's size leads to a transition from positive to negative biexciton binding energy values. The proposed behaviour disagrees with the dependence on size of the biexciton binding energy for piezoelectric pyramidal InAs/GaAs QDs as calculated in ref. [56], where negative values are predicted for "large" dots (12 nm basis length) and positive for smaller ones. The imbalance between exchange-correlations and direct Coulomb energy is explained there with the effect of the strain induced piezoelectric field, which spatially separates electrons and holes reducing their mutual attraction and exchange and increasing the Coulomb repulsion between equally charged carriers. This effect scales linearly with the dots dimensions, thus from a negative biexciton

binding energy for large dots a transition to positive values is predicted reducing dots size, which is in contrast to the experimental results.

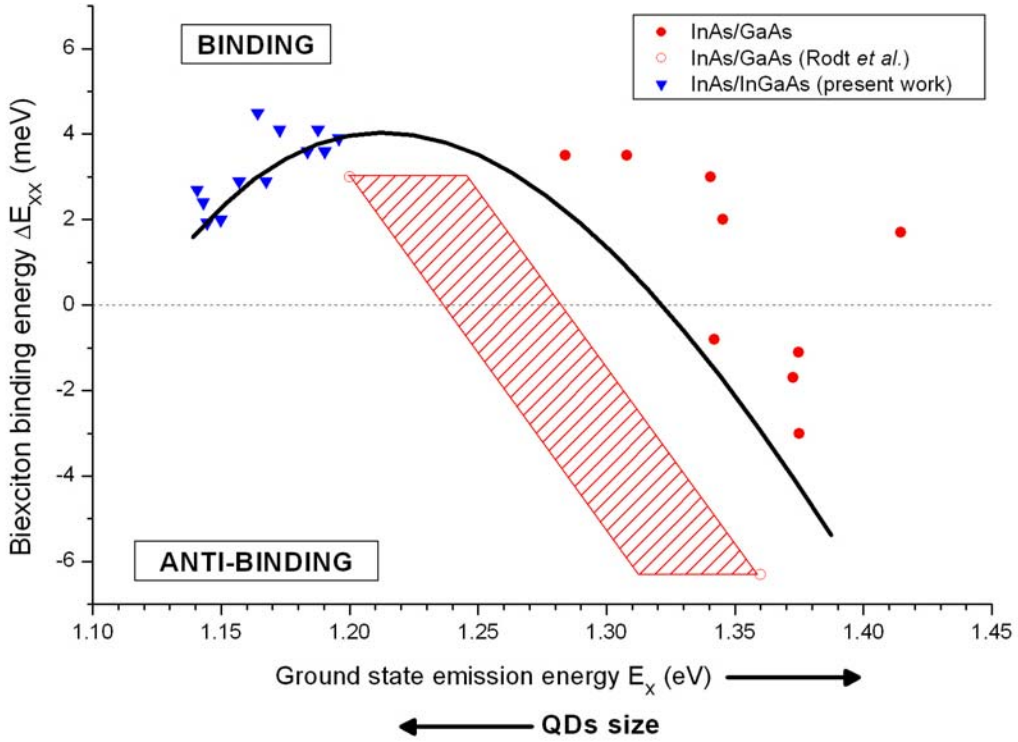

Figure 6.4 Biexciton binding energy (ΔE_{xx}) vs. ground state emission energy (E_x) data for InAs/$In_{0,12}Ga_{0,88}As$ and InAs/GaAs QDs and proposed curve (black line) for the dependence on size of the biexciton binding energy.

The behaviour proposed here summarizes the data for InAs dots and, for small dots, follows the predicted transition from binding to anti-binding state presented in refs. [44][45]. An important point has to be considered: the experimental data refer to QD's characterised by inhomogeneous growth conditions, resulting in dots with similar compositions, but quite different ground state emission energies. This is clear from fig. 6.4: the red dots are experimental results on different samples, while the red marked area represents the data acquired on a single sample. Both sets of data present the same trend, namely the transition to negative values whit decreasing dots dimensions, but shifted in energy. A systematic study on a single sample is required to confirm the proposed trend and to correlate it with the ground state emission energy and with the actual dots dimensions.
Furthermore the influence of parameters like shapes and compositions, even within the same material system needs to be investigated. These parameters have a great impact on the single particle wave functions and consequently on the biexciton binding energy. Indeed in a flat QD with truncated pyramidal shape the electron and holes wave functions present an optimal overlap, with the hole strongly localized than the electron, because of the larger effective mass. The theoretically predicted biexciton binding energy does not present transition from positive to

negative values while decreasing the size [45]. An experimental point in fig. 6.3 probably disagrees with this prediction, because the very flat QD (20×2 nm^2) is characterised by a negative binding energy. This example confirms the difficulties in the comparison between theoretical predictions and experimental results. At the same time material characteristics strongly influence the electronic properties. High indium content increases the sublevel splitting, thus quenches the impact of correlation and exchange (positive contributes to the biexciton binding energy). Furthermore in less strained QDs, or in QDs which consist of less piezoelectric materials, the piezoelectric effect has a less pronounced impact. The balance between all these factors depends on the particular QD's system and can be investigated with systematic studies on different samples.

7. Summary and outlook

Single QD spectroscopy allows to measure the emission spectrum without the obstructing influence of inhomogeneous broadening resulting from statistical variations of the structural properties of QD's emission. In this way it is possible to observe in the spectra the signatures of individual QDs, like the quantisation of the energy levels and their renormalization due to many-particle occupancy.
In this thesis single QD spectroscopy was done using a low temperature micro-photoluminescence system, on a sample where the interdot separation is larger than the spatial resolution. The experimental set-up has been developed on the basis of a cold finger cryostat combined with a Fourier Transform spectrometer and optimised to have an efficient long term spatial stability and to collect a maximum of the QD's emission. The QD samples consist of self-assembled InAs QDs embedded in an $In_{0,12}Ga_{0,88}As$ QW surrounded by a GaAs matrix and emitting in the near infrared. TEM pictures show QDs characterised by a truncated pyramidal form, with a base length in the range between 30 and 40 nm and a height of about 9 nm.
Photoluminescence of the QDs was excited non resonantly with a He-Ne laser and single dot spectroscopy was carried out at temperatures below 60 K. The emission spectra of a single QD shows the characteristic dependence with increasing excitation power density, namely the appearance of the single exciton emission line, followed by the biexciton line on the lower energy side. A further increase leads to the emission from excitons occupying higher energetic shells in the dot. Varying the sample temperature, the ground state emission energy shows the characteristic redshift related to the shrinking of the semiconductor band gap, while the linewidth is broadened due to the coupling with acoustic and optical phonons. A statistics of exciton, biexciton and excited states emission energies of a dozen of dots was acquired.

Although the intrinsic optical properties of a QD can be studied with this kind of experiments, the interpretation of the data is a complex task, because of the lack of knowledge about the geometrical and chemical properties of the particular QD under investigation. Therefore a straightforward comparison of the experimental results with detailed theoretical calculations is yet not possible.

Up to now, reliable information on the geometrical structure and on the optical properties of the same QD could not be obtained, at least not for epitaxially grown self-assembled QDs. For this reason the interplay of geometry and material composition on one side and the optical properties on the other side, can be understood only comparing experimental data and theoretical calculations for different QD shapes, sizes and compositions.

The small statistics of optical properties of the here investigated QDs has been compared with single QD spectroscopy experimental data available in the literature, for III-V material systems. Despite the uncertainty about the dot's dimensions, from the analysis of these data a general trend can be found for the dependency of the biexciton binding energy on the size of InAs QDs, parameterised by their ground state emission energy. These results agree with some of the published theoretical predictions, showing the utility of a comparative study of single QD spectroscopy experimental data. A more systematic research, with the investigation of a large number of individual QDs within the same sample and on different samples, can lead to a better understanding of the complex interplay between the geometrical and chemical factors (size, shape, composition, strain and piezoelectric effects), which determine the optical characteristics of the dots.
The observation of a multimodal distribution in the ground state emission of a QDs ensemble, explained by a monolayer shell-like difference in the average dots dimensions, can be exploited to improve the results of further investigations of size related effects. Optical experiments on single QDs belonging to one subensemble may help to understand the parameters which determine the broadening of the optical properties of dots characterised by the same mean volume. Furthermore a comparison between subensambles will address the impact on the optical spectra of the monolayer difference in the dots volume. At the same time a more detailed knowledge about the QD's geometry is necessary, which can be obtained by systematic TEM and STM studies of the optically investigated QD samples.

Appendix

Abbreviations list:

QD	quantum dot
SAQD	self-assembled quantum dot
PL	photoluminescence
μ-PL	micro-photoluminescence
LHe	liquid helium
FT	fourier transform
He-Ne	helium neon
Nd-Yag	neodymium yttrium aluminium garnet
LED	light emitting diode
EL	elettroluminescence
CL	chatodoluminescence
PLE	photoluminescence excitation
SIL	solid immersion lens
SNOM	scanning near field microscopy
QW	quantum well
QWR	quantum wire
TEM	transmission electron microscope
ML	monolayer
NIR	near infrared
MBE	molecular beam epitaxy
MOVCD	metalorganic chemical vapour deposition
DOS	density of states
EPM	empirical pseudopotential method
LH	light hole
HH	heavy hole
SO	split-off
RHEED	reflection high energy electron diffraction
FWHM	full width at half maximum
ZPL	zero phonon line
QCSE	quantum-confined Stark effect
RMS	root mean square
SFM	scanning force microscopy
STM	scanning tunnelling microscopy
NA	numerical aperture
CCD	charge coupled device
CW	continuous wave
FIB	focussed ion beam
EBM	electron beam lithography

Used variables:

E_x	exciton emission energy
E_{xx}	biexciton emission energy
ΔE_{xx}	biexciton binding energy
E_p	center of the p-shell emission (first excited level)
E_d	center of the d-shell emission (second excited level)
$\Delta E_{sp} \equiv E_p - E_x$	energy gap between first excited level and ground state
$\Delta E_{pd} \equiv E_d - E_p$	energy gap between first and second excited levels
H	Hamiltonian
Θ_D	Debye temperature
T	temperature
t	time
T_1	longitudinal relaxation time
T_2	transverse relaxation time
T_2'	pure phase relaxation time
Γ	linewidth
Γ_0	homogeneous linewidth
γ	inhomogeneous broadening
A	temperature linewidth broadening: linear coefficient
E_A	temperature linewidth broadening: activated coefficient

Fundamental physical constants:

$\hbar = h / 2\pi$	$= 1{,}05457168 \cdot 10^{-34}$ J·s	Planck's constant
	$= 6{,}5821191 \cdot 10^{-13}$ meV·s	
k_B	$= 1{,}3806505 \cdot 10^{-23}$ J/K	Boltzmann constant
	$= 8{,}6173432 \cdot 10^{-2}$ meV/K	
m_e	$= 9{,}10938188 \cdot 10^{-31}$ Kg	electron mass

Unity conversion:

1 wave number (cm^{-1}) = 0,1239841856 meV

Material parameters at 300 K

	Symbol	**GaAs**	**InAs**	**Unit**
Crystal structure		zinc blende	zinc blende	
Lattice constant (300 K)	a_0	5,65325	6,0583	Å
de Broglie electron λ		24	40	nm
Exciton Bohr radius	a_r^{exc}	~10		nm
Bandgap energy (300 K)	E_g	1,424	0,356	eV
Debye temperature	Θ_D	360	280	K
Relative dielectric constant	ε_r	13,18	15,15	-
Effective electron mass	m_e^*	0,063 m_e	0,027 m_e	-
Effective heavy hole mass	m_{hh}^*	0,51 m_e	0,41 m_e	-
Effective light hole mass	m_{lh}^*	0,082 m_e	0,025 m_e	-
LO phonon energy		36,25	29	meV
TO phonon energy		33,29	27	meV
Piezolelectric constant	e_{14}	-0,16	$-4{,}15\cdot10^{-2}$	$C\cdot m^{-2}$

Bibliography

[1] D. Bimberg, M. Grundmann, N. N. Ledentsov. Quantum dot heterostructures. *John Wiley & Sons*, Chichester (1999)

[2] D. Bimberg, N. Ledentsov. Quantum dots: lasers and amplifiers. *J. Phys.: Condens. Matter.*, **15**, R1063 (2003)

[3] A. Fiore, J. X. Chen, M. Ilegems. Scaling quantum-dot light-emitting diodes to submicrometer sizes. *Appl. Phys. Lett.*, **81**, 10, 1756 (2002)

[4] S. Chakrabarti, A. D. Stiff-Roberts, X. H. Su, P. Bhattacharya, G. Ariyawansa, A. G. U. Perera. High-performance mid-infrared quantum dot infrared photodetectors. *J. Phys. D.: Appl. Phys.*, **38**, 2135 (2005)

[5] P. Michler, A. Kiraz, C. Becher, W. V. Schoenfeld, P. M. Petroff, L. Zhang, E. Hu, A. Imamoglu. A quantum dot single-photon turnstile device. *Science*, **290**, 2282 (2000)

[6] C. Santori, M. Pelton, G. Solomon, Y. Dale, Y. Yamamoto. Triggered single photons from a quantum dot. *Phys. Rev. Lett.*, **86**, 8, 1502 (2001)

[7] G. Chen, N. H. Bonadeo, D. G. Steel, D. Gammon, D. S. Katzer, D. Park, L. J. Sham. Optically induced entanglement of excitons in a single quantum dot. *Science*. **289**, 1906 (2000)

[8] D. Bouwmeester, A. Ekert, A. Zeilinger. The physics of quantum information. *Springer*, Berlin (2000)

[9] D. Loss, D. DiVincenzo. Quantum computation with quantum dots. *Phys. Rev. A*, **57**, 1, 120 (1998)

[10] F. Troiani, U. Hohenester, E. Molinari. Exploiting exciton-exciton interactions in semiconductor quantum dots for quantum-information processing. *Phys. Rev. B*, **62**, 4, R2263 (2000)

[11] E. Biolatti, R. C. Iotti, P. Zanardi, F. Rossi. Quantum information processing with semiconductor macroatoms. *Phys. Rev. Lett.*, **85**, 26, 5647 (2000)

[12] M. Bayer, A. Schmidt, A. Forchel, F. Faller, T. L. Reinecke, P. A. Knipp, A. A. Dremin, V. D. Kulakovskii. Electron-hole transitions between states with nonzero angular momenta in the magnetoluminescence of quantum dots. *Phys. Rev. Lett.*, **74**, 17, 3439 (1995)

[13] K. Brunner, U. Bockelmann, G. Abstreiter, M. Walther, G. Böhm, G. Tränkle, G. Weimann. Photoluminescence from a single GaAs/AlGaAs quantum dot. *Phys. Rev. Lett.*, **69**, 22, 3216 (1992)

[14] Y. Arakawa. Fabrication of quantum wires and dots by MOCVD selective growth. *Solid State Electron.*, **37**, 4-6, 523 (1994)

[15] U. Woggon. Optical properties of semiconductor quantum dots. *Springer*, Berlin, 1996

[16] A. Zrenner. L. V. Butov, M. Hagn, G. Abstreiter, G. Böhm, G. Weimann. Quantum dots formed by interface fluctuations in AlGa/GaAs coupled quantum well structures. *Phys. Rev. Lett.*, **72**, 21, 3382 (1994)

[17] I. N. Stranski, L. von Krastanow. *Akad. Wiss. Lit. Mainz Abh. Math. Naturwiss. Kl.*, **146**, 797 (1939)

[18] A. Gustafsson, M.-E. Pistol, L. Montelius, L. Samuelson. Local probe techniques for luminescence studies of low-dimensional semiconductor structures. *J. Appl. Phys.*, **84**, 4, 1715 (1998)

[19] E. Dekel, D. Gershoni, E. Ehrenfreund, D. Spektor, J. M. Garcia, P. M. Petroff. Multiexciton spectroscopy of a single self-assembled quantum dot. *Phys. Rev. Lett.*, **80**, 22, 4991 (1998)

[20] M. Bayer, A. Forchel. Temperature dependence of the exciton homogeneous linewidth in $In_{0,60}Ga_{0,40}As$/GaAs self-assembled quantum dots. *Phys. Rev. B*, **65**, 41308R (2002)

[21] N. H. Bonadeo, J. Erland, D. Gammon, D. Park, D. S. Katzer, D. G. Steel. Coherent optical control of the quantum state of a single quantum dot. *Science*. **282**, 1473 (1998)

[22] T. Flissikowsky, A. Hundt, M. Lowisch, M. Rabe, F. Henneberger. Photon beats from a single semiconductor quantum dot. *Phys. Rev. Lett.*, **86**, 14, 3172 (2001)

[23] A. Zrenner. A close look on single quantum dots. *J. of. Chem. Phys.*, **112**, 18, 7790 (2000)

[24] S. M. Mansfield, G. S. Kino. Solid immersion microscope. *Appl. Phys. Lett.*, **57**, 24, 2615 (1990)

[25] Q. Wu, R. D. Grober, D. Gammon, D. S. Katzer. Excitons, biexcitons, and electron-hole plasma in a narrow 2.8-nm GaAs/$Al_xGa_{1-x}As$ quantum well. *Phys. Rev. B*, **62**, 19, 13022 (2000)

[26] D. W. Pohl, W. Denk, M. Lanz. Optical spectroscopy: image recording with resolution lambda/20. *Appl. Phys. Lett.*, **44**, 7, 651 (1984)

[27] K. Matsuda, T. Saiki, S. Nomura, M. Mihara, Y. Aoyagi, S. Nair, T. Takagahara. Near-field optical mapping of exciton wave functions in a GaAs quantum dot. *Phys. Rev. Lett.*, **91**, 17, 177401 (2003)

[28] P. Michler. Single quantum dots. Foundamentals, applications and new concepts. *Springer*, Berlin (2003)

[29] F. Findeis, A. Zrenner, G. Böhm, G. Abstreiter. Optical spectroscopy on a single InGaAs/GaAs quantum dot in the few-exciton limit. *Sol. State Comm.*, **114**, 227 (2000)

[30] E. Dekel, D. Gershoni, E. Ehrenfreund, J. M. Garcia, P. M. Petroff. Carrier-carrier correlations in an optically excited single semiconductor quantum dot. *Phys. Rev. B*, **61**, 16, 11009 (2000)

[31] K. Ota, N. Usami, Y. Shiraki. Temperature dependence of microscopic photoluminescence spectra of quantum dots and quantum wells. *Physica E*, **2**, 573, (1998)

[32] R. Rinaldi, P. V. Giugno, R. Cingolani, H. Lipsanen, M. Sopanen, J. Tulkki, J. Ahopelto. Zeeman effect in parabolic quantum dots. *Phys. Rev. Lett.*, **77**, 2, 342 (1996)

[33] M. Bayer, G. Ortner, O. Stern, A.Kuther, A. A. Gorbunov, A. Forchel, P. Hawrylak, S. Fafard, K. Hinzer, T. L. Reinecke, S. N. Walck, J. P. Reithmaier, F. Klopf, F. Schäfer. Fine structure of neutral and charged

excitons in self-assembled In(Ga)As/(Al)GaAs quantum dots. *Phys. Rev. B*, **65**, 195315 (2002)

[34] F. Findeis, M. Baier, E. Beham, A. Zrenner, G. Abstreiter. Photocurrent and photoluminescence of a single self-assembled quantum dot in electric fields. *Appl. Phys. Lett.*, **78**, 19, 2958 (2001)

[35] A. Hartmann, Y. Ducommun, E. Kapon, U. Hohenester, E. Molinari. Few-particle effects in semiconductor quantum dots: observation of multicharged excitons. *Phys. Rev. Lett.*, **84**, 24, 5648 (2000)

[36] A. Forchel, R. Steffen, T. Koch, M. Michel, M. Albrecht, T. L. Reinecke. Optical studies of free-standing single InGaAs/GaAs quantum dots. *Semicond. Sci. Technol.*, **11**, 1529 (1996)

[37] R. Steffen, A. Forchel, T. L. Reinecke, T. Koch, M. Albrecht, J. Oshinowo, F. Faller. Single quantum dots as local probes of electronic properties of semiconductors. *Phys. Rev. B*, **54**, 3, 1510 (1996)

[38] M. Bayer, S. N. Walck, T. L. Reinecke, A. Forchel. Exciton binding energies and diamagnetic shift in semiconductor quantum wires and quantum dots. *Phys. Rev. B*, **57**, 11, 6584 (1998)

[39] M. Bayer, T. Gutbrod, A. Forchel, V. D. Kulakovskii, A. Gorbunov, M. Michel, R. Steffen, K. H. Wang. Exciton complexes in $In_xGa_{1-x}As$/GaAs quantum dots. *Phys. Rev. B*, **58**, 8, 4740 (1998)

[40] J. Stangl, V. Holy, G. Bauer. Structural properties of self-organized semiconductor nanostructures. *Rev. of Modern Phys.*, **76**, 725 (2004)

[41] O. Flebbe, H. Eisele, T. Kalka, F. Heinrichsdirff, A. Krost, D.Bimberg, M. Dähne-Prietsch. Atomic structure of stacked InAs quantum dots grown by metal-organic chemical vapor deposition. *J. Vac. Sci. Technol. B.* **17**, 4, 1639 (1999)

[42] S. Kret, T. Benabbas, C. Delamarre, Y. Androussi, A. Dubon, J. Y. Laval, A. Lefebvre. High resolution electron microscope analysis of lattice distortions and In segregation in highly strained $In_{0,35}Ga_{0,65}As$ coherent islands grown on GaAs (001). *J. Appl. Phys.*, **86**, 4, 1988 (1999)

[43] E. Dekel, D. V. Regelman, D. Gershoni, E. Ehrenfreund, W. V. Schoenfeld, P. M. Petroff. Cascade evolution and radiative recombination of quantum dot multiexcitons studied by time-resolved spectroscopy. *Phys. Rev. B*, **62**, 16, 11038 (2000)

[44] S. Rodt, A. Schliwa, R. Heitz, V. Türck, O. Stier, R. L. Sellin, M. Strassburg, U. W. Pohl, D. Bimberg. Few-particle effects in self-organized quantum dots. *Phys. Status Solidi B*, **234**, 1, 354 (2002)

[45] S. Rodt, A. Schliwa, K. Pötschke, F. Guffarth, D. Bimberg. Correlation of structural and few-particle properties of self-organized InAs/GaAs quantum dots. *Phys. Rev. B*, **71**, 155325 (2005)

[46] K. Leosson, J. R. Jensen, J. M. Hvam, W. Langbein. Linewidth statistics of single InGaAs quantum dot photoluminescence lines. *Phys. Status Solidi B*, **221**, 49 (2000)

[47] F. Guffarth, R. Heitz, A. Schliwa, K. Pötschke, D. Bimberg. Observation of monolayer-splitting for InAs/GaAs quantum dots. *Physica E*, **21**, 326 (2004)

[48] R. Heitz, F. Guffarth, K. Pötschke, A. Schliwa, D. bimberg, N. D. Zakharov, P. Werner. Shell like formation of self-organized InAs/GaAs quantum dots. *Phys. Rev. B*, **71**, 453325 (2005)

[49] R. M. Thompson, R. M. Stevenson, A. J. Shields, I. Farrer, C. J. Lobo, D. A. Ritchie, M. L. Leadbeater, M. Pepper. Single-photon emission from exciton complexes in individual quantum dots. *Phys. Rev. B*, **64**, 201302R (2001)

[50] G. Chen, T. H. Stievater, E. T. Batteh, X. Li, D, G, Steel, D. Gammon, D. S. katzer, D.Park, L. J. Sham. Biexciton quantum coherence in a single quantum dot. *Phys. Rev. Lett.*, **88**, 11, 117901 (2002)

[51] X. Li, Y. Wu, D. Steel, D. Gammon, T. H. Stievater, D. S. Katzer, D. Park, C. Piermarocchi, L. J. Sham. An all-optical quantum gate in a semiconductor quantum dot. *Science*, **301**, 809 (2003)

[52] M. A. Lampert. Mobile and immobile effective-mass-particle complexes in nonmetallic solids. *Phys. Rev. Lett.*, **1**, 12, 450 (1958)

[53] R. C. Miller, D. A. Kleinman, A. C. Gossard, O. Munteanu. Biexcitons in GaAs quantum wells. *Phys. Rev. B*, **25**, 10, 6545 (1982)

[54] S. Nair, T. Takagahara. Theory of exciton pair states and their nonlinear optical properties in semiconductor quantum dots. *Phys. Rev. B*, **55**, 8, 5153 (1998)

[55] P. Lelong, O. Heller, G. Bastard. Coulomb interactions in small InAs quantum dots. *Solid State Elec.*, **42**, 7-8, 1251 (1998)

[56] O. Stier, A. Schliwa, R. Heitz, M. Grundmann, D. Bimberg. Stability of biexcitons in pyramidal InAs/GaAs quantum dots. *Phys. Status Solidi B*, **224**, 1, 115 (2001)

[57] O. Stier, R. Heitz, A. Schliwa, D. Bimberg. Shape and composition effects on excitons and biexcitons in quantum dots. *Phys. Status Solidi A*, **190**, 2, 477 (2002)

[58] S. Rodt, R. Heitz, A. Schliwa, R. L. Sellin, F. Guffarth, D. Bimberg. Repulsive exciton-exciton interaction in quantum dots. *Phys. Rev. B*, **68**, 35331 (2003)

[59] M. Kastner. Artificial atoms. *Phys. Tod*. **46**, 24 (1993)

[60] T. W. Hänsch, H. Walther. Laser spectroscopy and quantum optics. *Rev. Mod. Phys.*, **71**, 2, 242 (1999)

[61] O. Stier, M. Grundmann, D. Bimberg. Electronic and optical properties of strained quantum dots modelled by 8-band k·p theory. *Phys. Rev. B*, **59**, 8, 5688 (1999)

[62] G. W. Bryant, W. Jaskolski. Designing quantum dots and quantum-dot solids. *Physica E*, **11**, 72 (2001)

[63] A. Williamson, A. Zunger, A. Canning. Prediction of a strain-induced conduction-band minimum in embedded quantum dots. *Phys. Rev. B*, **57**, 8, R4253 (1998)

[64] M. Grundmann, O. Stier, D. Bimberg. InAs/GaAs pyramidal quantum dots: strain distribution, optical phonons, and electronic structure. *Phys. Rev. B*, **52**, 16, 11969 (1995)

[65] C. Pryor. Eight-band calculations of strained InAs/GaAs quantum dots compared with one-, four-, and six-bands approximations. *Phys. Rev. B*, **57**, 12, 7190 (1998)

[66] D. V. Regelman, E. Dekel, D. Gershoni, E. Ehrenfreund, A. J. Williamson, J. Shumway, A. Zunger, W. V. Schoenfeld, P. M. Petroff. Optical spectroscopy of single quantum dots at tunable positive, neutral, and negative charge states. *Phys. Rev. B*, **64** 165301 (2001)

[67] K. Hinzer, P. Hawrylak, M. Korkusinski, S. Fafard, M. Bayer, O. Stern, A. Gorbunov, A. Forchel. Optical spectroscopy of a single $Al_{0,36}In_{0,64}As/Al_{0,33}Ga_{0,67}As$ quantum dot. *Phys. Rev. B*, **63**, 75314 (2001)

[68] P. Hawrylak. Excitonic artificial atoms: engineering optical properties of quantum dots. *Phys. Rev. B*, **60**, 8, 5597 (1999)

[69] W. Langbein, J. M. Hvam. Localization-enhanced biexciton binding energy in semiconductors. *Phys. Rev. B*, **59**, 23, 15405 (1999)

[70] S. Adachi, T. Miyashita, S. Takeyama, Y. Takagi, A. Tackeuchi, M. Nakayama. Polarization choices in exciton-biexciton system of GaAs quantum wells. *Phys. Rev. B*, **55**, 3, 1654 (1997)

[71] T. Baars, W. Braun, M. Bayer, A. Forchel. Biexcitons in semiconductor quantum wires. *Phys. Rev. B*, **58**, 4, R1750 (1998)

[72] A. Euteneuer, J. Möbius, R. Rettig, E. J. Mayer, M. Hofmann, W. Stolz, E. O. Göbel, W. W. Rühle. Biexciton binding energies in the transition regime from three- to two-dimensional semiconductors. *Phys. Rev. B*, **56**, 16, R10028 (1997)

[73] J. Zhang, T. Pang, C. Chen. Biexcitons in quantum wells: a quantum Monte Carlo study. *Phys. Lett. A*, **206**, 101 (1995)

[74] P. Borri, W. Langbein, J. M. Hvam, F. Martelli. Binding energy and dephasing of biexcitons in $In_{0,18}Ga_{0,82}As/GaAs$ single quantum wells. *Phys. Rev. B*, **60**, 7, 4505 (1999)

[75] Y. Masumoto, S. Okamoto, S. Katayanagi. Biexciton binding energy in CuCl quantum dots. *Phys. Rev. B*, **50**, 24, 18658 (1994)

[76] S. Schmitt-Rink, D. A. B. Miller, D. S. Chemla. Theory of the linear and nonlinear optical properties of semiconductor microcrystallites. *Phys. Rev. B*, **35**, 15, 8113 (1987)

[77] W. Xie. Binding energy of biexcitons in quantum dots. *J. Phys. Condens. Matter*, **13**, 3149 (2001)

[78] T. Takagahara. Effects of dielectric confinement and electron-hole exchange interaction on excitonic states in semiconductor quantum dots. *Phys. Rev. B*, **47**, 8, 4569 (1993)

[79] E. L. Ivchenko, P. Pikus. Superlattices and other heterostructures. *Springer*, Berlin (1997)

[80] G. Bester, S. Nair, A. Zunger. Pseudopotential calculation of the excitonic fine structure of million-atom self-assembled $In_{1-x}Ga_xAs/GaAs$ quantum dots. *Phys. Rev. B*, **67**, 161306R (2003)

[81] M. Sugawara. Theory of spontaneous-emission lifetime of Wannier excitons in mesoscopic semiconductor quantum disks. *Phys. Rev. B*, **51**, 16, 10743 (1995)

[82] J. Bellessa, V. Voliotis, R. Grousson, X. L. Wang, M. Ogura, H. Matsuhata. Quantum-size effects on radiative lifetimes and relaxation of excitons in semiconductor nanosctructures. *Phys. Rev. B*, **58**, 15, 9933 (1998)

[83] H. Benisty, C. M. Sotomayor-Torres, C. Weisbuch. Intrinsic mechanism for the poor luminescence properties of quantum-box systems. *Phys. Rev. B*, **44**, 19, 10945 (1991)

[84] U. Bockelmann. Exciton relaxation and radiative recombination in semiconductor quantum dots. *Phys. Rev. B*, **48**, 23, 17637 (1993)

[85] B. Ohnesorge, M. Albrecht, J. Oshinowo, A. Forchel, Y. Arakawa. Rapid carrier relaxation in self assembled $In_xGa_{1-x}As/GaAs$ quantum dots. *Phys. Rev. B*, **54**, 16, 11532 (1996)

[86] R. Heitz, M. Grundmann, N. N. Ledentsov, L. Eckey, M. Veit, D. Bimberg, V. M. Ustinov, A. Y. Egorov, A. E. Zhukov, P. S. Kop'ev, Z. I. Alferov. Multiphonon-relaxation processes in self-organized InAs/GaAs quantum dots. *Appl. Phys. Lett.*, **68**, 3, 361 (1996)

[87] T. S. Sosnowsky, T. B. Norris, H. Jiang, J. Singh, K. Kamath, P. Bhattacharya. Rapid carrier relaxation in $In_{0,4}Ga_{0,6}As/GaAs$ quanum dots characterised by differential transmission spectroscopy. *Phys. Rev. B*, **57**, 16, R9423 (1998)

[88] Y. Toda, O. Moriwaki, M. Nishioka, Y. Arakawa. Efficient carrier relaxation mechanism in InGaAs/GaAs self-assembled quantum dots based on the existence of continuum states. *Phys. Rev. Lett.*, **82**, 20, 4114 (1999)

[89] R. Heitz, I. Mukhametzhanov, O. Stier, A. Madhukar, D. Bimberg. Enhanced polar exciton-LO-phonon interaction in quantum dots. *Phys. Rev. Lett.*, **83**, 22, 4654 (1999)

[90] X-Q. Li, Y. Arakawa. Optical linewidths in an individual quantum dot. *Phys. Rev. B*, **60**, 3, 1915 (1999)

[91] X. Fan, T. Takagahara, J. E. Cunningham, H. Wang. Pure dephasing induced by exciton-phonon interactions in narrow GaAs quantum wells. *Solid State Commun.*, **108**, 11, 857 (1998)

[92] L. Besombers, K. Kheng, L. Marsal, H. Mariette. Acoustic phonon broadening mechanism in single quantum dot emission. *Phys. Rev. B*, **63**, 155307 (2001)

[93] I. Favero, G. Cassabois, R. Ferreira, D. Darson, C. Voisin, J. Tignon, C. Delalande, G. Bastard, Ph. Roussignol, J. M. Gerard. Acoustic phonon sidebands in the emission line of single InAs/GaAs quantum dots. *Phys. Rev. B*, **68**, 233301 (2003)

[94] D. Gammon, E. S. Snow, B. V. Shanabrook, D. S. Katzer, D. Park. Homogeneous linewidths in the optical spectrum of a single gallium arsenide quantum dot. *Science*, **273**, 87 (1996)

[95] R. Heitz, H. Born, F. Guffarth, O. Stier, A. Schliwa, A. Hoffmann, D. Bimberg. Existence of a phonon bottleneck for excitons in quantum dots. *Phys. Rev. B*, **64**, 241305R (2001)
[96] H. Kamada, J. Temmyo, M. Notomi, T. Furuta, T. Tamamura. Dephasing processes in self-organised strained InGaAs single-dots on (311)B-GaAs substrate. *Jpn. J. Appl. Phys.*, **36**, 4194 (1997)
[97] P. Borri, W. Langbein, S. Schneider, U. Woggon, R. L. Sellin, D. Ouyang, D. Bimberg. Relaxation and dephasing of multiexcitons in semiconductor quantum dots. *Phys. Rev. Lett.*, **89**, 18, 187401 (2002)
[98] D. A. B. Miller, D. S. Chemla, T. C. Damen, A. C. Gossard, W. Wiegmann, T. H. Wood, C. A. Burrus. Band-edge electroabsorption in quantum well structures: the quantum-confined stark effect. *Phys. Rev. B*, **32**, 1043 (1985)
[99] S. A. Empedocles, M. G. Bawendi. Quantum-confined stark effect in single CdSe nanocrystallite quantum dots. *Science*, **278**, 2114 (1997)
[100] V. Türck, S. Rodt, O. Stier, R. Heitz, R. Engelhardt, U. W. Pohl, D. Bimberg, R. Steingrüber. Effect of random field fluctuations on excitonic transitions of individual CdSe quantum dots. *Phys. Rev. B*, **61**, 15, 9944 (2000)
[101] J. Seufert, R. Weigand, G. Bacher, T. Kümmel, A. Forchel, K. Leonardi, D. Hommel. Spectral diffusion of the exciton transition in a single self-organized quantum dot. *Appl. Phys. Lett.*, **76**, 14 (2000)
[102] M-E. Pistol, P. Castrillo, D. Hessman, J. A. Prieto, L. Samuelson. Random telegraph noise in photoluminescence from individual self-assembled quantum dots. *Phys. Rev. B*, **59**, 16 (1999)
[103] D. Bertram, M. C. Hanna, A. J. Nozik. Two color blinking of single strain-induced GaAs quantum dots. *Appl. Phys. Lett.*, **74**, 18, 2666 (1999)
[104] L. Besombers, K. Kheng, L. Marsal, H. Mariette. Few-particle effects in single CdTe quantum dots. *Phys. Rev. B*, **65**, 121314R (2002)
[105] M. Cardona. Renormalization of the optical response of semiconductors by electron-phonon interaction. *Phys. Status Solidi A*, **188**, 4, 1209 (2001)
[106] S. Biernacki, U. Scherz, B. K. Meyer. Temperature dependence of optical transitions between electronic energy levels in semiconductors. *Phys. Rev. B*, **49**, 7, 4501 (1994)
[107] K. P. O'Donnel, X. Chen. Temperature dependence of semiconductor band gaps. *Appl. Phys. Lett.*, **58**, 25, 2924 (1991)
[108] R. Pässler. Basic model relations for temperature dependencies of fundamental energy gaps in semiconductor. *Phys. Status Solidi B*, **200**, 155 (1997)
[109] R. Pässler. Temperature dependence of exciton peak energies in multiple quantum wells. *J. Appl. Phys.*, **83**, 6, 3356 (1998)
[110] R. Pässler. Parameters sets due to fittings of the temperature dependencies of fundamental bandgaps in semiconductors. *Phys. Status Solidi B*, **216**, 975 (1999)
[111] R. Pässler. Moderate phonon dispersion shown by the temperature dependence of fundamental band gaps of various elemental and binary

semiconductors including wide-band gap materials. *J. Appl. Phys.*, **88**, 5, 2570 (2000)

[112] M. V. Maximov, A. F. Tsatsul'nikov, B. V. Volovik, D. S. Sizov, Y. M. Shernyakov, I. N. Kaiander, A. E. Zhukov, A. R. Kovsh, S. S. Mikhrin, V. M. Ustinov, Z. I. Alferov, R. Heitz, V. A. Shchukin, N. N. Ledenntsov, D. Bimberg, Y. G. Musikhin, W. Neumann. Tuning quantum dot properties by activated phase separation of an InGa(Al)As alloy grown on InAs stressors. *Phys. Rev. B*, **62**, 24, 16671 (2000)

[113] S. Yoon, Y. Moon, T.-W. Lee, H. Hwang, E. Yoon, Y. D. Kim. Shape change of InAs self-assembled quantum dots induced by As/P exchange reaction. *Thin Solid Films*, **357**, 81 (1999)

[114] D. V. Kazantsev, C. Dal Savio, K. Pierz, B. Güttler, H.-U. Danzebrink. Low-temperature scanning system for near and far-field optical investigations. *J. of Microscopy*, **209**, 199 (2003)

[115] H-U. Danzebrink, D. V. Kazantsev, C. Dal Savio, K. Pierz, B. Güttler. Optical microscope with SNOM option for micro- and nanoanalytical investigations at low temperatures. *Appl. Phys. A*, **76**, 889 (2003)

[116] C. Dal Savio, H. Wolff, T. Dziomba, H.-A. Fuß, H.-U. Danzebrink. A compact sensor head for simultaneous scanning force and near-field optical microscopy. *Prec. Engineering*, **26**, 199 (2002)

[117] G. Behme, A. Richter, M. Süptitz, C. Lienau. Vacuum near-field scanning optical microscope for variable cryogenic temperatures. *Rev. Sci. Inst.*, **68** (9), 3458 (1997)

[118] D. I. Lubyshev, P. P. Gonzalez-Borrero, E. Marega, E. Petitprez, N. La Scala, P. Basmaji. Exciton localization and temperature stability in self-organized InAs quantum dots. *Appl. Phys. Lett.*, **68**, 2, 205 (1996)

[119] Z. Y. Xu, Z. D. Lu, X. P. Yang, Z. L. Yuan, B. Z. Zheng, J. Z. Xu, W. K. Ge, Y. wang, J. wang, L. L. Chang. Carrier relaxation and thermal activation of localized excitons in self-organized InAs multilayers grown on GaAs substrates. *Phys. Rev. B*, **54**, 16 (1996)

[120] P. Dawson, O. Rubel, S. D. Baranovskii, K. Pierz, P. Thomas, E. O. Göbel. Temperature dependent optical properties of InAs/GaAs quantum dots: exciton versus independent carrier exchange. *To be published*

[121] H. W. Yoon, D. R. Wake, J. P. Wolfe. Effect of exciton-carrier thermodynamics on the GaAs quantum well photoluminescence. *Phys. Rev. B*, **54**, 4, 2763 (1996)

[122] E. S. Moskalenko, K. F. Karlsson, P. O. Holtz, B. Monemar, W. V. Schoenfeld, J. M. Garcia, P. M. Petroff. Influence of excitation energy on charged exciton formation in self-assembled InAs quantum dots. *Phys. Rev. B*, **64**, 085302 (2001)

[123] K. Brunner, G. Abstreiter, G. Böhm, G. Tränkle, G. Weimann. Sharp-line photoluminescence and two-photon absorption of zero-dimensional biexcitons in a GaAs/AlGaAs structure. *Phys. Rev. Lett.*, **73**, 8, 1138 (1994)

[124] H. Kamada, H. Ando, J. Temmyo, T. Tamamura. Excited-state optical transitions of excitons and biexcitons in a single $In_xGa_{1-x}As$ quantum disc. *Phys. Rev. B*, **58**, 24, 16243 (1998)

[125] G. Bacher, R. Weigand, J. Seufert, V. D. Kulakowskii, N. A. Gippius, A. Forchel, K. Leonardi, D. Hommel. Biexciton versus exciton lifetime in a single semiconductor quantum dot. *Phys. Rev. Lett.*, **83**, 21, 4417 (1994)

[126] A. Kiraz, S. Fälth, C. Becher, B. Gayral, W. V. Schoenfeld, P. M. Petroff, L. Zhang, E. Hu, A. Imamoglu. Photon correlation spectroscopy of a single quantum dot. *Phys. Rev. B*, **65**, 161303R (2002)

[127] E. Moreau, I. Robert, L. Manin, V. Thierry-Mieg, J. M. Gerard, I. Abram. Quantum cascade of photons in semiconductor quantum dots. *Phys. Rev. Lett.*, **87**, 18, 183601 (2001)

[128] M. Bayer, O. Stern, P. Hawrylak, S. Fafard, A. Forchel. Hidden symmetries in the energy levels of excitonic 'artificial atoms'. *Nature*, **405**, 923 (2000)

[129] L. Landin, M. S. Miller, M.-E. Pistol, C. E. Pryor, L. Samuelson. Optical studies of individual InAs quantum dots in GaAs: few-particle effects. *Science*, **280**, 262 (1998)

[130] C. Kammerer, C. Voisin, G. Cassabois, C. Delalande, P. Roussignol, F. Klopf, J. P. Reithmaier, A. Forchel, J. M. Gerard. Line narrowing in single semiconductor quantum dots: toward the control of environment effects. *Phys. Rev. B*, **66**, 41306R (2002)

[131] C. Kammerer, G. Cassabois, C. Voisin, C. Delalande, P. Roussignol, A. Lemaitre J. M. Gerard. Efficient acoustic phonon broadening in single self-assembled InAs/GaAs quantum dots. *Phys. Rev. B*, **65**, 33313 (2001)

[132] C. Kammerer, G. Cassabois, C. Voisin, M. Perrin, C. Delalande, P. Roussignol, J. M. Gerard. Interferometric correlation spectroscopy in single quantum dots. *Appl. Phys. Lett.*, **81**, 15, 2737 (2002)

[133] B. Urbaszek, E. J. McGhee, M. Krüger, R. J. Warburton, K. Karrai, T. Amand, B. D. Gerardot, P. M. Petroff, J. M. Garcia. Temperature-dependent linewidth of charged excitons in semiconductor quantum dots: strongly broadened ground state transitions due to acoustic phonon scattering. *Phys. Rev. B*, **69**, 35304 (2004)

[134] P. Borri, W. Langbein, S. Schneider, U. Woggon, R. L. Sellin, D. Ouyang, D. Bimberg. Ultralong dephasing time in InGaAs quantum dots. *Phys. Rev. Lett.*, **87**, 15, 157401 (2001)

[135] H. Gotoh, H. Kamada, T. Saitoh, H. Ando, J. Temmyo. Effects of biexcitons on exciton decoherence processes in $In_xGa_{1-x}As$ quantum dots. *Phys. Rev. B*, **69**, 155328 (2004)

[136] S. Kaiser, T. Mensing, L. Worschech, F. Klopf, J. P. Reithmaier, A. Forchel. Optical spectroscopy of single InAs/InGaAs quantum dots in a quantum well. *Appl. Phys. Lett.*, **81**, 26 (2002)

[137] M. Bayer, A. Kuther, A. Forchel, A. Gorbunov, V. B. Timofeev, F. Schäfer, J. P. Reithmaier, T. L. Reinecke, S. N. Walck. Electron and hole g factors and exchange interaction from studies of the exciton fine structure in $In_{0,60}Ga_{0,40}As$ quantum dots. *Phys. Rev. Lett.*, **82**, 8, 1748 (1999)

[138] M. Bayer, A. Kuther, F. Schäfer, J. P. Reithmaier, A. Forchel. Strong variation of the exciton g factors in self-assembled $In_{0,60}Ga_{0,40}As$ quantum dots. *Phys. Rev. B*, **60**, 12, R8481 (1999)

[139] J. J. Finley, D. J. Mowbray, M. S. Skolnick, A. D. Ashmore, C. baker, A. F. G. Monte, M. Hopkinson. Fine structure of charged and neutral excitons in InAs-$Al_{0,6}Ga_{0,4}As$ quantum dots. *Phys. Rev. B*, **66**, 153316 (2002)

[140] J. J. Finley, P. W. Fry, A. D. Ashmore, A. Lemaitre, A. I. Tartakovskii, R. Oulton, D. J. Mowbray, M. S. Skolnick, M. Hopkinson, P. D. Buckle, P. A. Maksym. Observation of multicharged excitons and biexcitons in a single InGaAs quantum dot. *Phys. Rev. B*, **64**, 161305R (2001)

[141] M. Baier, F. Findeis, A. Zrenner, M. Bichler, G. Abstreiter. Optical spectroscopy of charged excitons in single quantum dot photodiodes. *Phys. Rev. B*, **64**, 195326 (2001)

[142] A. Kuther, M. Bayer, A. Forchel, A. Gorbunov, V. B. Timofeev, F. Schäfer, J. P. Reithmaier. Zeeman splitting of excitons and biexcitons in single $In_{0,6}Ga_{0,4}As$/GaAs self-assembled quantum dots. *Phys. Rev. B*, **58**, 12, R7508 (1998)

[143] F. Findeis, A. Zrenner, G. Böhm, G. Abstreiter. Phonon-assisted biexciton generation in a single quantum dot. *Phys. Rev. B*, **61**, 16, R10579 (2000)

[144] L. Landin, M.-E. Pistol, C. Pryor, M. Persson, L. Samuelson, M. Miller. Optical investigations of individual InAs quantum dots: level splittings of exciton complexes. *Phys. Rev. B*, **60**, 24,16640 (1999)

[145] A. Zrenner, M. Markmann, A. Paassen, A. L. Elfros, M. Bichler, W. Wegscheider, G. Böhm, G. Abstreiter. Spatially resolved magneto-optics on confined systems. *Physica B*, **256**, 300 (1998)

[146] J. J. Finley, A. D. Ashmore, A. Lemaitre, D. J. Mowbray, M. S. Skolnick, I. E. Itskevich, P. A. Maksym, M. Hopkinson, T. F. Krauss. Charged and neutral exciton complexes in individual self-assembled In(Ga)As quantum dots. *Phys. Rev. B*, **63**, 73307 (2001)

[147] T. Saiki, K. Nishi, M. Ohtsu. Low temperature near-field photoluminescence spectroscopy of InGaAs single quantum dots. *Jpn. J. Appl. Phys.*, **37**, 1, 1638 (1998)

[148] M. Persson, N. Panev, L. Landin, S. Jeppesen, M.-E. Pistol. Relaxation pathways in InAs/GaAs quantum dots. *Phys. Rev. B*, **64**, 075309 (2001)

[149] K. Matsuda, K. Ikeda, T. Saiki, H. Tsuchiya, H. Saito, K. Nishi. Homogeneous linewidth broadening in $In_{0,5}Ga_{0,5}As$/GaAs single quantum dot at room temperature investigated using a highly sensitive near-field scanning optical microscope. *Phys. Rev. B*, **63**, 121304R (2001)

[150] G. Chen, T. H. Stievater, E. T. Batteh, X. Li, D. G. Steel, D. Gammon, D. S. Katzer, D. Park, L. J. Sham. Biexciton quantum coherence in a single quantum dot. *Phys. Rev. Lett.*, **88**, 11, 117901 (2002)

[151] D. Sarkar, H. P. van der Meulen, J. M. Calleja, J. M. Becker, R. J. Haug, K. Pierz. Phonons in InAs/AlAs single quantum dots observed by optical emission. *Phys. Rev. B*, **71**, 81302R (2005)

[152] H. Kamada, H. Ando, J. Temmyo, T. Tamamura. Excited-state optical transitions of excitons and biexcitons in a single $In_xGa_{1-x}As$ quantum disk. *Phys. Rev. B*, **58**, 24, 16234 (1998)

[153] E. Peter, J. Hours, P. Senellart, A. Vasanelli, A. Cavanna, J. Bloch, J. M. Gerard. Phonon sidebands in exciton and biexciton emission from single GaAs quantum dots. *Phys. Rev. B*, **69**, 41307R (2004)

[154] M. Achermann, J. A. Hollingsworth, V. I. Klimov. Multiexcitons confined within a subexcitonic volume: spectroscopic and dynamical signatures of neutral and charged biexcitons in ultrasmall semiconductor nanocrystals. *Phys. Rev. B*, **68**, 245302 (2003)